Fakultät für Elektrotechnik und Informationstechnik

Physically Consistent Modeling of Multi-Antenna Systems

Tobias Christian Laas

Vollständiger Abdruck der von der Fakultät für Elektrotechnik und Informationstechnik der Technischen Universität München zur Erlangung des akademischen Grades eines

Doktors der Ingenieurwissenschaften

genehmigten Dissertation.

Vorsitz: Prof. Dr.-Ing. Erwin Biebl

Prüfer*innen der Dissertation:

1. Prof. Dr. techn. Dr. h. c. Josef A. Nossek
2. Prof. Dr.-Ing. Amine Mezghani
3. Prof. Dr.-Ing. Thomas Eibert

Die Dissertation wurde am 16.11.2021 bei der Technischen Universität München eingereicht und durch die Fakultät für Elektrotechnik und Informationstechnik am 30.03.2022 angenommen.

Acknowledgments

This thesis is mainly based on my research work at the Munich Research Center, Huawei Technologies Duesseldorf GmbH, and at the Associate Professorship Methods of Signal Processing at the Department of Electrical and Computer Engineering, Technical University of Munich.

First of all, I would like to express my deepest gratitude to my supervisor Prof. Josef A. Nossek for his continuous support, motivation and guidance. In addition I am extremely grateful to Prof. Wolfgang Utschick for the opportunity to join his research group like an internal member and to supervise the Digital Signal Processing Laboratory at TUM. I would like to express my sincere gratitude to my mentors Dr. Mario H. Castañeda Garcia and Dr. Samer Bazzi for their guidance and our fruitful discussions, as well as my mentor and superior Dr. Wen Xu for supporting my research topic. I would also like to thank Prof. Amine Mezghani for serving as a second examiner and Prof. Erwin Biebl for chairing my examination committee. A special thanks goes to Prof. Thomas Eibert for serving as a third examiner and for conducting the simulation of an antenna array in CST Studio Suite.

I would like to thank all my colleagues and friends at Huawei and at TUM for the good working atmosphere, and the amazing lunch and coffee breaks. Many thanks to Anastasios Kakkavas for our successful collaboration, and for reviewing many of my research papers, as well as to my fellow doctoral candidates at Huawei, Anastasios Foliadis, Dr. Fabio Pittalá, Ferhad Askerbeyli, José Mauricio Perdomo, Dr. Maja Ćurić, Dr. Marcin Iwanow, Dr. Marcin Pikus, Michail Palaiologos, M. Yusuf Şener, Naveed Iqbal, Prajwal Keshavamurthy, Ramya Panthangi Manjunath, Tapisha Soni, Taylan Şahin, Dr. Yilin Li and Yunyan Chang. Specifically I would also like to thank my Huawei colleagues, Dr. Jian Luo, Dr. Malte Schellmann, Dr. Martin Schubert, Dr. Mate Boban, Dr. Najeeb Ul Hassan, Dr. Onurcan İşcan, Dr. Nikola Vučić, Dr. Panagiotis Spapis and Dr. Ronald Böhnke for the insights and discussions. In addition, I would like to thank my colleague Ignacio González Sebastián from the Advanced Antenna Systems department at Huawei for the discussions and for conducting a simulation of an antenna array in HFSS.

I have also learnt a lot from working with the DSP Lab tutors Georg Maringer, Nicholas Bing Yang Gay, Amir H. Rezaei Tabar and Tiantian Qiu, and from the interaction with the students and would like to thank them. In particular, I would also like to mention Thiago Azevedo de Vasconcelos, whose Master's thesis I assisted in supervising. I am also very grateful to Dr. Michael Joham for his support, in particular related to teaching, and to Dr. Christoph Stöckle, Dr. Jawad Munir, Michael Newinger and Oliver de Candido, who were very supportive with the DSP Lab. Thanks to all the fellow internal and external doctoral candidates and postdocs at TUM, Dr. Chistoph Hellings, Dr. Johannes Russer, Dr. Andreas Barthelme, Dr. Andreas Lenz, Andreas Noll, Benedikt Fesl, Dr. Bernhard Lehmeyer, Daniel Plabst, Diego Lentner, Dominik Semmler, Donia Ben Amor, Florian Bischeltsrieder, Dr. F. Javier García Gómez, Franz Weißer, Dr. Friederike Fohlmeister, Dr. Hela

Jedda, Dr. Israa H. Slim, Dr. Johannes Obermaier, Julia Sistermanns, Dr. Kilian Roth, Dr. Leonardo Gomes Baltar, Lorenz Weiland, Dr. Markus Hefele, Dr. Matthias Hotz, Michael Baur, Michael Hani, Michael Koller, Michael Würth, Nurettin Turan, S. Hamidreza Moghadas, Thomas Wiegart, Dr. Thomas Wiese and Valentina Rizzello.

In addition, I would like to thank Christopher Mollén, PhD for asking inspiring questions that motivated the investigation presented in Chapter 3. I would also like to acknowledge the cooperation with our external partner Dr. Armin Dammann from the German Aerospace Center (DLR) on positioning, a topic not directly related to the dissertation. I would further like to acknowledge that the research work leading to two papers that are previous publications of my dissertation was supported in part by the Horizon 2020 project ONE5G (ICT-760809) receiving funds from the European Union.

Thanks for the administrative and technical support at TUM from Ali Yilmazcan, Ulrike Heer and Sergey Fedorov, and at Huawei from our team assistants and the Admin, IT and HR colleagues.

Tobias Laas, July 2022.

Abstract

Physically consistent modeling for wireless communication systems takes mutual coupling between the antenna elements into account at the transmitter and receiver, in contrast to conventionally modeled systems. In this work, the reciprocity of the channel is analyzed with mutual coupling taken into account, and a fair comparison with the performance when mutual coupling is neglected is presented. Furthermore, the mutual reactance of hypothetical isotropic radiators is derived and its impact on the performance is analyzed. The analysis is extended to antenna arrays with a small mutual reactance. Then the transmit and receive antenna array gain of uniform linear, circular and rectangular arrays is studied for various antenna separations and numbers of antennas. Thereby guidelines on how to shape antenna arrays optimally are derived.

Contents

1. Introduction

Antenna arrays at the base station and at the mobiles are an integral feature of the current cellular wireless standard, which is the so-called fifth generation (5G). 5G new radio (NR) was first released in 2018 (Release 15) [1]. The second release, Release 16, was published in 2020 and further development of 5G is ongoing [2]. In addition, research for the future sixth generation (6G) cellular wireless standard has already started, see e.g. [3]. A first release of 6G is expected towards the end of the 2020s or beginning of the 2030s.

One of the key features of 5G NR is the support for a larger number of antennas at the base stations and mobiles, and a better support for exploiting these antennas. Multiple antennas allow for beamforming at the transmitter and at the receiver of as many different signals as there are antennas. Beamforming of narrowband signals works by adjusting their phase and amplitude such that there is constructive and destructive interference in the desired directions of the electromagnetic field radiated and received by the individual antennas. This concept is also called multiple-input multiple-output (MIMO). A larger number of antennas can increase the achievable gain, i.e., it allows for a larger signal-to-noise ratio (SNR) at the same transmit power, a lower bit error ratio by exploiting diversity, or to serve more mobiles or streams to each mobile at the same time using spatial multiplexing.

Massive MIMO, i.e., a large number of antennas, is an important building block of future wireless systems. Indeed, the seminal paper [4] that introduced massive MIMO is based on the assumption that there is an unlimited number of base station antennas. In industry and academia, there are different notions of how many antennas a multi-antenna base station needs to have to be considered Massive MIMO: In the 3rd Generation Partnership Project (3GPP), the standardization body behind GSM (Global System for Mobile Communications), UMTS (Universal Mobile Telecommunications System), LTE (Long Term Evolution) and 5G, a Massive MIMO base station is considered to have more than 8 adjustable antennas [5, Ch. 1], whereas in academia, typically hundreds of antennas are assumed.

With the ongoing evolution of 5G and the introduction of 6G, a further increase in the number of antennas is expected. Increasing the number of antennas at the base station and at the mobiles is challenging, because the available area is limited. It is especially challenging at lower frequencies (below $1\,\mathrm{GHz}$), because the dimensions of the area normalized by the wavelength are important. Typical antenna separations are $\lambda/2$ to 0.7λ [5, Ch. 6], which correspond to about $15\,\mathrm{cm}$ to $21\,\mathrm{cm}$ at $1\,\mathrm{GHz}$ for example, but smaller antenna separations are needed to increase the number of antennas even further. As the distance decreases, mutual coupling between the antennas increases. Mutual coupling means that if an antenna in the array is excited by a current, a voltage is induced in the other antennas. Typically, mutual coupling refers to the mutual coupling between the antennas in the same array, which is not considered in conventionally modeled systems. There is also inter-array mutual

coupling, which is what enables wireless communications and is considered to be the channel in conventionally modeled systems.

Mutual coupling influences the radiated power when transmitting and the noise correlations between the antennas when receiving. For a large number of antennas and a small distance between them, it is important to model this correctly using physically consistent modeling. Note that mutual coupling can lead to a superior performance when it is taken into account correctly using physically consistent modeling. Physically consistent modeling based on circuit theory was introduced independently by Wallace and Jensen [6] and by Waldschmidt, Schulteis and Wiesbeck [7] in 2004. This modeling has been developed further in the following years. This development includes the multiport communication theory model [8, 9], which this thesis is based on.

Circuit theory is well suited, because the quantities of the antenna arrays that are important for wireless communications, namely impedance parameters (or equivalently scattering patterns, or any other equivalent description) and radiation patterns, can be computed using an electromagnetic field solver or can be measured. In addition, circuit theory is well suited, because it allows to correctly compute transmit power based on voltages and currents, and because it is attractive for modeling the noise from various noise sources [8]. The communication system can be analyzed based on these parameters. In particular, the physical channel can be represented by an impedance matrix.

In much of the information theory and MIMO wireless communications literature, a higher level of abstraction is used, where transmit and receive signals are normalized and unit-less quantities, whose squared norms are assumed to be proportional to transmit or receive power. Multiport communication theory [8, 9] introduces a systematic mapping to the information-theoretic domain that ensures the proportionality and assigns a unit to the transmit and receive signals. This is explained in more detail in Chapter 2, where the background on physically consistent modeling based on Multiport Communication Theory is reviewed.

An essential aspect in the implementation of communication systems with antenna arrays, where mutual coupling is non-negligible, are decoupling and impedance matching networks (DMNs). DMNs are used to connect power amplifiers and antennas when transmitting and low noise amplifiers and antennas when receiving. They present uncoupled ports to the amplifiers, which are matched to their impedance. However, in massive MIMO systems, they could be almost impossible to implement. In this thesis, we use a simple physically consistent model based on Multiport Communication Theory, where simple means that we omit the theoretically lossless DMNs and directly connect the amplifiers to the antennas. We assume that we have a flat fading channel by assuming that the fading is flat within a narrowband (group of) subcarrier(s) of a multicarrier system, which is the standard assumption in most of the MIMO literature. On each subcarrier in a system with N transmit and M receive antennas, the antennas and the physical channel can be represented by a linear $N + M$ port. The simple physically consistent circuit model is presented in Chapter 2, as well as the properties of infinitely thin but perfectly conducting $\lambda/2$-dipoles. In addition, the mutual impedance between them is derived when they are oriented arbitrarily, which is used to compute the impedance matrices of uniform rectangular arrays with dual-polarized crossed $\lambda/2$-dipoles. In many numerical simulations, we use infinitely thin but perfectly conducting $\lambda/2$-dipoles, because there are analytic expressions for their self-impedance and the mutual impedance between them, as well as for its radiation pattern, and because they are more realistic than hypothetical isotropic radiators.

So far, only a one-way link between a transmitter and a receiver has been studied, but for a practical communication system, the relation between uplink and downlink is important, especially in Time Division Duplex (TDD) systems, which transmit and receive at the same frequency, but not at the same time. In Chapter 3, we study the reciprocity of the information-theoretic uplink

and downlink channel and establish that they are linked to each other by a physically consistent reciprocity relation, even if the transmit and receive chains are reciprocal. Then, we make a fair comparison of capacity and achievable rates when mutual coupling is neglected and when multiport communication theory is used naively. We consider independent and identically distributed (i.i.d.) channels and more realistic channels based on a 3D channel model from QuaDRiGa [10, 11], which implements the 3GPP technical specification (TS) 38.901 channel model [12], which is also used in standardization. Numerical results for various scenarios with a single and with several users having one or more antennas are presented. Uniform circular arrays are used, because they simplify the analysis, as their gain is independent of the azimuth angle for an odd number of antennas. The approach presented however, is not limited to these types of channels, antennas or antennas arrays.

In Chapter 4, we consider the essential question: what is the mutual reactance of hypothetical isotropic radiators? Hypothetical isotropic radiators are a common type of antenna element in the signal processing and wireless communications literature, because an isotropic radiation pattern simplifies the analysis, albeit isotropic radiators do not exist. Their mutual resistance is well known, but their mutual reactance was an open question. We derive their mutual reactance based on passivity. Furthermore, we analyze the impact of ignoring the mutual reactance in uniform linear and circular arrays (ULAs and UCAs) on achievable rates, when the mutual resistance in the arrays is zero. ULAs are a common kind of antenna array in the signal processing and wireless communications literature. In ULAs with hypothetical isotropic radiators, the mutual resistance vanishes for an antenna separation of $\lambda/2$. We further extend this analysis to antenna arrays with more realistic antenna elements, $\lambda/2$-dipoles, which have a small mutual resistance at $\lambda/2$ antenna separation, in addition to their mutual reactance.

In Chapter 5, we consider how the transmit and receive (antenna) array gains behave as the number of antennas is increased to an extremely large number for varying antenna separations and array sizes. Array gain is defined as the ratio of SNRs between a system with many antennas and a system with a single antenna. This chapter extends the analysis of [13], which considers the transmit array gain in a UCA with fixed radius and shows that the minimum energy per bit saturates when the number of antennas in increased. Considering receive array gain is important, because the noise coupling at the receiver caused by mutual coupling leads to different results than for the transmit array gain. Conventional modeling assumes that the array gain grows linearly with the number of antennas regardless of the number of antennas, but this is unreasonable, because the achievable array gain within a certain array size is limited, when then antennas are lossy. To obtain reasonable results, we introduce small losses in the antennas by adding a resistance in series with the antennas, which model the losses that are caused by the finite conductance of the conductors the antennas are made of, among others. Losses in the antennas limit super-gain in the antenna array, even if they are small [14]. Super-gain here means that an array gain is larger than the number of antennas in the array, whereas in conventional modeling, the array gain is bounded by the number of antennas. It can lead to a superior system performance and occurs when a wave with a wavenumber larger than $2\pi/\lambda$ is excited, but this means that the wavenumber becomes complex. A complex wavenumber means that the wave has an evanescent part, and this evanescent part stores energy similar to a reactance [15, Sec. IV-B], [16]. The analysis is extended to uniform rectangular arrays (URAs) with dual-polarized antennas, which is the most common array type at the base station in today's cellular systems. To obtain more realistic results, arrays consisting of dual-polarized infinitely thin $\lambda/2$-dipoles are considered. As the radiation patterns of the antennas in such an array vary between the antennas, gain instead of array gain needs to be considered.

One of the contributions of this thesis is also to make some ideas that might be known in the antennas and propagation community accessible to the communications and signal processing community.

2. Physically Consistent Modeling

Physically consistent modeling deals with how to model a wireless communication system with multiple antennas in a physically consistent way. Consider a transmitter with N antennas and a receiver with M antennas that communicate with each other over a frequency-flat channel with additive noise. The typical conventional model is [17, Ch. 1]

$$\boldsymbol{y} = \boldsymbol{H}\boldsymbol{x} + \boldsymbol{\vartheta}, \tag{2.1}$$

where $\boldsymbol{y} \in \mathbb{C}^M$ is related to the signal at the output of the analog-to-digital converters (ADCs), $\boldsymbol{H} \in \mathbb{C}^{M\times N}$ is the channel matrix, $\boldsymbol{x} \in \mathbb{C}^N$ is related to the signal at the input of the digital-to-analog converters (DACs) and $\boldsymbol{\vartheta} \in \mathbb{C}^M$ is additive noise. It is assumed that the transmit power P_T is $\mathrm{E}[\|\boldsymbol{x}\|_2^2]$. In order to compute the physical power however, a conjugated pair of vectors is needed [18], e.g., voltage and current.

The physically consistent modeling used in this dissertation is based on circuit theory. In particular the so-called Multiport Communication Theory [8, 9] is employed, which shows how to encode voltages and currents into $\boldsymbol{x}$, $\boldsymbol{H}$ and $\boldsymbol{y}$ such that the transmit power P_T is really $\mathrm{E}[\|\boldsymbol{x}\|_2^2]$, and such that the noise $\boldsymbol{\vartheta}$ is modeled in a physically consistent way. Circuit theory is attractive for modeling the noise from various noise sources [8]. This theory is in turn based on a circuit-theoretical description using impedance matrices and provides a way to model the system consistently with physics. The circuit model can equivalently be described using scattering matrices, similar to the models [6, 7], which to the authors' best knowledge were the first to take into account that mutual coupling changes the transmit power. The model in [6] was later extended by a detailed amplifier noise model [19]. Two similar noise models that contain both antenna and amplifier noise are introduced in [8, 9], and [20]. The key contributions of [8] and [9] are that they merge the circuit model and the noise model, and that they introduce a systematic mapping from the circuit-based models to the usual information-theoretic model.

Fig. 2.1 shows a circuit diagram of the communication system. Going from left to right, it shows the signal generation, the transmit impedance matching, the antennas and their interaction through mutual coupling, the extrinsic noise sources, the receive impedance matching, and the noisy receive chains/amplifiers [8].

This chapter is organized as follows: the following section goes into various matching strategies for the matching networks and Section 2.2 gives an overview of a simple model without DMNs using Multiport Communication theory. Section 2.3 gives an overview of the common uniform arrays considered in this thesis, and Section 2.4 gives an overview on infinitely thin but perfectly conducting $\lambda/2$-dipoles. Section 2.5 shows how to compute the mutual impedance of infinitely thin but perfectly conducting dipoles with arbitrary rotation, Section 2.6 discusses the infinitely thin but

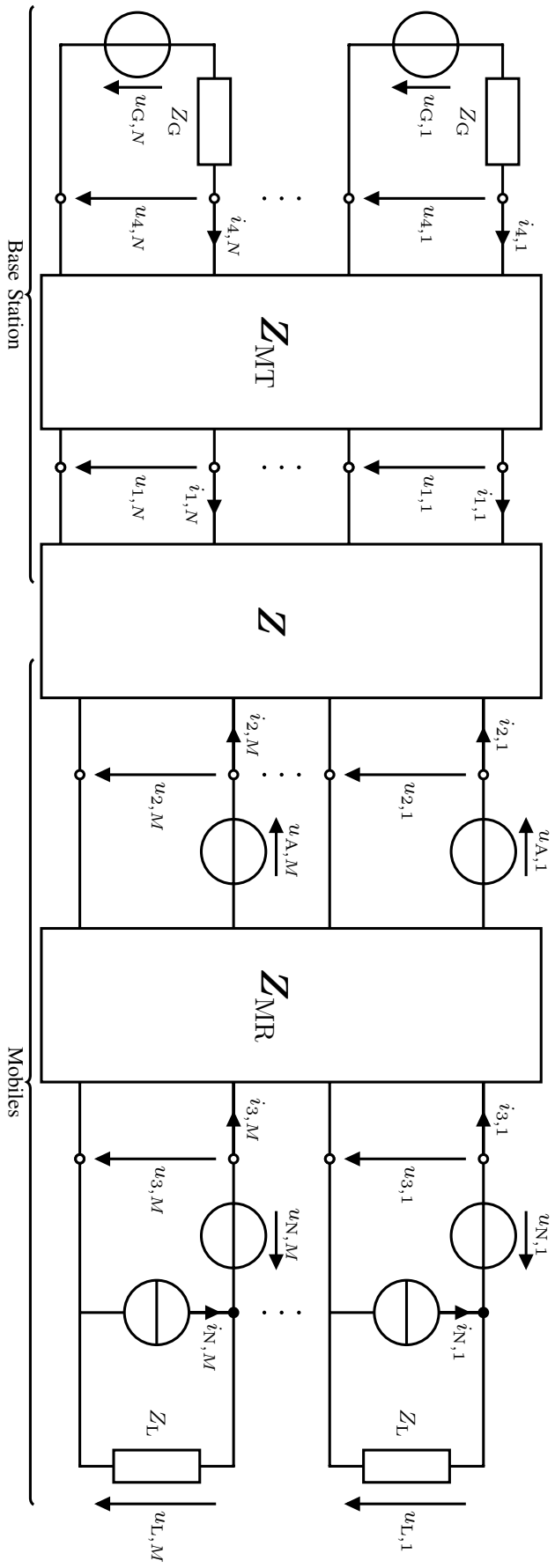

Fig. 2.1. Circuit model with DMNs.

perfectly conducting dipoles that are parallel to a reflector, Section 2.7 presents an antenna array simulated in CST Studio Suite and Section 2.8 provides a conclusion. A large part of Section 2.2 has been published in [21] (©IEEE 2019), and part of Section 2.4 was presented at the 21st International ITG Workshop on Smart Antennas (WSA 2017) [22]. Furthermore, a large part of Section 2.5 was presented at the 24th International ITG Workshop on Smart Antennas (WSA 2020) [23].

2.1 Matching Strategies

The DMNs at the transmitter and at the receiver can be described by the linear multi-ports $\boldsymbol{Z}_{\mathrm{MT}}$ and $\boldsymbol{Z}_{\mathrm{MR}}$ using the impedance matrix description, or equivalently the S-parameter description, or any other. Commonly, it is assumed that the DMN is lossless and reciprocal, because an ideal DMN does not dissipate any power. Reciprocity is desirable, as any lossless reciprocal multi-port can be realized as a Π-network with only inductances and capacitances, see [24]. This means that no active elements are needed. For a given impedance matrix, there are various possibilities to realize them: Π-networks or T-networks can be used for example.

There are various matching strategies for wireless transmitters and receivers. The well-known power matching strategy maximizes the real power flowing from a source with given internal impedance into a load whose input impedance is optimized. Noise matching, which has been known at least since [25], maximizes the SNR. In this dissertation we consider front-ends that are uncoupled, uncorrelated and identical. Noise matching was extended to multi-ports by Warnick and Jensen [26], where it was shown that the DMN that maximizes SNR for arbitrary signals decouples the antenna array and applies noise matching at each output port. Domizioli and Hughes [27] have further shown that such a DMN also maximizes capacity in various point-to-point MIMO additive white Gaussian noise (AWGN) channels.

In general, the number of elements needed to realize a DMN with a generalized Π-network for an N element array is at least $N^2 + N$, see [24]. This is not feasible to implement for large N, because the losses increase with the number of elements and because of the rapidly increasing number of connections between the elements needed.

A two-port matching at the receiver that optimizes the average noise temperature has been studied in [28], and one that maximizes the sum-rates of a MU-SIMO system when there is only noise from the LNAs has been studied in [29, 30]. The optimization of two-port matching at the transmitter, when the available power at the generators is fixed for example, is still an open problem to the author's best knowledge.

A suboptimal broadband transmitter without matching is considered in [31, 32], and compared to a system with DMNs for power matching at the transmitter and noise matching at the receiver. The DMNs are designed at the center frequency. The frequency is swept and the ergodic capacities in an i.i.d. channel for a single frequency are compared. It is shown that depending on how far away the frequency is from the center frequency, capacity can be larger in the system without matching for the same available power, because the DMNs have a limited bandwidth. In [32], it is shown how the DMNs are designed, the comparison is extended to multiple users, and various quality factors of the elements comprising the DMNs are considered. In addition, results are shown for the capacity of the entire channel for various bandwidths.

The practical realization of DMNs has been considered for a long time. In [33, Ch. 3], [34], the synthesis and realization of DMNs for symmetric three ports is considered, in particular for a 3 element UCA consisting of monopoles on a ground plane.

2.2 Multiport Communication Theory

This section provides on overview of Multiport Communication Theory. It introduces a simple circuit model, and then details a mapping from the circuit-theoretic model to the information-theoretic model.

2.2.1 Circuit-Theoretic Model

We focus on a simple circuit model (Fig. 2.2) for the fading channel by assuming that the fading is flat within a narrowband (group of) subcarrier(s) of a multicarrier system[1], similar to the ones in [8], [9, Fig. 9] and [13, 35], where simple means that as in [13, 35], we omit the lossless DMNs, because in massive MIMO systems, they could be almost impossible to implement. But as in [8, 9] and [13], we also consider the thermal noise of the antennas.

The signal generation at the transmitter is modeled as a linear voltage source $u_{\mathrm{G},n}$ with internal impedance Z_{G} per antenna. The antennas are assumed to be lossless [9] and their coupling and the physical channel are modeled jointly by an impedance matrix $\boldsymbol{Z}$. At the receivers, each hardware chain is modeled by an impedance Z_{L} and several noise sources, which we will come back to later.

Let there be in total N antennas at the transmitter(s) and M at the receiver(s). As antennas and the physical channel are reciprocal [36], the system described by the impedance matrix $\boldsymbol{Z} \in \mathbb{C}^{(N+M)\times(N+M)} \cdot \Omega$ is symmetric, i.e.,

$$\boldsymbol{Z} = \boldsymbol{Z}^T. \tag{2.2}$$

It is partitioned into four blocks [8]: the transmit and receive impedance matrices $\boldsymbol{Z}_{11} \in \mathbb{C}^{N\times N} \cdot \Omega$ and $\boldsymbol{Z}_{22} \in \mathbb{C}^{M\times M} \cdot \Omega$, and the mutual impedance matrices $\boldsymbol{Z}_{21} \in \mathbb{C}^{M\times N} \cdot \Omega$ and $\boldsymbol{Z}_{12} \in \mathbb{C}^{N\times M} \cdot \Omega$ such that

$$\begin{bmatrix} \boldsymbol{u}_1 \\ \boldsymbol{u}_2 \end{bmatrix} = \underbrace{\begin{bmatrix} \boldsymbol{Z}_{11} & \boldsymbol{Z}_{12} \\ \boldsymbol{Z}_{21} & \boldsymbol{Z}_{22} \end{bmatrix}}_{\boldsymbol{Z}} \begin{bmatrix} \boldsymbol{i}_1 \\ \boldsymbol{i}_2 \end{bmatrix}, \tag{2.3}$$

where $\boldsymbol{u}_1 \in \mathbb{C}^N \cdot \mathrm{V}, \boldsymbol{i}_1 \in \mathbb{C}^N \cdot \mathrm{A}, \boldsymbol{u}_2 \in \mathbb{C}^M \cdot \mathrm{V}, \boldsymbol{i}_2 \in \mathbb{C}^M \cdot \mathrm{A}$ are the port voltages and currents at the transmitter and receiver side [8] (see Fig. 2.2). All voltages and currents in this paper are rms values of complex envelopes.

Let us consider the relation between the generator and load voltages $\boldsymbol{u}_{\mathrm{G}} \in \mathbb{C}^N \cdot \mathrm{V}$ and $\boldsymbol{u}_{\mathrm{L}} \in \mathbb{C}^M \cdot \mathrm{V}$. Compared to [8], the relation between voltages and currents at the generator side simplifies to

$$\boldsymbol{u}_{\mathrm{G}} = \boldsymbol{u}_1 + Z_{\mathrm{G}} \boldsymbol{i}_1. \tag{2.4}$$

Using the unilateral approximation $\|\boldsymbol{Z}_{12}\|_{\mathrm{F}} \ll \|\boldsymbol{Z}_{11}\|_{\mathrm{F}}$ [8], whereby we assume that the attenuation of the channel is so high that the currents in the antennas at the receivers do not influence the transmitter, we have [8]

$$\boldsymbol{u}_1 = \boldsymbol{Z}_{11} \boldsymbol{i}_1. \tag{2.5}$$

According to the superposition theorem,

$$\boldsymbol{u}_{\mathrm{L}} = \underbrace{\boldsymbol{u}_{\mathrm{L}}|_{\mathrm{nf}}}_{\text{noise-free}} + \underbrace{\boldsymbol{u}_{\mathrm{L}}|_{\mathrm{sf}}}_{\text{signal-free}} = \boldsymbol{u}_{\mathrm{L}}|_{\mathrm{nf}} + \sqrt{R_{\mathrm{L}}}\boldsymbol{\eta}, \quad R_{\mathrm{L}} \coloneqq \mathrm{Re}(Z_{\mathrm{L}}), \tag{2.6}$$

where $\boldsymbol{\eta}$ describes the noise, see also (2.14). The excitation in the noise-free case is caused by $\boldsymbol{u}_{\mathrm{G}}$,

[1] This is the standard assumption in most of the MIMO literature.

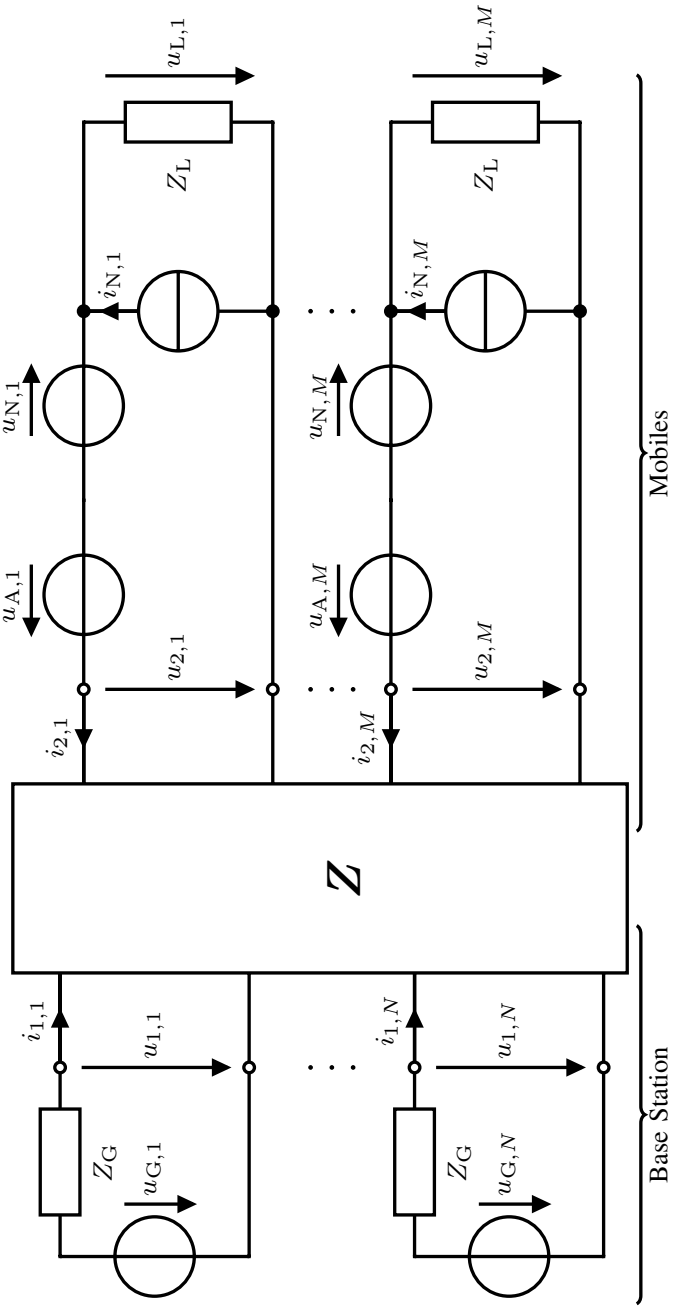

Fig. 2.2. Circuit model in the downlink [21]. (©IEEE 2020)

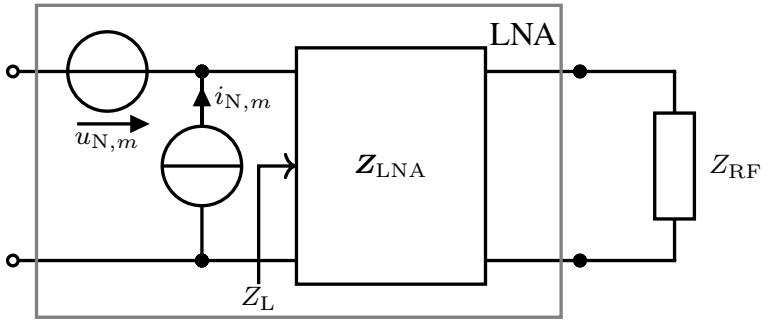

Fig. 2.3. Equivalent circuit of the LNA.

and in the signal-free case by the noise sources. We use the same noise model as in [9], which distinguishes between the extrinsic noise $\boldsymbol{u}_{\mathrm{A}} \in \mathbb{C}^M \cdot \mathrm{V}$ produced by the antennas in thermal equilibrium, and the intrinsic noise, which stems mainly from the LNAs (but also from other components) [8], which can be jointly modeled as noisy two-ports. There is an equivalent model [25] for each of the noisy two-ports consisting of a noiseless two-port with a voltage and a current noise source, $u_{\mathrm{N},m}, i_{\mathrm{N},m}$, at its input, which model the intrinsic noise. Its output port is connected to the next component in the radio frequency (RF) chain, whose input impedance is modeled by a load Z_{RF}, see Fig. 2.3. The SNR at the input and the output of the noiseless two-port is the same and thus it is sufficient to only consider the input port in the model [9]. Based on this model,

$$Z_{\mathrm{L}} = Z_{\mathrm{LNA},11} - \frac{Z_{\mathrm{LNA},12} Z_{\mathrm{LNA},21}}{Z_{\mathrm{LNA},22} + Z_{\mathrm{RF}}}. \tag{2.7}$$

The noise distributions are modeled as [8]

$$\begin{aligned} \boldsymbol{u}_{\mathrm{A}} &\sim \mathcal{N}_{\mathbb{C}}(\boldsymbol{0}\,\mathrm{V}, \boldsymbol{R}_{\mathrm{A}}), \quad \boldsymbol{R}_{\mathrm{A}} = 4k_{\mathrm{B}} T_{\mathrm{A}} \Delta f \,\mathrm{Re}(\boldsymbol{Z}_{22}), \\ \boldsymbol{u}_{\mathrm{N}} &\sim \mathcal{N}_{\mathbb{C}}(\boldsymbol{0}\,\mathrm{V}, \sigma_u^2 \boldsymbol{I}), \qquad \boldsymbol{i}_{\mathrm{N}} \sim \mathcal{N}_{\mathbb{C}}(\boldsymbol{0}\,\mathrm{A}, \sigma_i^2 \boldsymbol{I}) \end{aligned} \tag{2.8}$$

for some $\sigma_u > 0\,\mathrm{V}, \sigma_i > 0\,\mathrm{A}$, where k_{B} is the Boltzmann constant, Δf is the noise bandwidth and T_{A} is the noise temperature of the antennas. In the noise-free case,

$$\boldsymbol{u}_{\mathrm{L}}|_{\mathrm{nf}} = \boldsymbol{u}_2|_{\mathrm{nf}} = \boldsymbol{Z}_{21}\boldsymbol{i}_1 + \boldsymbol{Z}_{22}\boldsymbol{i}_2|_{\mathrm{nf}} = -Z_{\mathrm{L}}\boldsymbol{i}_2|_{\mathrm{nf}}. \tag{2.9}$$

Combining (2.4), (2.5) and (2.9) leads to

$$\boldsymbol{u}_{\mathrm{L}}|_{\mathrm{nf}} = \boldsymbol{D}\boldsymbol{u}_{\mathrm{G}}, \quad \boldsymbol{D} = Z_{\mathrm{L}}(\boldsymbol{Z}_{22} + Z_{\mathrm{L}}\boldsymbol{I})^{-1}\boldsymbol{Z}_{21}(\boldsymbol{Z}_{11} + Z_{\mathrm{G}}\boldsymbol{I})^{-1}. \tag{2.10}$$

In the signal-free case, the intrinsic noise sources $\boldsymbol{u}_{\mathrm{N}}$ and $\boldsymbol{i}_{\mathrm{N}}$ are assumed to be uncorrelated with the extrinsic noise $\boldsymbol{u}_{\mathrm{A}}$. $u_{\mathrm{N},m}$ and $i_{\mathrm{N},m}$ are correlated with the correlation coefficient [8]

$$\rho = \frac{\mathrm{E}[u_{\mathrm{N},m} i_{\mathrm{N},m}^*]}{\sigma_u \sigma_i} \quad \forall m. \tag{2.11}$$

Consider the following two equations that follow from Kirchhoff's voltage and current law:

$$-\boldsymbol{u}_{\mathrm{A}} + \boldsymbol{u}_{\mathrm{N}} + \boldsymbol{u}_{\mathrm{L}}|_{\mathrm{sf}} = \boldsymbol{Z}_{22}\boldsymbol{i}_2|_{\mathrm{sf}}, \tag{2.12}$$

$$\boldsymbol{i}_2|_{\mathrm{sf}} = \boldsymbol{i}_{\mathrm{N}} - Z_{\mathrm{L}}^{-1}\boldsymbol{u}_{\mathrm{L}}|_{\mathrm{sf}}. \tag{2.13}$$

Eliminating $\boldsymbol{i}_2|_{\mathrm{sf}}$ and solving for $\boldsymbol{u}_{\mathrm{L}}|_{\mathrm{sf}}$ gives the relation between $\boldsymbol{\eta}$ and the noise sources

$$\boldsymbol{\eta} = \frac{\boldsymbol{u}_{\mathrm{L}}|_{\mathrm{sf}}}{\sqrt{R_{\mathrm{L}}}} = \frac{Z_{\mathrm{L}}}{\sqrt{R_{\mathrm{L}}}}(\boldsymbol{Z}_{22} + Z_{\mathrm{L}}\boldsymbol{I})^{-1}(\boldsymbol{u}_{\mathrm{A}} - \boldsymbol{u}_{\mathrm{N}} + \boldsymbol{Z}_{22}\boldsymbol{i}_{\mathrm{N}}). \tag{2.14}$$

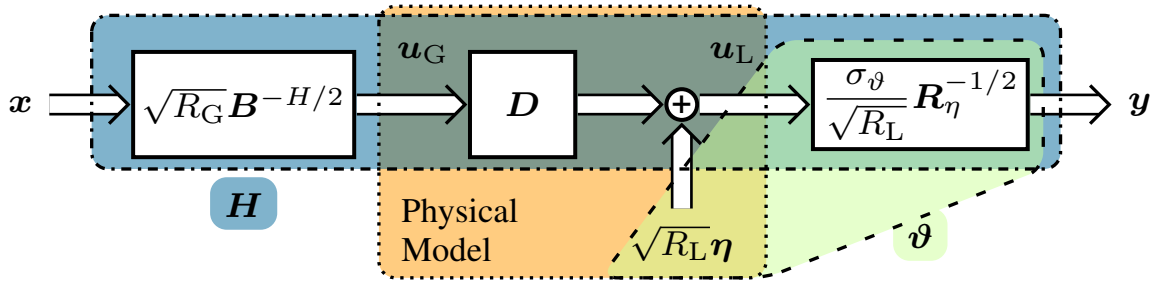

Fig. 2.4. System model showing the relation between the physical and the information-theoretic model [21]. (©IEEE 2020)

Together with (2.8) and (2.11), the noise covariance matrix can be computed as

$$\begin{aligned}\boldsymbol{R}_\eta &= \mathrm{E}[\boldsymbol{\eta}\boldsymbol{\eta}^H] = \frac{|Z_\mathrm{L}|^2}{R_\mathrm{L}}(\boldsymbol{Z}_{22}+Z_\mathrm{L}\boldsymbol{I})^{-1}\boldsymbol{Q}(\boldsymbol{Z}_{22}+Z_\mathrm{L}\boldsymbol{I})^{-H},\\ \boldsymbol{Q} &= \sigma_u^2\boldsymbol{I}+\sigma_i^2\boldsymbol{Z}_{22}\boldsymbol{Z}_{22}^*-2\sigma_u\sigma_i\,\mathrm{Re}(\rho^*\boldsymbol{Z}_{22})+\boldsymbol{R}_\mathrm{A}.\end{aligned} \tag{2.15}$$

The transmit power in the physical model can be computed as

$$\begin{aligned}P_\mathrm{T} &= \mathrm{E}[\mathrm{Re}(\boldsymbol{i}_1^H\boldsymbol{u}_1)] = \frac{\mathrm{E}[\boldsymbol{u}_\mathrm{G}^H\boldsymbol{B}\boldsymbol{u}_\mathrm{G}]}{R_\mathrm{G}}, \quad R_\mathrm{G} \coloneqq \mathrm{Re}(Z_\mathrm{G}),\\ \boldsymbol{B} &= R_\mathrm{G}(\boldsymbol{Z}_{11}+Z_\mathrm{G}\boldsymbol{I})^{-H}\,\mathrm{Re}(\boldsymbol{Z}_{11})(\boldsymbol{Z}_{11}+Z_\mathrm{G}\boldsymbol{I})^{-1},\end{aligned} \tag{2.16}$$

where we have used (2.4) and where $\boldsymbol{B}$ is the so-called power-coupling matrix [8]. Then the complete physical model is

$$\boldsymbol{u}_\mathrm{L} = \boldsymbol{D}\boldsymbol{u}_\mathrm{G}+\sqrt{R_\mathrm{L}}\boldsymbol{\eta}, \quad \boldsymbol{\eta}\sim\mathcal{N}_\mathbb{C}(\boldsymbol{0}\sqrt{\mathrm{W}},\boldsymbol{R}_\eta), \qquad P_\mathrm{T} = \frac{\mathrm{E}[\boldsymbol{u}_\mathrm{G}^H\boldsymbol{B}\boldsymbol{u}_\mathrm{G}]}{R_\mathrm{G}}. \tag{2.17}$$

2.2.2 Information-Theoretic Model

Consider the typical information-theoretic model (e.g., [17, Ch. 1])

$$\boldsymbol{y} = \boldsymbol{H}\boldsymbol{x}+\boldsymbol{\vartheta}, \quad \boldsymbol{\vartheta}\sim\mathcal{N}_\mathbb{C}(\boldsymbol{0}\sqrt{\mathrm{W}},\sigma_\vartheta^2\boldsymbol{I}), \quad \sigma_\vartheta > 0\sqrt{\mathrm{W}}, \quad P_\mathrm{T} = \mathrm{E}[\boldsymbol{x}^H\boldsymbol{x}], \tag{2.18}$$

which allows existing techniques and results for capacity and achievable rates to be easily drawn on. In order to get a physically consistent information-theoretic model, we need to ensure that the transmit power P_T and the noise covariance are consistent with the physical model (2.17). This can be achieved by a linear mapping from $\boldsymbol{u}_\mathrm{G}$ and $\boldsymbol{u}_\mathrm{L}$ to $\boldsymbol{x}$ and $\boldsymbol{y}$,

$$\boldsymbol{x} = \frac{1}{\sqrt{R_\mathrm{G}}}\boldsymbol{B}^{H/2}\boldsymbol{u}_\mathrm{G}, \qquad \text{s.t.} \quad \boldsymbol{B} = \boldsymbol{B}^{1/2}\boldsymbol{B}^{H/2}, \tag{2.19}$$

$$\boldsymbol{y} = \frac{\sigma_\vartheta}{\sqrt{R_\mathrm{L}}}\boldsymbol{R}_\eta^{-1/2}\boldsymbol{u}_\mathrm{L}, \qquad \text{s.t.} \quad \boldsymbol{R}_\eta = \boldsymbol{R}_\eta^{1/2}\boldsymbol{R}_\eta^{H/2}, \tag{2.20}$$

as shown in [8,9] and leads to the system model shown in Fig. 2.4. Throughout the paper, we assume that matrix square roots in general fulfill a condition similar to (2.19). The expressions are not

Fig. 2.5. ULA with $N = 5$.

exactly the same as in [8, 9], because $\boldsymbol{B}^{1/2}$ is not unique and in these two papers, only $\boldsymbol{B}^{1/2}$ that are Hermitian are considered. We choose

$$\boldsymbol{B}^{1/2} = \sqrt{R_{\mathrm{G}}}(\boldsymbol{Z}_{11} + Z_{\mathrm{G}}\boldsymbol{I})^{-H}\,\mathrm{Re}(\boldsymbol{Z}_{11})^{1/2} \quad \text{s.t.} \quad \mathrm{Re}(\boldsymbol{Z}_{11}) = \mathrm{Re}(\boldsymbol{Z}_{11})^{1/2}\,\mathrm{Re}(\boldsymbol{Z}_{11})^{1/2}, \tag{2.21}$$

$$\boldsymbol{R}_{\eta}^{1/2} = \frac{Z_{\mathrm{L}}}{\sqrt{R_{\mathrm{L}}}}(\boldsymbol{Z}_{22} + Z_{\mathrm{L}}\boldsymbol{I})^{-1}\boldsymbol{Q}^{1/2}. \tag{2.22}$$

This leads to the information-theoretic channel

$$\boldsymbol{H} = \sigma_{\vartheta}\frac{\sqrt{R_{\mathrm{G}}}}{\sqrt{R_{\mathrm{L}}}}\boldsymbol{R}_{\eta}^{-1/2}\boldsymbol{D}\boldsymbol{B}^{-H/2} = \sigma_{\vartheta}\boldsymbol{Q}^{-1/2}\boldsymbol{Z}_{21}\,\mathrm{Re}(\boldsymbol{Z}_{11})^{-1/2}, \tag{2.23}$$

which captures the physical context [8, 9]. σ_{ϑ} is an arbitrary scaling, but to ensure that the sum noise powers in the physical and information-theoretic models are the same, i.e.,

$$\mathrm{E}[\boldsymbol{\vartheta}^H\boldsymbol{\vartheta}] = \mathrm{E}[\boldsymbol{\eta}^H\boldsymbol{\eta}] \tag{2.24}$$

holds, let

$$\sigma_{\vartheta}^2 = \frac{\mathrm{tr}(\boldsymbol{R}_{\eta})}{M}. \tag{2.25}$$

2.2.3 Neglecting the Mutual Coupling

There are three matrices that characterize the information-theoretic channel $\boldsymbol{H}$, namely $\boldsymbol{B}$, $\boldsymbol{D}$ and $\boldsymbol{R}_{\eta}$. The matrix $\boldsymbol{D}$ can be estimated with the help of pilot symbols. Independent of whether the mutual coupling is neglected or not, the estimate related to perfect CSI knowledge is always the same $\boldsymbol{D}$. It is the only matrix of the three that is time-variant due to user mobility. The other two are time-invariant. $\boldsymbol{B}$ is a function of Z_{G} and $\boldsymbol{Z}_{11}$ – or equivalently the scattering parameters – which can be determined by off-line modeling, simulation or measurement of the antenna arrays, including the front/back end of the RF chains. In many publications, mutual coupling is ignored, meaning that $\boldsymbol{B}$ and $\boldsymbol{R}_{\eta}$ are assumed to be diagonal or scaled identity matrices (see Section 3.3). Acquiring $\boldsymbol{R}_{\eta}$ is further discussed in the following section.

2.3 Common Uniform Antenna Arrays

In this thesis, ULAs, UCAs and URAs are considered. ULAs are very common in the signal processing and wireless communications literature. A ULA consists of antennas spaced uniformly on a line, i.e., the position of the n-th antenna is

$$x_n = nd, \quad y_n = 0, \tag{2.26}$$

where d is the antenna separation. For a UCA with N antennas, the antennas are located at

$$x_n = r\cos\left(\frac{2\pi}{N}n\right), \quad y_n = r\sin\left(\frac{2\pi}{N}n\right), \qquad n = 0, \ldots, N-1. \tag{2.27}$$

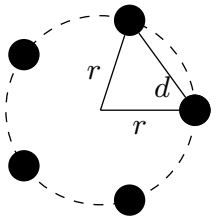

Fig. 2.6. UCA with $N = 5$.

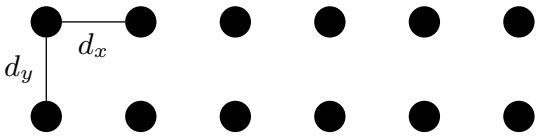

Fig. 2.7. URA with $N_x = 6, N_y = 2$.

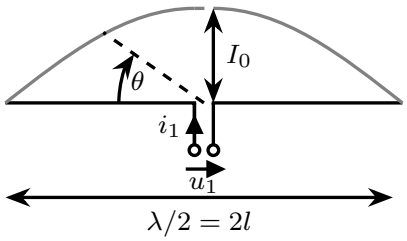

Fig. 2.8. Infinitely thin but perfectly conducting $\lambda/2$-dipole with a sinusoidal current distribution.

The antenna separation d and its radius r are related by

$$\frac{\pi}{N} = \sin\left(\frac{d}{2r}\right). \tag{2.28}$$

For a URA with N_x antennas in the x-direction and N_y antennas in the y-direction, the position of the n-th antenna is given by

$$x_n = n_x d_x, \qquad n_x = 0, \ldots, N_x - 1, \tag{2.29a}$$
$$y_n = n_y d_y, \qquad n_y = 0, \ldots, N_y - 1. \tag{2.29b}$$

2.4 Infinitely Thin but Perfectly Conducting λ/2-dipoles

The self-impedance of an infinitely thin but perfectly conducting $\lambda/2$-dipole is given by [36, Ch. 13], as well as the mutual impedance between two of these dipoles that are parallel. For this kind of dipole, the current distribution is commonly approximated to be sinusoidal on the dipole, see Fig. 2.8. As they are canonical minimum scattering antennas [37, 38], the entries of the impedance matrix $\boldsymbol{Z}$ of an array of parallel $\lambda/2$-dipoles can be computed independently, because they do not influence each other when they are terminated by an open circuit. This is similar to arrays of $\lambda/4$-monopoles as shown in [13] (which is based on [36, Ch. 13]). The mutual impedance between antennas i and j situated $d_{i,j}$ apart is

$$\begin{aligned} Z_{i,j} = \frac{Z_0}{4\pi}\Big(&2\,\mathrm{Ci}(2\pi d_{i,j}/\lambda) - \mathrm{Ci}(\zeta_{i,j} + \pi) - \mathrm{Ci}(\zeta_{i,j} - \pi) \\ &+ j\big(\mathrm{Si}(\zeta_{i,j} + \pi) + \mathrm{Si}(\zeta_{i,j} - \pi) - 2\,\mathrm{Si}(2\pi d_{i,j}/\lambda)\big)\Big), \end{aligned}$$

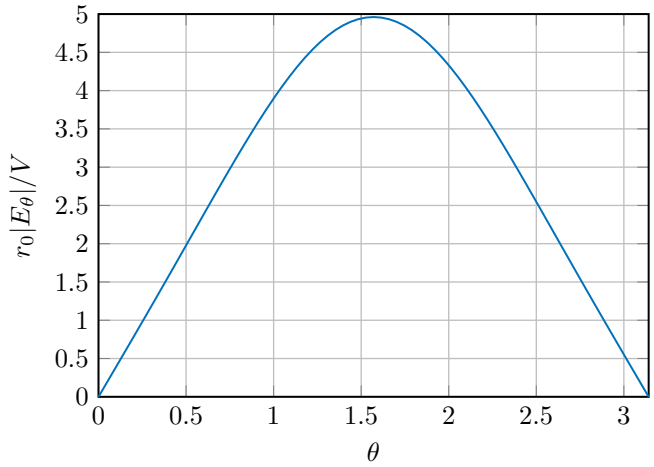

Fig. 2.9. Radiation pattern of an infinitely thin $\lambda/2$-dipole with a radiated power of $P_{\text{rad}} = 1/2\,\text{W}$.

$$\zeta_{i,j} = \pi\sqrt{1 + 4d_{i,j}^2/\lambda^2}, \quad Z_0 = \sqrt{\frac{\mu_0}{\varepsilon_0}} \approx 120\pi\,\Omega \tag{2.30}$$

and the impedance of each dipole is

$$Z_{\lambda/2} = \frac{Z_0}{4\pi}\big(\,\text{Cin}(2\pi) + j\,\text{Si}(2\pi)\big), \tag{2.31}$$

where Z_0 is the impedance of free space, Si, Ci and Cin are the sine and cosine integrals [36, (6-52)] [39, Ch. 6]

$$\begin{aligned} \text{Si}(x) &= \int_0^x \frac{\sin(t)}{t}dt, \qquad \text{Cin}(x) = \int_0^x \frac{1-\cos(t)}{t}dt, \\ \text{Ci}(x) &= \gamma + \ln(x) - \text{Cin}(x) = -\int_x^\infty \frac{\cos(t)}{t}dt \end{aligned} \tag{2.32}$$

and γ is the Euler-Mascheroni constant.

An infinitely thin but perfectly conducting $\lambda/2$-dipole that is excited by the current I_0 generates the (field) radiation pattern on a sphere with radius r_0 around it given by [36, Section 11.2] (in the far-field)

$$E_\theta(\theta) r_0 e^{jkr_0} = jI_0\frac{Z_0}{2\pi}\frac{\cos(kl\cos(\theta)) - \cos(kl)}{\sin(\theta)}, \quad l = \lambda/4, \tag{2.33}$$

where $2l$ is the length of the dipole, see Figs. 2.8 and 2.9, and k is the angular wavenumber. The corresponding radiated power is given by

$$P_{\text{rad}} = |I_0|^2\,\text{Re}(Z_{\lambda/2}). \tag{2.34}$$

2.5 Mutual Impedance of Infinitely Thin but Perfectly Conducting Dipoles with Arbitrary Orientation

As infinitely thin but perfectly conducting dipoles are canonical minimum scattering antennas [37,38], the mutual impedance matrix can be computed by considering two dipoles at a time.

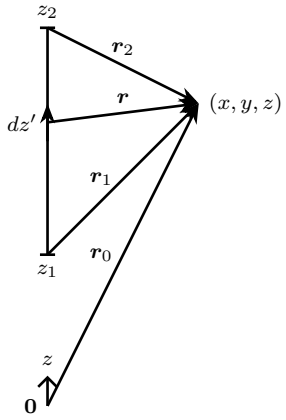

Fig. 2.10. Illustration of the integration path to obtain the electric field of the current filament.

Consider a straight sinusoidal current filament on the z-axis extending from $z = z_1$ to $z = z_2$, with current distribution $i(z)$, which corresponds to the current density

$$\boldsymbol{J}_\mathrm{f} = \boldsymbol{e}_z \delta(x)\delta(y)i(z), \tag{2.35}$$

where $\delta(x)$ is the Dirac delta distribution. The magnetic vector potential $\boldsymbol{A}_\mathrm{f}$ at the point with position vector $\boldsymbol{r}_0$ produced by this current density is given by [40, Ch. 4.7]

$$\boldsymbol{A}_\mathrm{f} = \frac{Z_0}{c}\int_{z_1}^{z_2} i(z')\Psi dz' \boldsymbol{e}_z, \qquad \Psi = \frac{e^{-jkr}}{4\pi r}, \quad r = \|\boldsymbol{r}\|, \quad \boldsymbol{r} = \boldsymbol{r}_0 - z'\boldsymbol{e}_z, \tag{2.36}$$

where $\boldsymbol{e}_z$ is the unit vector in z-direction and c is the speed of light. The corresponding electric field in z-direction, $E_{\mathrm{f},z}$, at $\boldsymbol{r}_0$ is given by [36, Ch. 12.7]

$$\begin{aligned} E_{\mathrm{f},z} &= \frac{jZ_0}{4\pi k}\left[i'(z_2)\frac{e^{-jkr_2}}{r_2} - i'(z_1)\frac{e^{-jkr_1}}{r_1} + i(z_2)\frac{\partial e^{-jkr_2}}{\partial z r_2} - i(z_1)\frac{\partial e^{-jkr_1}}{\partial z r_1}\right], \\ \boldsymbol{r}_1 &= \boldsymbol{r}_0 - z_1\boldsymbol{e}_z, \quad r_1 = \|\boldsymbol{r}_1\|_2, \\ \boldsymbol{r}_2 &= \boldsymbol{r}_0 - z_2\boldsymbol{e}_z, \quad r_2 = \|\boldsymbol{r}_2\|_2, \end{aligned} \tag{2.37}$$

where $i'(z)$ is the derivative of $i(z)$. The derivation of $E_{\mathrm{f},x}$, $E_{\mathrm{f},y}$ follows similar steps as the derivation of $E_{\mathrm{f},z}$ in [36, Ch. 12.6, 12.7] and [40, Ch. 4.7]. Based on [40, Ch. 4.7], the electric field generated by $\boldsymbol{A}_\mathrm{f}$ is

$$\boldsymbol{E}_\mathrm{f} = -jck\boldsymbol{A}_\mathrm{f} - \frac{jc}{k}\operatorname{grad}(\operatorname{div}(\boldsymbol{A}_\mathrm{f})). \tag{2.38}$$

This means, the x-component $E_{\mathrm{f},x}$ for a straight current filament on the z-axis is given by

$$E_{\mathrm{f},x} = \frac{Z_0}{jk}\int_{z_1}^{z_2} i(z')\frac{\partial^2\Psi}{\partial x\partial z}dz' = \frac{jZ_0}{k}\int_{z_1}^{z_2} i(z')\frac{\partial^2\Psi}{\partial x\partial z'}dz', \quad x = \boldsymbol{r}\cdot\boldsymbol{e}_x, \tag{2.39}$$

where the second equality holds because

$$\frac{\partial^2\Psi}{\partial x\partial z} = -\frac{\partial^2\Psi}{\partial x\partial z'}. \tag{2.40}$$

The integration path is illustrated in Fig. 2.10. $E_{\mathrm{f},x}$ can be simplified by partial integration,

$$E_{\mathrm{f},x} = \frac{jZ_0}{k} \int_{z_1}^{z_2} i(z') \frac{\partial^2 \Psi}{\partial x \partial z'} dz' = \frac{jZ_0}{k} \left[i(z') \frac{\partial \Psi}{\partial x} \right]_{z_1}^{z_2} - \frac{jZ_0}{k} \int_{z_1}^{z_2} i'(z') \frac{\partial \Psi}{\partial x} dz', \tag{2.41}$$

where

$$\frac{\partial \Psi}{\partial x} = -\frac{\Psi x}{r^2}(1 + jkr). \tag{2.42}$$

and similarly for $E_{\mathrm{f},y}$.

For a dipole of length $2l$ with a center gap of length $2l_{\mathrm{g}}$, there is one current filament on the z-axis for each of both arms, i.e., E_x of such a dipole can be obtained by superposition of the fields of both arms, i.e.,

$$E_x = E_{\mathrm{f},x}|_{z_1=l_{\mathrm{g}}}^{z_2=l} + E_{\mathrm{f},x}|_{z_1=-l}^{z_2=-l_{\mathrm{g}}} \tag{2.43}$$

and similarly for E_y and E_z. Consider the sinusoidal current distribution on the dipole and its derivative given by

$$i(z) = \begin{cases} I_0 \sin(k(l - |z|)) & l_{\mathrm{g}} \leq |z| \leq l, \\ 0 & \text{else}, \end{cases} \tag{2.44}$$

$$i'(z) = \frac{di(z)}{dz} = \begin{cases} -kI_0 \cos(k(l - |z|)) & l_{\mathrm{g}} \leq z \leq l, \\ kI_0 \cos(k(l - |z|)) & -l \leq z \leq -l_{\mathrm{g}}, \\ 0 & \text{else}, \end{cases} \tag{2.45}$$

similar to the distribution on a dipole without center gap [36, Ch. 13.2], because the current is distributed sinusoidally on infinitely thin conductors and is zero at the open ends of the dipole.

For E_x, E_y, the first summand in (2.41) contributes

$$\frac{jZ_0}{k} \left(i(l) \frac{\partial \Psi}{\partial x}(l) - i(l_{\mathrm{g}}) \frac{\partial \Psi}{\partial x}(l_{\mathrm{g}}) + i(-l_{\mathrm{g}}) \frac{\partial \Psi}{\partial x}(-l_{\mathrm{g}}) - i(-l) \frac{\partial \Psi}{\partial x}(-l) \right) = 0, \tag{2.46}$$

as $i(l) = i(-l) = 0$, $i(l_{\mathrm{g}}) = i(-l_{\mathrm{g}})$ and $\frac{\partial \Psi}{\partial x}(l_{\mathrm{g}}) = \frac{\partial \Psi}{\partial x}(-l_{\mathrm{g}})$. When we plug the remaining second summand of (2.41) into (2.43), as well as (2.42) and (2.45),

$$\begin{aligned} E_x = &- \frac{jZ_0}{4\pi} I_0 \int_{l_{\mathrm{g}}}^{l} \cos(k(l - z')) \frac{e^{-jkr} x}{r^3} (1 + jkr) dz' \\ &+ \frac{jZ_0}{4\pi} I_0 \int_{-l}^{-l_{\mathrm{g}}} \cos(k(l + z')) \frac{e^{-jkr} x}{r^3} (1 + jkr) dz'. \end{aligned} \tag{2.47}$$

E_y can be obtained in a similar way. E_z can be obtained in a similar way as in [36, Ch. 12.7].

$$\begin{aligned} E_z = &\frac{jZ_0}{4\pi k} \left[i'(l) \frac{e^{-jkr_2}}{r_2} - i'(l_{\mathrm{g}}) \frac{e^{-jkr_{2\mathrm{g}}}}{r_{2\mathrm{g}}} - i(l_{\mathrm{g}}) \frac{\partial}{\partial z} \frac{e^{-jkr_{2\mathrm{g}}}}{r_{2\mathrm{g}}} \right. \\ &\left. + i'(-l_{\mathrm{g}}) \frac{e^{-jkr_{1\mathrm{g}}}}{r_{1\mathrm{g}}} - i'(-l) \frac{e^{-jkr_1}}{r_1} + i(-l_{\mathrm{g}}) \frac{\partial}{\partial z} \frac{e^{-jkr_{1\mathrm{g}}}}{r_{1\mathrm{g}}} \right] \end{aligned} \tag{2.48}$$

as $i(l) = i(-l) = 0$. After plugging in (2.44) and (2.45), we obtain

$$\begin{aligned} E_z =& \frac{jZ_0}{4\pi} I_0 \Bigg[-\frac{e^{-jkr_2}}{r_2} - \frac{e^{-jkr_1}}{r_1} + \cos(k(l-l_\mathrm{g})) \left(\frac{e^{-jkr_{2\mathrm{g}}}}{r_{2\mathrm{g}}} + \frac{e^{-jkr_{1\mathrm{g}}}}{r_{1\mathrm{g}}} \right) \\ &+ \sin(k(l-l_\mathrm{g})) \left(\frac{e^{-jkr_{2\mathrm{g}}}}{r_{2\mathrm{g}}^3} \frac{1+jkr_{2\mathrm{g}}}{k} (z+l_\mathrm{g}) - \frac{e^{-jkr_{1\mathrm{g}}}}{r_{1\mathrm{g}}^3} \frac{1+jkr_{1\mathrm{g}}}{k} (z-l_\mathrm{g}) \right) \Bigg]. \end{aligned} \tag{2.49}$$

For a dipole with infinitely small center gap, i.e., $l_\mathrm{g} = 0$, (2.49) can be simplified to [36, Ch. 13.2]

$$E_z = \frac{jZ_0}{4\pi} I_0 \left[2\cos(kl) \left(\frac{e^{-jkr_{2\mathrm{g}}}}{r_{2\mathrm{g}}} \right) - \frac{e^{-jkr_2}}{r_2} - \frac{e^{-jkr_1}}{r_1} \right], \quad r_{2\mathrm{g}} = r_{1\mathrm{g}} \text{ for } l_\mathrm{g} = 0. \tag{2.50}$$

Consider the mutual impedance between a dipole and another dipole centered around $\boldsymbol{p}_0$. It can be computed as [36, Ch. 12.4]

$$Z_{21} = -\frac{\int_{-l}^{-l_\mathrm{g}} \boldsymbol{E}_1(s) \cdot \boldsymbol{t}_2 \, i_2(s) ds + \int_{l_\mathrm{g}}^{l} \boldsymbol{E}_1(s) \cdot \boldsymbol{t}_2 \, i_2(s) ds}{I_{0,1} I_{0,2} \sin^2(k(l-l_\mathrm{g}))} \tag{2.51}$$

due to reciprocity, where $\boldsymbol{E}_1$ is the electric field produced by the first dipole when it is excited by $I_{0,1}\sin(k(l-l_\mathrm{g}))$, $i_2(s) = i(s)|_{I_0=I_{0,2}}$ is the current distribution on the second dipole when it is excited by $I_{0,2}\sin(k(l-l_\mathrm{g}))$ and $\boldsymbol{t}_2$ is a tangent vector of the second dipole with unit length. For the integration, $\boldsymbol{r}_0$ and x need to be parameterized by s:

$$\boldsymbol{r}_0 = \boldsymbol{p}_0 + s\boldsymbol{t}_2, \qquad x = p_{0,x} + st_{2,x}. \tag{2.52}$$

In order to compute Z_{21} as shown, for the tangent vector of the dipole excited, $\boldsymbol{t}_1 = \boldsymbol{e}_z$ has to hold. For scenarios, where this is not the case, $\boldsymbol{t}_1, \boldsymbol{t}_2$ and $\boldsymbol{r}_0$ can be rotated. Consider the unit vector

$$\boldsymbol{u} = \frac{\boldsymbol{t}_1 \times \boldsymbol{e}_z}{\|\boldsymbol{t}_1 \times \boldsymbol{e}_z\|_2} = \frac{1}{\sqrt{t_{1,x}^2 + t_{1,y}^2}} (t_{1,y}\boldsymbol{e}_x - t_{1,x}\boldsymbol{e}_y). \tag{2.53}$$

$\boldsymbol{t}_1$ is mapped to $\boldsymbol{e}_z$ by a rotation around $\boldsymbol{u}$ by $\alpha \in [0, \pi]$, where

$$\cos(\alpha) = \boldsymbol{t}_1 \cdot \boldsymbol{e}_z = t_{1,z}, \quad \sin(\alpha) = \sqrt{1 - t_{1,z}^2}. \tag{2.54}$$

The rotation matrix for this rotation is given by [41, 42]

$$\boldsymbol{R} = \begin{bmatrix} \frac{t_{1,z}t_{1,x}^2 + t_{1,y}^2}{t_{1,x}^2 + t_{1,y}^2} & \frac{t_{1,x}t_{1,y}(t_{1,z}-1)}{t_{1,x}^2 + t_{1,y}^2} & -t_{1,x} \\ \frac{t_{1,x}t_{1,y}(t_{1,z}-1)}{t_{1,x}^2 + t_{1,y}^2} & \frac{t_{1,x}^2 + t_{1,z}t_{1,y}^2}{t_{1,x}^2 + t_{1,y}^2} & -t_{1,y} \\ t_{1,x} & t_{1,y} & t_{1,z} \end{bmatrix}. \tag{2.55}$$

Then Z_{21} can be computed using $\boldsymbol{R}\boldsymbol{t}_1$, $\boldsymbol{R}\boldsymbol{t}_2$ and $\boldsymbol{R}\boldsymbol{r}_0$ in place of $\boldsymbol{t}_1, \boldsymbol{t}_2$ and $\boldsymbol{r}_0$.

If both dipoles lie in the xz-plane (Fig. 2.11) – possibly after a rotation – $\boldsymbol{t}_2$ can be written as

$$\boldsymbol{t}_2 = \begin{bmatrix} -\sin(\theta_1 + \theta_2) \\ 0 \\ -\cos(\theta_1 + \theta_2) \end{bmatrix}. \tag{2.56}$$

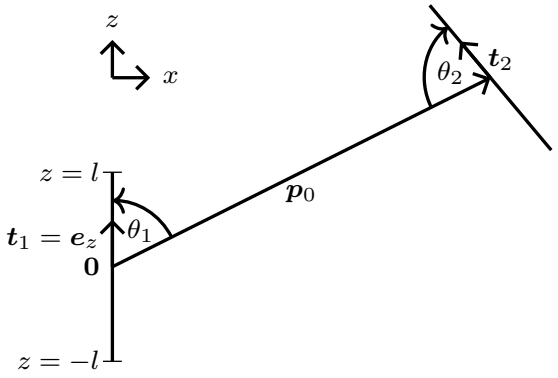

Fig. 2.11. Two dipoles in the xz-plane (based on [23]).

2.6 Dipole in Front of a Reflector

Consider a dipole that is in front of a perfect reflector, and parallel to it. We analyze the scenario by replacing the reflector with an image dipole on the other side of the reflector, which is excited by the same current but with opposite sign. Let $E_{\theta,1}$ be the electric field component of the dipole in θ-direction and $E_{\theta,2}$ that of the image dipole. Let

$$E_\theta = E_{\theta,1} + E_{\theta,2}. \tag{2.57}$$

The electric field for each dipole is given according to (2.33). The total (field) radiation pattern is given by

$$\begin{aligned} E_\theta = \frac{jZ_0 I_0}{2\pi \sin(\theta)} \Bigg[\big(\cos(kl\cos(\theta)) - \cos(kl) \big) \frac{e^{-jkr_0}}{r_0} \\ - \big(\cos(kl\cos(\theta)) - \cos(kl) \big) \frac{e^{-jkr_{02}}}{r_{02}} \Bigg], \end{aligned} \tag{2.58}$$

where θ, φ are the zenith and azimuth angles in the usual spherical coordinate system and I_0 is the current amplitude of the sine describing the current distribution on the dipole, see (2.44).

In the far-field, we assume that $r_0 \approx r_{02}$ and $r_0 - r_{02} \approx 2d\sin(\theta)\cos(\varphi)$, where d is the distance between the dipole and the reflector. Using these assumptions, we can simplify

$$E_\theta = \frac{jZ_0 I_0}{2\pi r_0 \sin(\theta)} \big(\cos(kl\cos(\theta)) - \cos(kl) \big) e^{-jkr_0} \left(1 - e^{2jkd\sin(\theta)\cos(\varphi)} \right). \tag{2.59}$$

The corresponding radiation density is

$$\begin{aligned} \Phi = \frac{|E_\theta r_0|^2}{Z_0} &= \frac{Z_0 I_0^2}{4\pi^2 \sin^2(\theta)} \big(\cos(kl\cos(\theta)) - \cos(kl) \big)^2 |1 - e^{2jkd\sin(\theta)\cos(\varphi)}|^2 \\ &= \frac{Z_0 I_0^2}{4\pi^2 \sin^2(\theta)} \big(\cos(kl\cos(\theta)) - \cos(kl) \big)^2 2\big(1 - \cos(2kd\sin(\theta)\cos(\varphi))\big). \end{aligned} \tag{2.60}$$

The impedance matrix consisting of N dipoles in front of a reflector $\boldsymbol{Z}$ can be obtained from the impedance matrix of the antenna array consisting of the dipoles and the image dipoles $\boldsymbol{Z}_{\text{tot}}$, which can be partitioned into 4 blocks of dimension $N \times N$,

$$\boldsymbol{Z}_{\text{tot}} = \begin{bmatrix} \boldsymbol{Z}_{\text{orig}} & \boldsymbol{Z}_{\text{mutual}} \\ \boldsymbol{Z}_{\text{mutual}}^T & \boldsymbol{Z}_{\text{orig}} \end{bmatrix}, \tag{2.61}$$

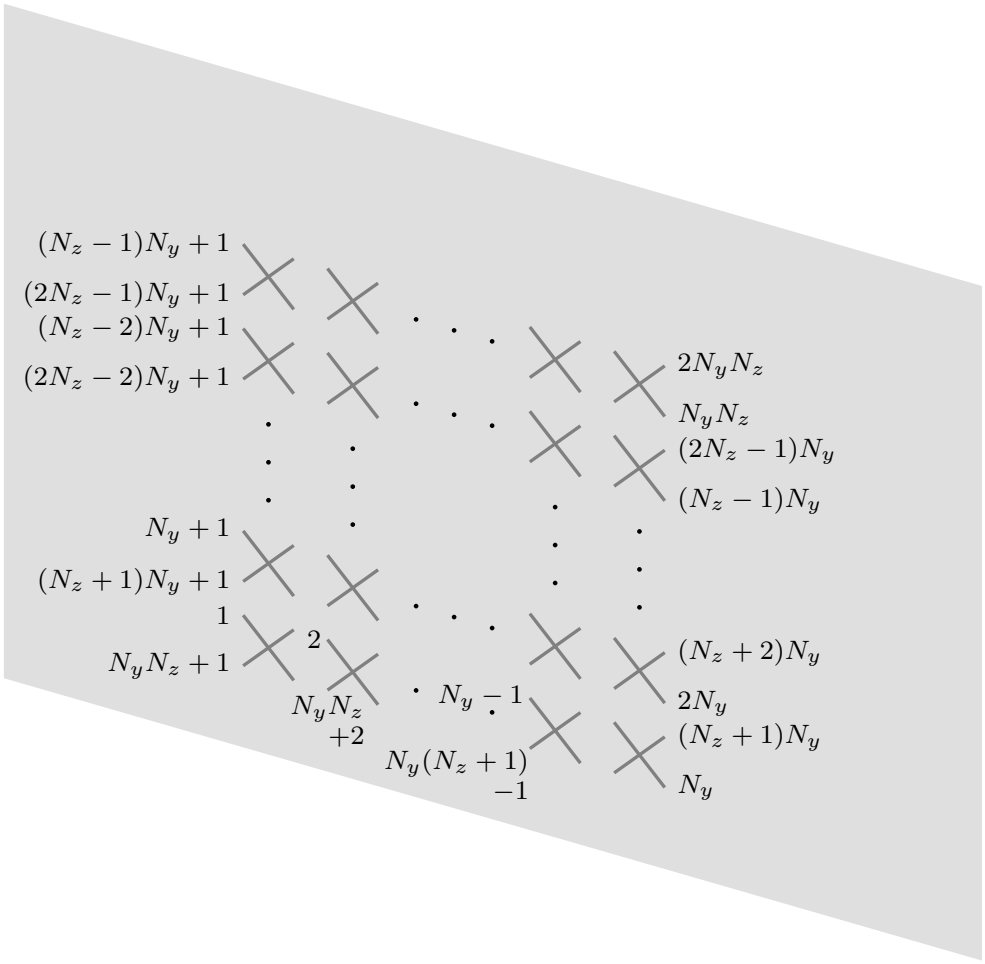

Fig. 2.12. Numbering of the antennas of the URA simulated in CST Studio Suite.

where $\boldsymbol{Z}_{\text{orig}}$ corresponds to the impedance matrix of the original dipoles and that of the image dipoles, and $\boldsymbol{Z}_{\text{mutual}}$ corresponds to the mutual impedance matrix between the original and the image dipoles. According to [36, Section 13.5], $\boldsymbol{Z} = \boldsymbol{Z}_{\text{orig}} - \boldsymbol{Z}_{\text{mutual}}$.

2.7 Antenna Array in CST Studio Suite

In order to evaluate how well our results with infinitely thin dipoles predict how a system with an antenna array consisting of dipoles with a finite thickness behaves, Prof. Thomas Eibert from the Department of Electrical and Computer Engineering, Technical University of Munich conducted a simulation of a 10×10 URA with dual-polarized crossed flat dipoles in CST Studio Suite 2021 using the integral equation solver that provided us with a scattering matrix and the radiation patterns of the antennas at a single frequency, i.e., $N_y = 10$, $N_z = 10$. Table 2.1 gives the important parameters of the array.

Dipoles with a finite thickness are not canonical minimum scattering antennas. Their isolated radiation patterns are different from their embedded radiation patterns, i.e., their radiation patterns when they are part of the array. Furthermore the embedded radiation pattern can vary depending on the position of the antenna element in the array. The radiation patterns with terminated ports were obtained in CST Studio Suite and the radiation patterns with open ports were calculated based

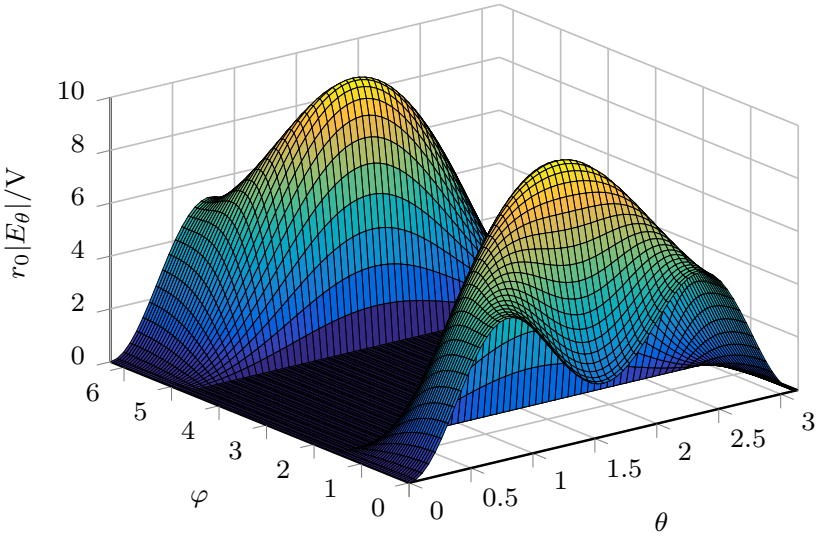

Fig. 2.13. Radiation pattern of a $\lambda/2$-dipole in front of a reflector with distance of about 0.4667λ and an excitation of $P_0 = 1/2\,\mathrm{W}$.

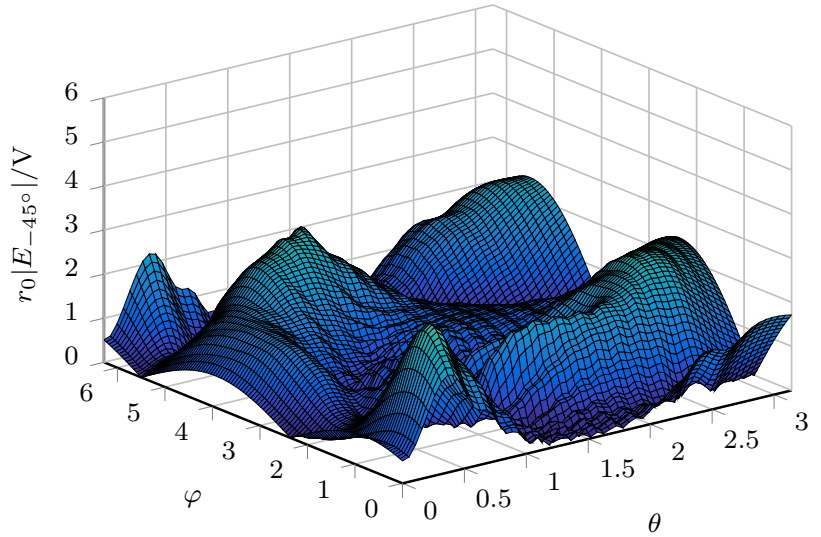

Fig. 2.14. Radiation pattern with open ports of dipole 101 in the CST Studio Suite array at 2.9 GHz in the polarization orthogonal to the dipole with an excitation of $P_0 = 1/2\,\mathrm{W}$.

on them according to [43]. Figs. 2.14 and 2.15 show the radiation pattern with open ports in $\pm 45^\circ$ polarization for dipole number 101 at 2.9 GHz, see Fig. 2.12 for the numbering of the antenna elements. At this frequency, the dipoles are on average $48.25\,\mathrm{mm} \approx 0.4667\lambda$ in front of a reflector and a corresponding infinitely thin but perfectly conducting $\lambda/2$-dipole's radiation pattern in -45° polarization is shown in Fig. 2.13, and its pattern in $+45^\circ$ polarization is zero, i.e., $r_0|E_{+45^\circ}| = 0\,\mathrm{V}$. There are similarities between these radiation patterns and those of the CST Studio Suite dipole number 101, but there are also differences: the -45° polarization radiation pattern is not exactly zero, and there is some radiation into the area behind the reflector in CST Studio Suite.

Regarding the impedance matrices, consider their distance using the metric between their real parts normalized to their self-impedance. We consider only the real part, because the channel $\boldsymbol{H}$ in (2.23) is independent of its imaginary part. We further normalize to their self-impedance, because

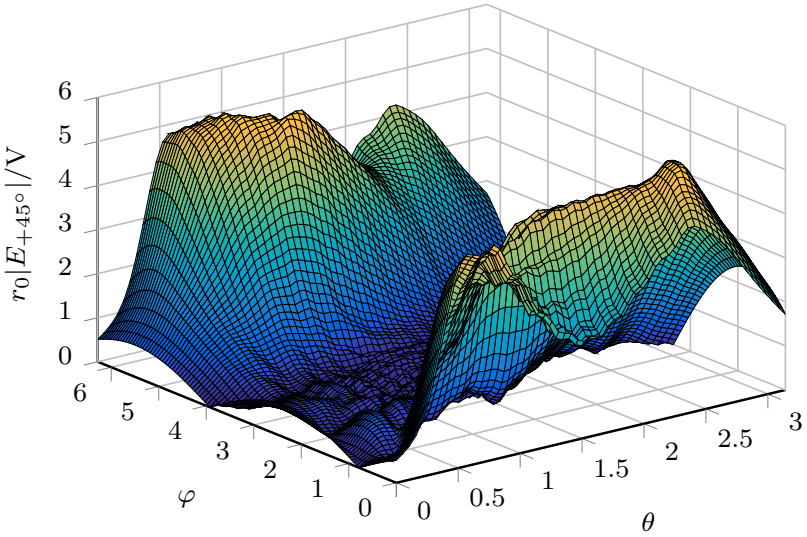

Fig. 2.15. Radiation pattern with open ports of dipole 101 in the CST Studio Suite array at 2.9 GHz in the polarization parallel to the dipole with an excitation of $P_0 = 1/2\,\mathrm{W}$.

Table 2.1. Important parameters of the CST Studio Suite array

Parameter	Value
Center frequency	2.9 GHz
Element spacing	6 cm
Dipole length	5 cm
Distance to reflector	4.8 cm for one polarization and 4.85 cm for the other one
Flat dipole width	0.6738 mm
Reflector dimensions	65 cm × 65 cm
Grid for the radiation pattern	$\varphi = 0, \frac{\pi}{60}, \frac{2\pi}{60}, \ldots, 2\pi, \quad \theta = 0, \frac{\pi}{60}, \frac{2\pi}{60}, \ldots, \pi$

the antenna elements in the CST Studio Suite array and the infinitely thin but perfectly conducting $\lambda/2$-dipoles have different self-impedances, i.e., we compare

$$\boldsymbol{A}_{\mathrm{CST}} = \operatorname{diag}\left(\begin{bmatrix} \sqrt{\operatorname{Re}(Z_{\mathrm{CST},1,1})}^{-1} \\ \sqrt{\operatorname{Re}(Z_{\mathrm{CST},2,2})}^{-1} \\ \vdots \\ \sqrt{\operatorname{Re}(Z_{\mathrm{CST},M,M})}^{-1} \end{bmatrix}\right) \operatorname{Re}(\boldsymbol{Z}_{\mathrm{CST}}) \operatorname{diag}\left(\begin{bmatrix} \sqrt{\operatorname{Re}(Z_{\mathrm{CST},1,1})}^{-1} \\ \sqrt{\operatorname{Re}(Z_{\mathrm{CST},2,2})}^{-1} \\ \vdots \\ \sqrt{\operatorname{Re}(Z_{\mathrm{CST},M,M})}^{-1} \end{bmatrix}\right) \tag{2.62}$$

with the matrix corresponding to the array with infinitely thin but perfectly conducting dipoles $\boldsymbol{A}$. In the latter array, the distance to the reflector is 4.825 cm for all dipoles, and the reflector is infinitely large.

Table 2.2. Geodesic distances between the normalized real parts of the impedance matrices of the antenna array simulated in CST Studio Suite and of the antenna array with infinitely thin but perfectly conducting dipoles, and to the identity matrix

Frequency	$\delta_2(\boldsymbol{A}_{\mathrm{CST}}+\gamma\boldsymbol{I}, \boldsymbol{A}+\gamma\boldsymbol{I})$	$\delta_2(\boldsymbol{A}_{\mathrm{CST}}+\gamma\boldsymbol{I}, (1+\gamma)\boldsymbol{I})$	$\delta_2(\boldsymbol{A}+\gamma\boldsymbol{I}, (1+\gamma)\boldsymbol{I})$
2.9 GHz	22.6	19.2	17.0

Table 2.3. Distances based on the Frobenius norm between the normalized real parts of the impedance matrices of the antenna array simulated in CST Studio Suite and of the antenna array with infinitely thin but perfectly conducting dipoles, and to the identity matrix

Frequency	$d_{\mathrm{F}}(\boldsymbol{A}_{\mathrm{CST}}, \boldsymbol{A})$	$d_{\mathrm{F}}(\boldsymbol{A}_{\mathrm{CST}}, \boldsymbol{I})$	$d_{\mathrm{F}}(\boldsymbol{A}, \boldsymbol{I})$
2.9 GHz	20.9	14.7	13.8

Table 2.4. Distances based on the spectral norm between the normalized real parts of the impedance matrices of the antenna array simulated in CST Studio Suite and of the antenna array with infinitely thin but perfectly conducting dipoles, and to the identity matrix

Frequency	$d_2(\boldsymbol{A}_{\mathrm{CST}}, \boldsymbol{A})$	$d_2(\boldsymbol{A}_{\mathrm{CST}}, \boldsymbol{I})$	$d_2(\boldsymbol{A}, \boldsymbol{I})$
2.9 GHz	4.24	3.30	3.35

For positive definite matrices $\boldsymbol{A}, \boldsymbol{B}$, we can use the geodesic distance [44]

$$\delta_2(\boldsymbol{A}, \boldsymbol{B}) = \sqrt{\sum_{n=1}^{N} \ln^2(\lambda_n(\boldsymbol{A}^{-1}\boldsymbol{B}))}, \tag{2.63}$$

where $\lambda_n(\boldsymbol{A}^{-1}\boldsymbol{B})$ denotes the n-th eigenvalue of $\boldsymbol{A}^{-1}\boldsymbol{B}$. $\boldsymbol{A}$ is positive definite, but $\boldsymbol{A}_{\mathrm{CST}}$ is only positive semidefinite. For a comparison using the geodesic distance, we introduce losses in the antennas by adding a series resistance at each port, which is given by $\gamma\,\mathrm{Re}(Z_{\mathrm{CST},m,m})$ at the m-th port, see also Section 5.2. This corresponds to $\boldsymbol{A}_{\mathrm{CST}}+\gamma\boldsymbol{I}$ and $\boldsymbol{A}+\gamma\boldsymbol{I}$, which are positive definite. In addition, we consider the metric induced by the Frobenius norm $d_{\mathrm{F}}(\boldsymbol{A}, \boldsymbol{B}) = \|\boldsymbol{A}-\boldsymbol{B}\|_{\mathrm{F}}$, and that induced by the spectral norm $d_2(\boldsymbol{A}, \boldsymbol{B}) = \|\boldsymbol{A}-\boldsymbol{B}\|_2$.

The distances between $\boldsymbol{A}_{\mathrm{CST}}$ and $\boldsymbol{A}$, as well as the distance to the identity matrix $\boldsymbol{I}$, which is also a positive definite matrix, and corresponds to an antenna array without mutual coupling, are given in Tables 2.2, 2.3 and 2.4, where $\gamma = 10^{-3}$ was chosen. If the results with infinitely thin dipoles predict the behavior of a system with dipoles of finite thickness well, the distance between $\boldsymbol{A}_{\mathrm{CST}}$ and $\boldsymbol{A}$ should be much smaller than that between $\boldsymbol{A}_{\mathrm{CST}}$ and $\boldsymbol{I}$. Unfortunately, the distances between $\boldsymbol{A}_{\mathrm{CST}}$ and $\boldsymbol{A}$ are larger than the corresponding distances to $\boldsymbol{I}$. Although the simulation gave results that are slightly inconsistent with a passive system due to numerical inaccuracies, as discussed in Section A1, it seems that the impact of the small differences in the geometry of the array as well as the difference between the infinitely thin and the flat dipoles have such an impact.

2.8 Conclusion

In this chapter, we have given an overview of physically consistent modeling based on circuit theory. We have discussed DMNs and introduced a simple model without DMNs. Then, we have provided details on infinitely thin but perfectly conducting dipoles, ULAs, UCAs and URAs. Furthermore, we

discussed the influence of the generators' impedance and the load impedance. In addition, we have derived the mutual impedance between infinitely thin but perfectly conducting dipoles with arbitrary orientation. Moreover, we have presented a comparison between an antenna array consisting of dual-polarized crossed dipoles with finite thickness simulated in CST Studio Suite and one with infinitely thin dipoles.

3. Reciprocity in a TDD System

In this chapter, we consider the reciprocity of the information-theoretic channel of TDD Multi-User-MIMO (MU-MIMO) systems in the up- and downlink. Specifically, we assume that the transmit and receive chains are reciprocal. We take the mutual coupling between the antenna elements at the base station and at the mobiles into account. Mutual coupling influences how to calculate transmit power and noise covariance. The analysis is based on Multiport Communication Theory, which ensures that the information-theoretic model is consistent with physics. It also includes a detailed noise model. We show that due to the coupling, the information-theoretic up- and downlink channels do not fulfill the ordinary reciprocity relation, even if the input-output relation of the transmit voltage sources and the receive load voltages, i.e., the channel which is estimated with the help of pilot signals in the uplink, is reciprocal. This is a fundamental effect that is not considered otherwise. We show via Monte Carlo simulations that both, using the ordinary reciprocity relation, and not taking the coupling into account, significantly decreases the ergodic rates in single-user and the ergodic sum rates in multi-user systems.

3.1 Introduction

Currently deployed wireless standards such as LTE only employ a small number of antennas at the mobiles and at the base station. It is expected that to accommodate further growth of the amount of transferred data, a significantly larger number of antennas needs to be employed at the base station. In order to exploit the degrees of freedom provided by the antennas, the base station requires channel state information (CSI). The amount of CSI increases with the number of antennas. In frequency division duplex (FDD) mode, the base station can usually acquire downlink CSI by sending pilot signals, letting the mobiles estimate the CSI and feed back the estimate. The advantage of TDD mode is that the base station can reuse CSI from the uplink, as the physical channel is reciprocal [45]. The uplink CSI can be acquired with less pilot overhead than the downlink CSI if there are in total fewer antennas at the mobiles than at the base station.

In practical systems, the transmit (Tx) and receive (Rx) RF chains are usually not identical, i.e., up- and downlink channels are not reciprocal. Reciprocity calibration is used to take this into account [46–51]. In some of these papers, the mutual coupling between the antenna elements of the same array is leveraged for the calibration process. But they do not take into account that mutual coupling itself has an impact on the reciprocity relation of the up- and downlink channel matrices in the information-theoretic model. Here we assume that one of the methods for calibrating the RF chains is applied such that those in the uplink and those in the downlink are made equal in the DSP part of the system.

We will show that there is another fundamental source changing the reciprocity relation, namely mutual coupling, using the so-called Multiport Communication Theory [8, 9]. All of these models only consider a one-way link, so it is applied to both up- and downlink in analyzing reciprocity. In conventionally modeled systems, the information-theoretic ordinary (pseudo-physical) reciprocity relation $\boldsymbol{H} = \boldsymbol{H}_{\mathrm{UL}}^T$ is employed, but due to mutual coupling, this relation does not hold, but rather a new physically consistent reciprocity relation. This is because mutual coupling influences how to calculate transmit power and noise covariance.

The rest of this chapter is organized as follows: first we consider the reciprocity of the information-theoretic channel based on the simple circuit-theoretic model in Section 2.2, and show how to take the reciprocity into account in Section 3.2. Then we analyze the effect on the radiated power and on the (sum) rates in the single user multiple input single output (SU-MISO), single user MIMO (SU-MIMO), multi user MISO (MU-MISO) and MU-MIMO downlink, first theoretically, see Section 3.3, and second in simulation in i.i.d. channels and in QuaDRiGa [10, 11] channels, see Sections 3.4 and 3.5. Conclusions follow in Section 3.6.

The SU-MISO case was presented in part at the 21st International ITG Workshop on Smart Antennas (WSA 2017) [22]. A large part of this chapter has been published in [21] (©IEEE 2019), and part of Section 3.5 was presented at the 22nd International ITG Workshop on Smart Antennas (WSA 2018) [52].

3.2 Reciprocity of the Information-Theoretic Channel

In this chapter, we relate the models presented in Section 2.2 to the downlink (Fig. 2.2). The uplink uses a similar model, but with the impedance matrix $\boldsymbol{Z}^T$ and with the noise sources at the base station. $\boldsymbol{Z}_{11}$ describes the antennas at the base station and $\boldsymbol{Z}_{22}$ those at the mobiles. In the following sections, we will assume that $Z_{\mathrm{G}} = Z_{\mathrm{L}}$, as $Z_{\mathrm{G}} \neq Z_{\mathrm{L}}$ will be compensated due to reciprocity calibration. Then, due to the symmetry between "1" and "2" in (2.10) and as $\boldsymbol{Z}_{21} = \boldsymbol{Z}_{12}^T$ (see (2.2)), the noiseless relation between generator and load voltage, $\boldsymbol{D}$, is reciprocal, i.e.,

$$\boldsymbol{D}_{\mathrm{UL}}^T = \boldsymbol{D} = Z_{\mathrm{L}}(\boldsymbol{Z}_{22} + Z_{\mathrm{L}}\boldsymbol{I})^{-1}\boldsymbol{Z}_{21}(\boldsymbol{Z}_{11} + Z_{\mathrm{G}}\boldsymbol{I})^{-1}. \tag{3.1}$$

However, there is no such symmetry in (2.23), but

$$\boldsymbol{H} = \sigma_\vartheta \boldsymbol{R}_\eta^{-1/2}\boldsymbol{D}\boldsymbol{B}^{-H/2} = \sigma_\vartheta \boldsymbol{Q}^{-1/2}\boldsymbol{Z}_{21}\,\mathrm{Re}(\boldsymbol{Z}_{11})^{-1/2} \tag{3.2}$$

and

$$\boldsymbol{H}_{\mathrm{UL}} = \sigma_{\vartheta,\mathrm{UL}} \boldsymbol{R}_{\eta,\mathrm{UL}}^{-1/2}\boldsymbol{D}_{\mathrm{UL}}\boldsymbol{B}_{\mathrm{UL}}^{-H/2} = \sigma_{\vartheta,\mathrm{UL}} \boldsymbol{Q}_{\mathrm{UL}}^{-1/2}\boldsymbol{Z}_{12}\,\mathrm{Re}(\boldsymbol{Z}_{22})^{-1/2} \tag{3.3}$$

hold, so the information-theoretic downlink and uplink channels are not reciprocal in the ordinary way, i.e., $\boldsymbol{H}_{\mathrm{UL}}^T \neq \boldsymbol{H}$. Although $\boldsymbol{D}$ is reciprocal, in general, a different reciprocity relation is introduced by whitening the noise coupling between the antennas and by maintaining the physical consistency of the transmit power, see (2.19) and (2.20). This physically consistent reciprocity relation

$$\boldsymbol{H} = \frac{\sigma_\vartheta}{\sigma_{\vartheta,\mathrm{UL}}} \boldsymbol{R}_\eta^{-1/2}\boldsymbol{B}_{\mathrm{UL}}^{*/2}\boldsymbol{H}_{\mathrm{UL}}^T\boldsymbol{R}_{\eta,\mathrm{UL}}^{T/2}\boldsymbol{B}^{-H/2} \tag{3.4}$$

is obtained by comparing (3.2) and (3.3). If the base station wants to reuse the CSI estimated in the uplink for the downlink, it needs to use this physically consistent reciprocity relation for the information-theoretic channel.

Consider that the base station acquires CSI in the uplink by estimating $\boldsymbol{D}_{\mathrm{UL}}$ – instead of $\boldsymbol{H}_{\mathrm{UL}}$ – from the mobile(s)' pilot symbols. To make the downlink physically consistent at the base station, i.e., to apply (2.19), it needs to know $\boldsymbol{B}^{-H/2}$ anyway, so that it can compute $\boldsymbol{D}_{\mathrm{UL}}^T\boldsymbol{B}^{-H/2}$ without any further information, although compared to (3.2), there remains the unknown factor $\sigma_\vartheta \boldsymbol{R}_\eta^{-1/2}$.

Let us simplify the model for the MU-MISO downlink and uplink, i.e., when each mobile has a single antenna. We assume that the distance between different mobiles is large with respect to the wavelength. For large distances, the coupling reduces inversely with the distance [9], so it goes to zero and $\boldsymbol{Z}_{22}$ becomes diagonal. Furthermore, we assume identical antenna impedances Z_{A} at the mobiles, i.e.,

$$\boldsymbol{Z}_{22} = Z_{\mathrm{A}}\boldsymbol{I}. \tag{3.5}$$

Then the downlink information-theoretic channel simplifies to

$$\boldsymbol{R}_\eta = \sigma_\eta^2\boldsymbol{I}, \quad \sigma_\eta^2 = \frac{|Z_{\mathrm{L}}|^2}{R_{\mathrm{L}}|Z_{\mathrm{A}}+Z_{\mathrm{L}}|^2}\sigma_q^2, \quad \boldsymbol{Q} = \sigma_q^2\boldsymbol{I}, \quad \boldsymbol{H} = \boldsymbol{D}_{\mathrm{UL}}^T\boldsymbol{B}^{-H/2}, \tag{3.6}$$

i.e., due to (2.25), there is no unknown factor $\sigma_\vartheta \boldsymbol{R}_\eta^{-1/2}$ in this scenario. The uplink information-theoretic channel simplifies to

$$\boldsymbol{H}_{\mathrm{UL}} = \sigma_{\vartheta,\mathrm{UL}}\boldsymbol{R}_{\eta,\mathrm{UL}}^{-1/2}\boldsymbol{D}_{\mathrm{UL}}\frac{Z_{\mathrm{A}}+Z_{\mathrm{G}}}{\sqrt{R_{\mathrm{G}}\,\mathrm{Re}(Z_{\mathrm{A}})}}. \tag{3.7}$$

Also in this case, $\boldsymbol{H}$ and $\boldsymbol{H}_{\mathrm{UL}}$ are not reciprocal in the ordinary way.

Note that if the mobiles have more than one antenna, i.e., in MU-MIMO systems, $\boldsymbol{Z}_{22}, \boldsymbol{Q}, \boldsymbol{R}_\eta$ and $\boldsymbol{B}_{\mathrm{UL}}$ are block diagonal, since we assume that there is no coupling between different mobiles. The noise covariance of multi-antenna mobiles is also a matrix instead of a scalar. Therefore, even if (2.25) is taken into account, $\boldsymbol{D}_{\mathrm{UL}}^T\boldsymbol{B}^{-H/2} \neq \boldsymbol{H}$ in general. One solution in practice might be to create a database of noise covariance matrices corresponding to different models of mobiles for the base station. As in conventionally modeled systems, the base station needs feedback from the mobiles about their SNR and needs to deal with $\boldsymbol{R}_\eta$, which is not known perfectly.

3.3 Capacities and Rates not Taking the Physical Reciprocity or the Mutual Coupling into Account

In this section, we will compute the ergodic (sum) capacity in the downlink C_{erg} and the ergodic (sum) rates when using the ordinary reciprocity relation, instead of the physically consistent one ($R_{\mathrm{erg,recip}}$) and when the base station ignores the coupling at the base station and at the mobiles ($R_{\mathrm{erg,hyp}}$). In particular, we compute the (sum) capacity and rate for a given channel and the ergodic ones are obtained by taking the expectation w.r.t. the channel, i.e., for the (sum) capacity

$$C_{\mathrm{erg}}(P) = \mathrm{E}_{\boldsymbol{H}}[C(P)], \tag{3.8}$$

and in a similar way for the (sum) rates. An overview of the different transmit strategies is given in Table 3.1. We assume that the base station obtains an error-free estimate of $\boldsymbol{D}_{\mathrm{UL}}$ via pilot symbols and that $\boldsymbol{x} \sim \mathcal{N}_{\mathbb{C}}(\boldsymbol{0}\sqrt{\mathrm{W}}, \boldsymbol{R}_x)$ with some covariance matrix $\boldsymbol{R}_x$.

Table 3.1. Overview of the Transmit Strategies [21]. (©IEEE 2020)

	"cap"	"recip"	"hyp"
Rates	C, R_{lin}	$R_{\text{recip}}, R_{\text{recip,lin}}$	$R_{\text{hyp}}, R_{\text{hyp,lin}}$
Motivation	Capacity achieving strategy.	Naive use of the Multiport Communication Theory.	Conventionally modeled systems.
Description	The base station uses the information-theoretic model (2.18), as it leads to an easy to use channel model [9], **and uses the physically consistent reciprocity relation** (3.4)**.**	The base station uses the information-theoretic model (2.18), as it leads to an easy to use channel model [9], **but assumes that the ordinary reciprocity relation holds.**	The base station uses the information-theoretic model ignoring the mutual coupling (see (3.15), (3.20), (3.22) and (3.30)) and the ordinary reciprocity relation.
Procedure	1: Estimate $\boldsymbol{D}_{\text{UL}}$. 2: Compute $\boldsymbol{H}$ using (3.3) and (3.4) (or (3.6)). 3: Apply the optimal transmit strategy based on $\boldsymbol{H}$ and $P = P_{\text{T}}$.	1: Estimate $\boldsymbol{D}_{\text{UL}}$. 2: Compute $\boldsymbol{H}_{\text{UL}}$ using (3.3). 3: Apply the optimal transmit strategy based on $\boldsymbol{H}_{\text{UL}}^{T}$ (corresponding to $\boldsymbol{h}_{\text{UL}}^{*}$ for SU-MISO) and $P = P_{\text{T}}$.	1: Estimate $\boldsymbol{D}_{\text{UL}}$. 2: Compute $\hat{\boldsymbol{H}}$ using (3.1) and (3.22). 3: Apply the optimal transmit strategy based on $\hat{\boldsymbol{H}}'$ (see (3.32)) and $P = P_{\text{T,p}}$.
Channel that is transmitted over in the downlink	$\boldsymbol{H}$	$\boldsymbol{H}$	$\hat{\boldsymbol{H}}$

3.3.1 SU-MISO

For a single user, the channel matrices become vectors. Let

$$\boldsymbol{h} = \boldsymbol{H}^T, \quad \boldsymbol{h}_{\mathrm{UL}} = \boldsymbol{H}_{\mathrm{UL}}, \quad \boldsymbol{d}_{\mathrm{UL}} = \boldsymbol{D}_{\mathrm{UL}}. \tag{3.9}$$

The capacity of the downlink with power P is

$$C(P) = \log_2\left(1 + \frac{P}{\sigma_\vartheta^2}\|\boldsymbol{h}\|_2^2\right) \text{ for } P_{\mathrm{T}} = P. \tag{3.10}$$

Let

$$\boldsymbol{x} = \boldsymbol{f}s, \quad s \sim \mathcal{N}_{\mathbb{C}}(0\sqrt{\mathrm{W}}, P). \tag{3.11}$$

Capacity can be achieved by applying the linear precoder

$$\boldsymbol{f} = \frac{\boldsymbol{h}^*}{\|\boldsymbol{h}\|_2}. \tag{3.12}$$

As $\boldsymbol{f}$ can be computed from $\boldsymbol{h}$, which in turn is computed from $\boldsymbol{d}_{\mathrm{UL}}$ via (3.6), estimating $\boldsymbol{d}_{\mathrm{UL}}$ in the uplink and using the physically consistent reciprocity relation (3.4) achieves capacity.

Now consider what happens if the base station uses the information-theoretic model in the up- and downlink, but assumes that the ordinary reciprocity relation $\boldsymbol{H} = \boldsymbol{H}_{\mathrm{UL}}^T$ holds, corresponding to $\boldsymbol{h} = \boldsymbol{h}_{\mathrm{UL}}$ for SU-MISO. This means it determines the information-theoretic uplink channel $\boldsymbol{h}_{\mathrm{UL}}$ via (3.3), and then chooses the optimal precoder based on $\boldsymbol{h}_{\mathrm{UL}}^*$,

$$\boldsymbol{f}_{\mathrm{recip}} = \frac{\boldsymbol{h}_{\mathrm{UL}}^*}{\|\boldsymbol{h}_{\mathrm{UL}}\|_2} \tag{3.13}$$

leading to the rate

$$R_{\mathrm{recip}}(P) = \log_2\left(1 + \frac{P}{\sigma_\vartheta^2}\frac{|\boldsymbol{h}^H\boldsymbol{h}_{\mathrm{UL}}^*|^2}{\|\boldsymbol{h}_{\mathrm{UL}}\|_2^2}\right) \text{ for } P_{\mathrm{T}} = P. \tag{3.14}$$

Note that this rate is different from (3.10) and there will be some rate loss compared to capacity.

For comparison, let us also consider what happens if the base station ignores the coupling. This means that it does not use Multiport Communication Theory, but rather conventional modeling. To predict how much power the base station radiates, it needs to know the power-coupling matrix $\hat{\boldsymbol{B}}$ that ignores the mutual coupling and uses the mapping

$$\hat{\boldsymbol{x}} = \frac{1}{\sqrt{R_{\mathrm{G}}}}\hat{\boldsymbol{B}}^{H/2}\boldsymbol{u}_{\mathrm{G}}. \tag{3.15}$$

$\hat{\boldsymbol{B}}$ is diagonal and its diagonal entries can be obtained by connecting a linear generator to only one antenna in the array at a time, terminating the other antennas with open circuits and measuring the power $P_{\mathrm{T,p},n}$ flowing into the antenna. This means that when the nth antenna is excited with the voltage $u_{\mathrm{G},n}$ corresponding to some $\hat{x}_n$, $i_{1,n'} = 0\,\mathrm{A}\ \forall n' \neq n$ and the relevant part of the circuit reduces to a simple voltage divider (Fig. 3.1). The base station predicts that it radiates

$$P_{\mathrm{T,p},n} = |u_{\mathrm{G},n}|^2 \frac{\mathrm{Re}\left([\boldsymbol{Z}_{11}]_{n,n}\right)}{|[\boldsymbol{Z}_{11}]_{n,n} + Z_{\mathrm{G}}|^2}. \tag{3.16}$$

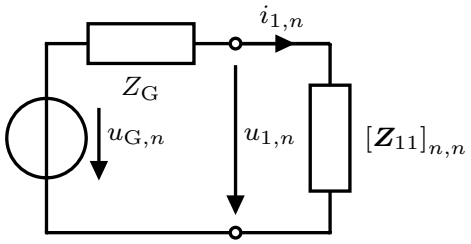

Fig. 3.1. Simplified circuit for measuring $P_{\mathrm{T},n}$ [21]. (©IEEE 2020)

Similar to (2.17), we also have

$$P_{\mathrm{T,p},n} = |u_{\mathrm{G},n}|^2 \frac{\left[\hat{\boldsymbol{B}}\right]_{n,n}}{R_{\mathrm{G}}}. \tag{3.17}$$

Thus analogously to (2.16), $\hat{\boldsymbol{B}}$ is given by

$$\hat{\boldsymbol{B}} = R_{\mathrm{G}}(\mathrm{diag}(\boldsymbol{Z}_{11}) + Z_{\mathrm{G}}\boldsymbol{I})^{-H} \,\mathrm{Re}(\mathrm{diag}(\boldsymbol{Z}_{11}))(\mathrm{diag}(\boldsymbol{Z}_{11}) + Z_{\mathrm{G}}\boldsymbol{I})^{-1} \tag{3.18}$$

and

$$\hat{\boldsymbol{B}}^{1/2} = \sqrt{R_{\mathrm{G}}}(\mathrm{diag}(\boldsymbol{Z}_{11}) + Z_{\mathrm{G}}\boldsymbol{I})^{-H} \,\mathrm{Re}(\mathrm{diag}(\boldsymbol{Z}_{11}))^{1/2}. \tag{3.19}$$

If the impedance of all base station antennas is the same, i.e., $\mathrm{diag}(\boldsymbol{Z}_{11})$ is a scaled identity matrix, then $\hat{\boldsymbol{B}}$ is also a scaled identity matrix. For an arbitrary excitation of the antenna array, the base station predicts the radiated power as

$$P_{\mathrm{T,p}} = \mathrm{E}\left[\|\hat{\boldsymbol{x}}\|_2^2\right] = \frac{\mathrm{E}\left[\boldsymbol{u}_{\mathrm{G}}^H \hat{\boldsymbol{B}} \boldsymbol{u}_{\mathrm{G}}\right]}{R_{\mathrm{G}}}. \tag{3.20}$$

As $\boldsymbol{x}$ is a zero-mean Gaussian random variable and as

$$\hat{\boldsymbol{x}} = \boldsymbol{B}^{-H/2} \hat{\boldsymbol{B}}^{H/2} \boldsymbol{x}, \tag{3.21}$$

$\hat{\boldsymbol{x}} \sim \mathcal{N}_{\mathbb{C}}(\boldsymbol{0}\sqrt{\mathrm{W}}, \boldsymbol{R}_{\hat{x}})$. Due to the mapping (3.15), the base station does not transmit over the information-theoretic channel $\boldsymbol{H}$, but over another information-theoretic channel $\hat{\boldsymbol{H}}$, the one ignoring the coupling, as given by

$$\hat{\boldsymbol{H}} = \sigma_\vartheta \boldsymbol{R}_\eta^{-1/2} \boldsymbol{D} \hat{\boldsymbol{B}}^{-H/2}. \tag{3.22}$$

For SU-MISO, let $\boldsymbol{d} = \boldsymbol{D}^T$ so that we can define the column vector

$$\hat{\boldsymbol{h}}^T = \hat{\boldsymbol{H}} \overset{(2.25)}{=} \boldsymbol{d}^T \hat{\boldsymbol{B}}^{-H/2}. \tag{3.23}$$

When the base station uses a precoder similar to (3.12),

$$\boldsymbol{f}_{\mathrm{hyp}} = \frac{\hat{\boldsymbol{h}}^*}{\|\hat{\boldsymbol{h}}\|_2}, \tag{3.24}$$

it can achieve the (hypothetical) rate

$$R_{\mathrm{hyp}}(P) = \log_2\left(1 + \frac{P}{\sigma_\vartheta^2}\|\hat{\boldsymbol{h}}\|_2^2\right) \text{ for } P_{\mathrm{T,p}} = P. \tag{3.25}$$

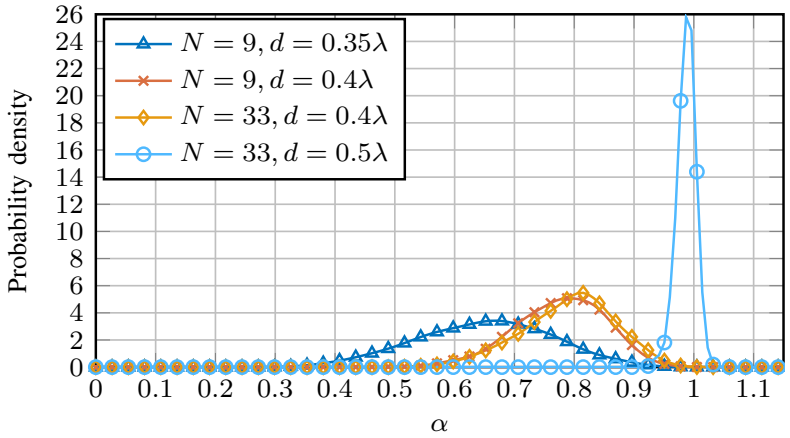

Fig. 3.2. Probability density of α for a uniform circular array (UCA) for four scenarios in a SU-MISO i.i.d. channel [21]. (©IEEE 2020)

We call the rate hypothetical because it is what the base station assumes to achieve. However when base station predicts that it radiates the power $P_{\mathrm{T,p}} = P$ and uses $\boldsymbol{f}_{\mathrm{hyp}}$, its (true) radiated power $P_{\mathrm{T}} \neq P$ in general. Consider the ratio α that follows from (2.17), (3.20), (3.21) and (3.24),

$$\alpha = \frac{P_{\mathrm{T}}}{P_{\mathrm{T,p}}} = \frac{\hat{\boldsymbol{h}}^*}{\|\hat{\boldsymbol{h}}\|_2} \hat{\boldsymbol{B}}^{-1/2} \boldsymbol{B} \hat{\boldsymbol{B}}^{-H/2} \frac{\hat{\boldsymbol{h}}^T}{\|\hat{\boldsymbol{h}}\|_2}. \tag{3.26}$$

α is a function of the channel and for some of its realizations,

$$\alpha < 1 \Leftrightarrow P_{\mathrm{T,p}} > P_{\mathrm{T}} \quad \text{or} \quad \alpha > 1 \Leftrightarrow P_{\mathrm{T,p}} < P_{\mathrm{T}}, \tag{3.27}$$

see Figs. 3.2 and 3.16, but $P_{\mathrm{T,p}} < P_{\mathrm{T}}$ is extremely rare for $d = 0.35\lambda$ and $d = 0.4\lambda$, but less so for $d = 0.5\lambda$. Therefore, depending on the channel realization, there will be rate curves that actually require more or less transmit power than predicted. On the one hand, if $\alpha > 1$ and if $P_{\mathrm{T,p}}$ is as large as the power available linearly from the power amplifiers, there will be non-linear distortions due to $P_{\mathrm{T}} > P_{\mathrm{T,p}}$, which may cause transmission failure. On the other hand, if $\alpha < 1$, i.e., $P_{\mathrm{T}} < P_{\mathrm{T,p}}$, the transmission will be successful but the power budget is not fully utilized.

The probability densities in this paper are estimated on a grid of 128 points in a Monte Carlo simulation (see Sections 3.4 and 3.5) using the MATLAB implementation [53] based on the theory in [54] with a Gaussian kernel. Note that α does not need to be estimated in the communication system; it is only introduced to explain the simulation results.

3.3.2 SU-MIMO

For SU-MIMO, the capacity in the downlink with power P is given by [55]

$$C(P) = \log_2 \left| \boldsymbol{I} + \sigma_\vartheta^{-2} \boldsymbol{H}^H \boldsymbol{H} \boldsymbol{R}_x \right| \text{ for } P_{\mathrm{T}} = P, \quad \boldsymbol{R}_x = \boldsymbol{V} \boldsymbol{\Psi} \boldsymbol{V}^H, \quad \mathrm{tr}(\boldsymbol{\Psi}) = P, \tag{3.28}$$

where $\boldsymbol{V}$ is obtained from the eigenvalue decomposition (EVD)

$$\boldsymbol{H}^H \boldsymbol{H} = \boldsymbol{V} \boldsymbol{\Phi} \boldsymbol{V}^H \tag{3.29}$$

and $\boldsymbol{\Psi}$ is a diagonal matrix whose entries are determined via waterfilling. This can be achieved by transmitting $\boldsymbol{s} \sim \mathcal{N}_{\mathbb{C}}(\boldsymbol{0}\sqrt{\mathrm{W}}, \boldsymbol{\Psi})$ over the precoder $\boldsymbol{V}$, i.e., $\boldsymbol{x} = \boldsymbol{V}\boldsymbol{s}$.

If the base station ignores the mutual coupling at the base station and at the mobiles, it uses (3.15) to transform from $\hat{\boldsymbol{x}}$ to $\boldsymbol{u}_{\mathrm{G}}$ as in SU-MISO, assumes that mobile uses the mapping

$$\hat{\boldsymbol{y}} = \frac{\sigma_\vartheta}{\sqrt{R_{\mathrm{L}}}} \hat{\boldsymbol{R}}_\eta^{-1/2} \boldsymbol{u}_{\mathrm{L}}, \quad \hat{\boldsymbol{R}}_\eta = \operatorname{diag}(\boldsymbol{R}_\eta) \tag{3.30}$$

instead of (2.20), and assumes that

$$\hat{\boldsymbol{\vartheta}} \sim \mathcal{N}_{\mathbb{C}}(\mathbf{0}\sqrt{\mathrm{W}}, \sigma_\vartheta^2 \boldsymbol{I}) \tag{3.31}$$

holds. Similar to (3.28), the optimal transmit strategy is to choose the precoder $\hat{\boldsymbol{V}}'$ from the singular value decomposition (SVD) of the channel

$$\hat{\boldsymbol{H}}' = \sigma_\vartheta \hat{\boldsymbol{R}}_\eta^{-1/2} \boldsymbol{D} \hat{\boldsymbol{B}}^{-H/2} = \hat{\boldsymbol{U}}' \hat{\boldsymbol{\Phi}}'^{,1/2} \hat{\boldsymbol{V}}'^{,H} \tag{3.32}$$

and the corresponding diagonal power allocation matrix $\hat{\boldsymbol{\Psi}}'$ obtained by waterfilling.

However, the noise distribution at the mobile in the information-theoretic model is

$$\hat{\boldsymbol{\vartheta}} \sim \mathcal{N}_{\mathbb{C}}\Big(\mathbf{0}\sqrt{\mathrm{W}}, \hat{\boldsymbol{R}}_\vartheta\Big), \quad \hat{\boldsymbol{R}}_\vartheta = \sigma_\vartheta^2 \hat{\boldsymbol{R}}_\eta^{-1/2} \boldsymbol{R}_\eta \hat{\boldsymbol{R}}_\eta^{-H/2}, \tag{3.33}$$

contrary to what the base station expects, see (3.31). Only $\operatorname{diag}\left(\hat{\boldsymbol{R}}_\vartheta\right) = \sigma_\vartheta^2 \boldsymbol{I}$ holds. This leads to the (hypothetical) rate

$$R_{\mathrm{hyp}}(P) = \log_2\Big|\boldsymbol{I} + \sigma_\vartheta^{-2} \hat{\boldsymbol{H}}^H \hat{\boldsymbol{H}} \boldsymbol{R}_{\hat{x}}\Big| \text{ for } P_{\mathrm{T,p}} = P, \quad \boldsymbol{R}_{\hat{x}} = \hat{\boldsymbol{V}}' \hat{\boldsymbol{\Psi}}' \hat{\boldsymbol{V}}'^{,H}, \quad \operatorname{tr}(\hat{\boldsymbol{\Psi}}') = P. \tag{3.34}$$

Similar to (3.25), this is only a hypothetical rate, since the true radiated power may be different from the predicted one. By generalization of (3.26), we consider the ratio

$$\begin{aligned} \alpha(P) &:= \frac{P_{\mathrm{T}}}{P_{\mathrm{T,p}}} = \frac{\operatorname{tr}\left(\hat{\boldsymbol{B}}^{-1/2} \boldsymbol{B} \hat{\boldsymbol{B}}^{-H/2} \boldsymbol{R}_{\hat{x}}\right)}{P} = \operatorname{tr}(\boldsymbol{A}(P)), \\ \boldsymbol{A}(P) &= \hat{\boldsymbol{B}}^{-1/2} \boldsymbol{B} \hat{\boldsymbol{B}}^{-H/2} \hat{\boldsymbol{V}}' \frac{\hat{\boldsymbol{\Psi}}}{P} \hat{\boldsymbol{V}}'^{,H}. \end{aligned} \tag{3.35}$$

Contrary to SU-MISO, for SU-MIMO α also depends on the power allocation.

When the base station uses the ordinary reciprocity relation instead of the physically consistent one, the optimal transmit strategy is to use the precoder $\boldsymbol{V}_{\mathrm{recip}}$ from the EVD

$$\boldsymbol{H}_{\mathrm{UL}}^* \boldsymbol{H}_{\mathrm{UL}}^T = \boldsymbol{V}_{\mathrm{recip}} \boldsymbol{\Phi}_{\mathrm{recip}} \boldsymbol{V}_{\mathrm{recip}}^H, \tag{3.36}$$

and $\boldsymbol{\Psi}_{\mathrm{recip}}$ determined via waterfilling. The rate of this scheme is

$$R_{\mathrm{recip}}(P) = \log_2\Big|\boldsymbol{I} + \sigma_\vartheta^{-2} \boldsymbol{R}_x \boldsymbol{H}^H \boldsymbol{H}\Big| \text{ for } P_{\mathrm{T}} = P, \quad \boldsymbol{R}_x = \boldsymbol{V}_{\mathrm{recip}} \boldsymbol{\Psi}_{\mathrm{recip}} \boldsymbol{V}_{\mathrm{recip}}^H, \quad \operatorname{tr}(\boldsymbol{\Psi}_{\mathrm{recip}}) = P. \tag{3.37}$$

3.3.3 MU-MISO and MU-MIMO

The sum capacity of the MU-MISO/MIMO Broadcast channel (BC) is given by [56, 57]

$$C(P) = \max_{\substack{\boldsymbol{\Xi} \succeq \mathbf{0}\,\mathrm{W} \\ \operatorname{tr}(\boldsymbol{\Xi}) \leq P}} \log_2\Big|\boldsymbol{I} + \sigma_\vartheta^{-2} \boldsymbol{H}^H \boldsymbol{\Xi} \boldsymbol{H}\Big| \text{ for } P_{\mathrm{T}} = P, \tag{3.38}$$

where $\boldsymbol{\Xi}$ is the (block-)diagonal covariance matrix in the dual Multiple Access Channel (MAC), i.e., it is based on the rate duality between the BC and the dual MAC with the channel $\boldsymbol{H}^H$. For MU-MIMO, we use the duality from [58], which ensures that streams allocated to the same mobile are orthogonal. Equation (3.38) describes a convex optimization problem that can be solved efficiently by various optimization algorithms, e.g., a projected gradient algorithm [59] with a step-size control as in [60, eq. (14)].

For MU-MISO, if the base station ignores the mutual coupling at the base station, it will perform an optimization as in (3.38), namely

$$R_{\mathrm{hyp}}(P) = \max_{\substack{\hat{\boldsymbol{\Xi}} \succeq \mathbf{0}\,\mathrm{W} \\ \mathrm{tr}(\hat{\boldsymbol{\Xi}}) \leq P}} \log_2 \left| \boldsymbol{I} + \sigma_\vartheta^{-2} \hat{\boldsymbol{H}}^H \hat{\boldsymbol{\Xi}} \hat{\boldsymbol{H}} \right| \text{ for } P_{\mathrm{T,p}} = P. \tag{3.39}$$

Note that this only holds as mutual coupling at the base station does not introduce interference, no matter whether taken into account or not – as long as the base station has got perfect channel knowledge.

For MU-MIMO, when the base station ignores the mutual coupling at the base station and at the mobiles, or when it uses the ordinary reciprocity relation in the information-theoretic model, the analysis is more involved, since the channel the base station expects and the true channel are different. This is similar to a channel estimation error and this leads to interference. The capacity achieving transmission scheme for perfect channel knowledge is Dirty Paper Coding (DPC). When this scheme is used with a channel estimation error, the achievable rate may even be lower than with linear precoding. This is shown for a lattice-based scheme in a two-user MU-MISO BC in [61].

When computing the achievable sum rate with linear precoding, a global optimization is required as this problem is non-convex, see e.g., [62, 63], which optimizes over the transmit covariance in the dual MAC globally. This is only feasible for a small number of users and their antennas. Instead, we use a linear zero forcing (ZF) approach for the comparison that is only guaranteed to find a local optimum. Among several algorithms in the literature [64, 65], we have chosen LISA [64], which is an elegant greedy weighted sum rate maximization algorithm with low complexity and very good performance. For the comparison we are considering, the choice of the weighted sum rate maximization algorithm is not substantial. LISA finds the ZF precoder and power allocation, where we use the variant that does not avoid the matrix inversion to optimize the receive filters. Applying it to $\boldsymbol{H}, \hat{\boldsymbol{H}}'$ and $\boldsymbol{H}_{\mathrm{UL}}^T$ for $P_{\mathrm{T}} = P, P_{\mathrm{T,p}} = P$ and $P_{\mathrm{T}} = P$ and transmitting over $\boldsymbol{H}, \hat{\boldsymbol{H}}$ and $\boldsymbol{H}$ respectively, leads to $R_{\mathrm{lin}}, R_{\mathrm{hyp,lin}}$ and $R_{\mathrm{recip,lin}}$. When computing the rates, we do not consider the equalizers at the mobiles, in other words, we assume that they employ an optimum equalization.

3.4 Simulations for the I.I.D. Channels

In the simulations, we assume a base station with a UCA of N parallel infinitely thin, but perfectly conducting $\lambda/2$-dipoles with antenna spacing d, and one or more mobiles with a UCA consisting also of parallel $\lambda/2$-dipoles. Their impedance matrices can be obtained according to Section 2.4. Let Z_{A} be the self-impedance of the $\lambda/2$-dipoles. We assume the heuristic match $Z_{\mathrm{G}} = Z_{\mathrm{L}} = \mathrm{Re}(Z_{\mathrm{A}})$, which matches the real part of the antenna impedance to the purely resistive source and load impedance. $\boldsymbol{Q}^{1/2}$ is obtained by the (lower triangular) Cholesky decomposition of $\boldsymbol{Q}$.

For the noise parameters, we use the measured ones from [66, Tables IV & VI] with a noise bandwidth of $740\,\mathrm{kHz}$, except that we assume $\mathrm{Re}(Z_{\mathrm{A}})$ as the input impedance of the LNA, so it fits our model. In this section we also assume that the entries of $\boldsymbol{Z}_{21}$ are i.i.d. according to $\mathcal{N}_{\mathbb{C}}(0\,\Omega, \sigma_z^2)$.

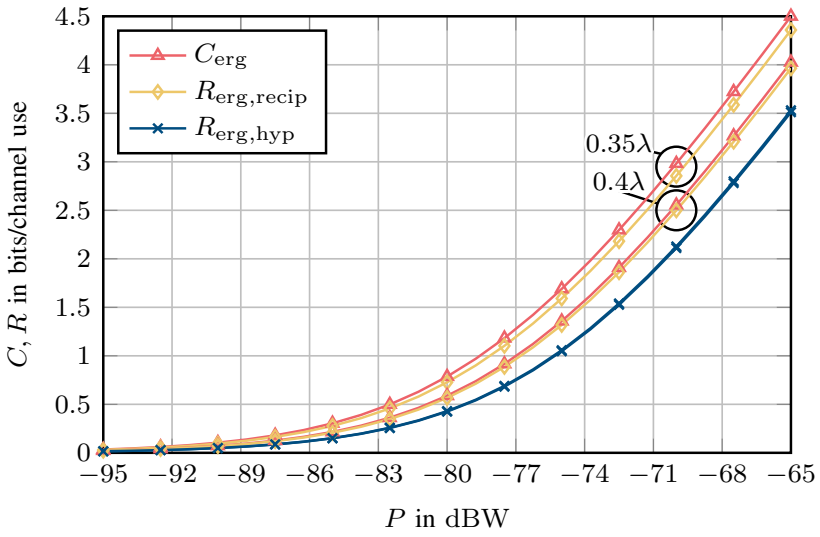

Fig. 3.3. Ergodic downlink rates for a UCA with 9 $\lambda/2$-dipoles, and 0.35λ and 0.4λ antenna spacing in a SU-MISO i.i.d. channel (based on [22]) [21]. (©IEEE 2020)

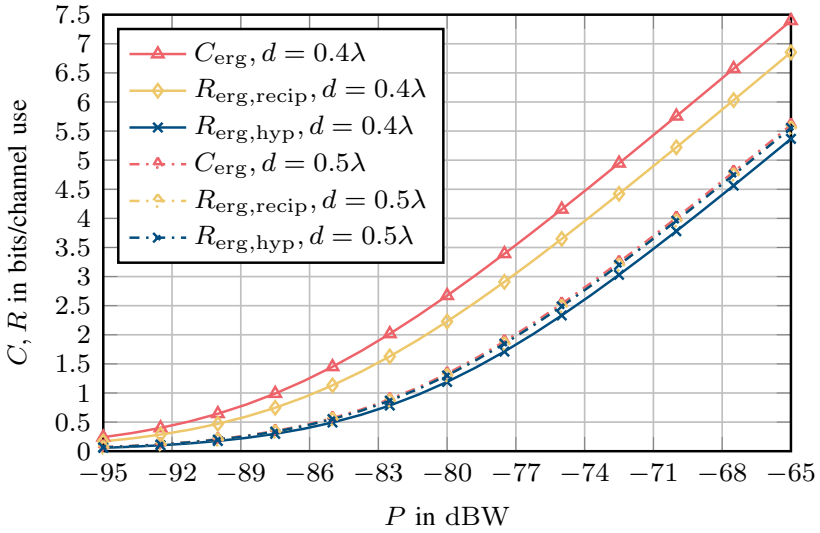

Fig. 3.4. Ergodic downlink rates for a UCA with 33 $\lambda/2$-dipoles, and 0.4λ and 0.5λ antenna spacing in a SU-MISO i.i.d. channel (based on [22]) [21]. (©IEEE 2020)

In order to obtain reasonable transmit powers, $\sigma_z \approx 0.019\,085\,\Omega$ is chosen, which corresponds to the absolute value of the mutual impedance between two $\lambda/2$-dipoles separated by 1000λ, which is about $85.7\,\text{m}$ at $3.5\,\text{GHz}$.

The ergodic (sum) capacity and rates, the average number of active streams and the empirical probability density of α were computed by a Monte Carlo simulation with 1000 channel realizations.

3.4.1 SU-MISO

Consider one single antenna receiver in four scenarios: a base station with $N = 9$ antennas and $d = 0.35\lambda$ or $d = 0.4\lambda$ antenna spacing and one with $N = 33$ and $d = 0.4\lambda$ or $d = 0.5\lambda$. Fig. 3.2 shows the probability density for α in these scenarios. The largest variation in α is obtained for a small antenna spacing of 0.35λ, where for some channel realizations only about $36.2\,\%$ of the

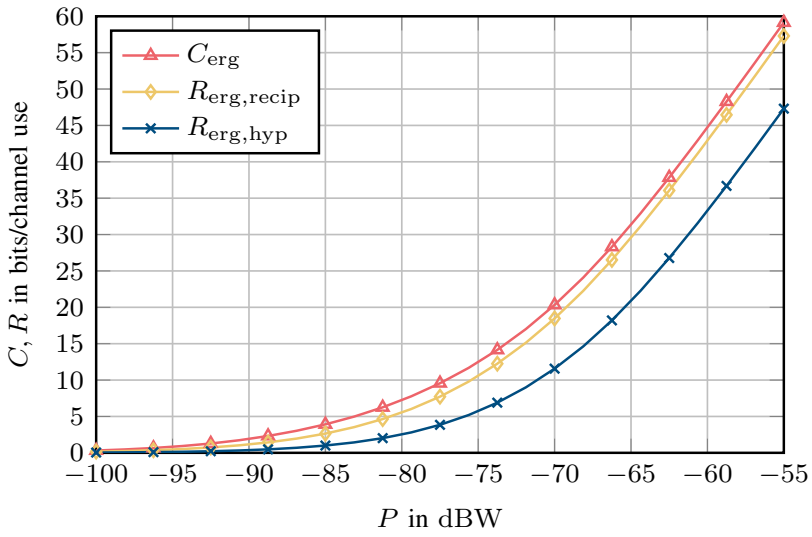

Fig. 3.5. Ergodic downlink rates for a UCA with 33 $\lambda/2$-dipoles at the base station and a mobile with a UCA with 9 $\lambda/2$-dipoles, both with 0.4λ antenna spacing, in a SU-MIMO i.i.d. channel [21]. (©IEEE 2020)

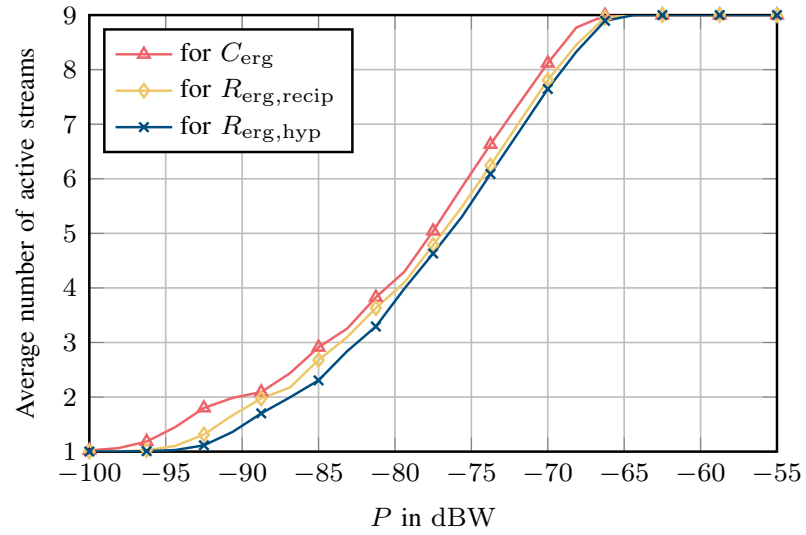

Fig. 3.6. Average number of active streams for a UCA with 33 $\lambda/2$-dipoles at the base station and a mobile with a UCA with 9 $\lambda/2$-dipoles, both with 0.4λ antenna spacing, in a SU-MIMO i.i.d. channel [21]. (©IEEE 2020)

predicted power is radiated and for some as much as $94.0\,\%$. The variations for 0.4λ antenna spacing are less pronounced, but there is still a considerable variation in α. For $d = 0.5\lambda$ there is even less variation. Furthermore, there is a trend that the larger d is, the further the mass of the distribution of α moves to larger values of α. We conclude that the base station radiates on average less power than predicted when it uses conventional modeling. The loss in power is significantly larger for $d = 0.35\lambda$ than for $d = 0.4\lambda$, and in turn than for $d = 0.5\lambda$.

Figs. 3.3 and 3.4 show the ergodic capacities and rates for these scenarios. Comparing them, we can see that for the same P, C_{erg} and $R_{\text{erg,recip}}$ are larger for $N = 33$ than for $N = 9$, and larger for smaller d than for larger d. Therefore, a smaller d is advantageous. $R_{\text{erg,hyp}}$ only changes very little from $d = 0.35\lambda$ to 0.4λ, and increases slightly from $d = 0.4\lambda$ to 0.5λ. We can also see that using the

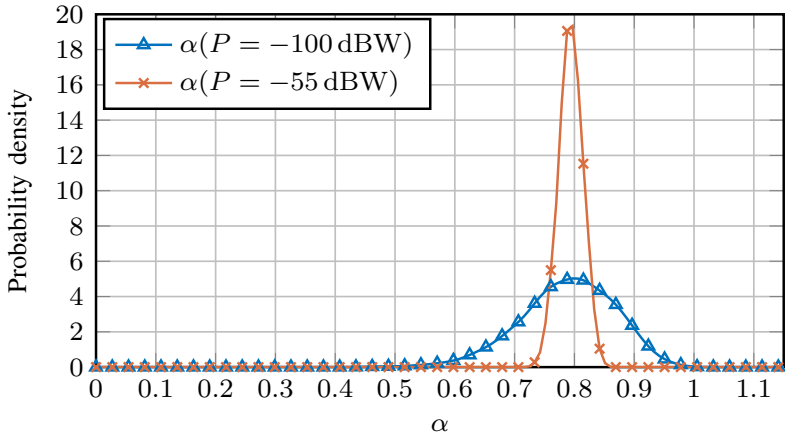

Fig. 3.7. Probability density of α for a UCA with 33 $\lambda/2$-dipoles at the base station and a mobile with a UCA with 9 $\lambda/2$-dipoles, both with 0.4λ antenna spacing, in a SU-MIMO i.i.d. channel [21]. (©IEEE 2020)

ordinary reciprocity relation in the information-theoretic model leads to a loss in rate that is small for larger antenna spacings and a small number of antennas, but increases considerably for smaller antenna spacings and a large number of antennas. This loss is caused by the precoder $\boldsymbol{f}_{\mathrm{recip}}$, leading to the beamforming vector $\sqrt{R_{\mathrm{G}}}\boldsymbol{B}^{-H/2}\boldsymbol{f}_{\mathrm{recip}}$. Both are optimal for the ordinary reciprocity relation, but not for the physically consistent one. Still, using the ordinary reciprocity relation is considerably better than using conventional modeling. $R_{\mathrm{erg,hyp}}$ shows the same tendency as $R_{\mathrm{erg,recip}}$, but the gap to C_{erg} is significantly larger than for $R_{\mathrm{erg,recip}}$. This gap is not only caused by a suboptimal precoder, but also by the base station not being able to accurately predict the radiated power P_{T} with conventional modeling. Note that mutual coupling is present independent of the antenna separation and does not decrease monotonically with increasing d, but rather follows a more complicated relation. It decreases monotonically approximately between $d = 0$ and $\lambda/2$, though. If we increase the number of base station antennas further, e.g., to $N = 65$, we see that the trends going from $N = 9$ to 33 continue.

3.4.2 SU-MIMO

Consider a base station with a UCA consisting of $N = 33$ $\lambda/2$-dipoles and a mobile with a UCA with $M = 9$ $\lambda/2$-dipoles, both with 0.4λ antenna spacing. Compared to SU-MISO (see Fig. 3.4), the difference between $R_{\mathrm{erg,hyp}}$ and C_{erg} is significantly larger, as shown in Fig. 3.5, although the antenna spacing at the base station is the same. As in SU-MISO, $R_{\mathrm{erg,recip}}$ achieves a better performance than $R_{\mathrm{erg,hyp}}$.

Looking at the average number of active streams (Fig. 3.6), all schemes perform similarly. This means the rate difference comes mainly from radiating a different amount of power than predicted and from the suboptimal precoders, instead of a suboptimal number of active streams.

Regarding the predicted radiated power $P_{\mathrm{T,p}}$ when ignoring the coupling, consider the probability density of α in Fig. 3.7. For $P = -100\,\mathrm{dBW}$, the average number of active streams is 1, and the distribution is similar to Fig. 3.2. However for $P = -55\,\mathrm{dBW}$, the average number of active streams is close to 9, and the distribution is much more narrow around $\alpha \approx 0.79$. This means that when more streams are active, there is an averaging effect between streams belonging to directions with large α and to those with small α. Note that the ratio of the predicted to the radiated power of the individual streams may still experience a distribution similar to when only one stream is active.

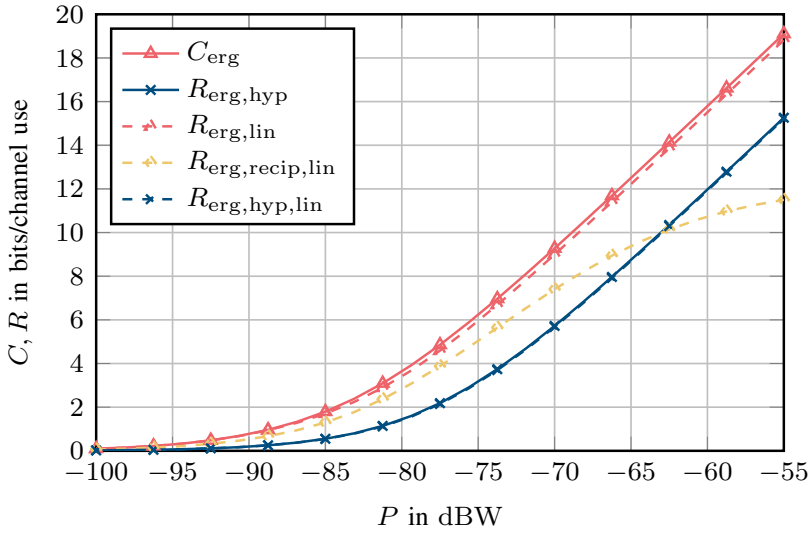

Fig. 3.8. Ergodic downlink sum rates for a UCA with 33 $\lambda/2$-dipoles with 0.4λ antenna spacing at the base station and two mobiles in a MU-MISO i.i.d. channel [21]. (©IEEE 2020)

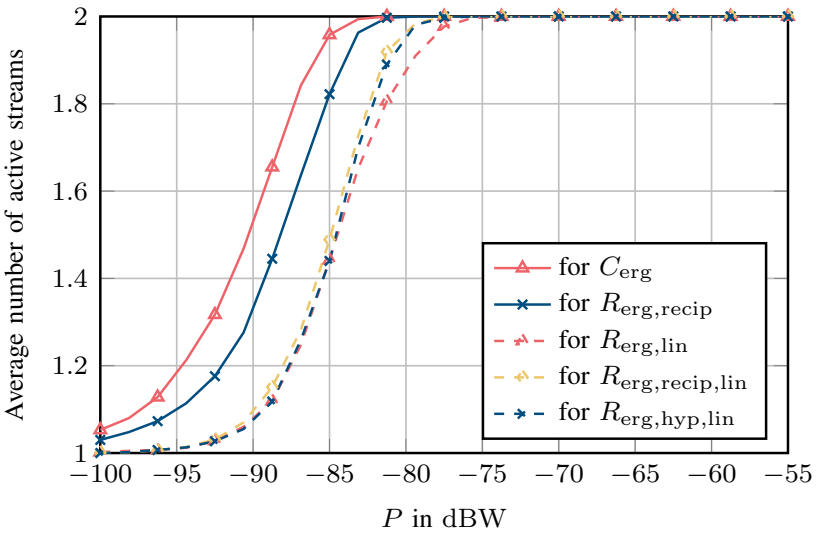

Fig. 3.9. Average number of active streams for a UCA with 33 $\lambda/2$-dipoles with 0.4λ antenna spacing at the base station and two mobiles in a MU-MISO i.i.d. channel [21]. (©IEEE 2020)

3.4.3 MU-MISO

Let us compare the ergodic sum rates in Fig. 3.8 for a base station with $N = 33$ $\lambda/2$-dipoles in a UCA communicating to two mobiles with one $\lambda/2$-dipole each. The performance of linear ZF precoding is very close to DPC for both, the sum capacity and the hypothetical sum rate, although fewer streams are active with linear precoding up to around $P = -75\,\mathrm{dBW}$, see Fig. 3.9. The loss when ignoring the coupling ($R_{\mathrm{erg,hyp}}$) is qualitatively similar to the loss for SU-MIMO in Fig. 3.5. For $R_{\mathrm{erg,recip,lin}}$, the loss is smaller than for $R_{\mathrm{erg,hyp,lin}}$ for small transmit powers – and as shown in Fig. 3.9, there is only a bit more than one stream active on average. This means that in this region, the system behaves similarly to a SU-MISO system and is mainly noise limited. For larger transmit powers, however, the loss starts to increase significantly when 2 streams are active on average, because using the ordinary reciprocity relation leads to wrong CSI in the downlink and causes

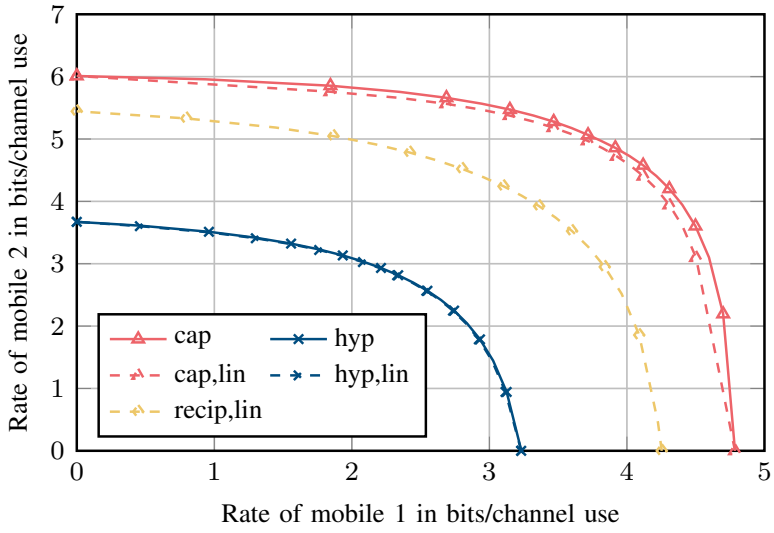

Fig. 3.10. Rate region for one channel realization for a UCA with 33 $\lambda/2$-dipoles with 0.4λ antenna spacing at the base station and two mobiles in a MU-MISO i.i.d. channel for $P = -70.57\,\mathrm{dBW}$ [21]. (©IEEE 2020)

interference. The larger this interference is compared to the noise power, the more important it is. For large interference, the system becomes interference limited and $R_{\mathrm{erg,recip,lin}}$ saturates. This is why starting from $P \approx -63\,\mathrm{dBW}$, $R_{\mathrm{erg,recip,lin}}$ is even worse than $R_{\mathrm{erg,hyp,lin}}$.

Consider also the rate region for one channel realization. The weighted sum and per-user rates for DPC can be obtained in a similar way to (3.38) and (3.39) using, e.g., a projected gradient algorithm [59], and for linear precoding using similarly the weighted sum rate maximization algorithm from [64]. When we have a look at the rate region for one channel realization in the same setting as for the sum rates, we can see a similar behavior as for the sum rate, see Fig. 3.10. The curves corresponding to the sum capacity and its corresponding sum rate with linear ZF precoding are called "cap" and "cap,lin" in the figure, and accordingly "hyp" and "hyp,lin" for the hypothetical sum rate and "recip,lin' for the one for the ordinary reciprocity relation. The performance using linear ZF precoding is very close to DPC.

3.4.4 MU-MIMO

For MU-MIMO, let us also consider a UCA with $N = 33$ antennas at the base station and two mobiles with a UCA of 9 antennas, all three with 0.4λ antenna spacing. For smaller transmit powers, the performance of linear ZF precoding is very close to DPC for the sum capacity and the hypothetical sum rate. But as the transmit power increases, the gap also increases, see Fig. 3.11. Similar to MU-MISO, for small P, $R_{\mathrm{erg,recip,lin}}$ performs well, around $P = -70\,\mathrm{dBW}$ the gap to $R_{\mathrm{erg,hyp,lin}}$ starts to decrease considerably, at $P \approx -61\,\mathrm{dBW}$ they intersect and for even larger P, $R_{\mathrm{erg,recip,lin}}$ starts to saturate. Compared to MU-MISO, the sum rate loss compared to C_{erg} increases for all ergodic rates, i.e., the loss increases with an increasing number of mobile antennas.

The average numbers of active streams in Fig. 3.12 show that for small transmit powers, they are very similar for DPC and linear ZF, but as the SNR increases, those for DPC increase much faster, i.e., the larger sum capacity and hypothetical rate in Fig. 3.11 can be explained by DPC supporting more active streams.

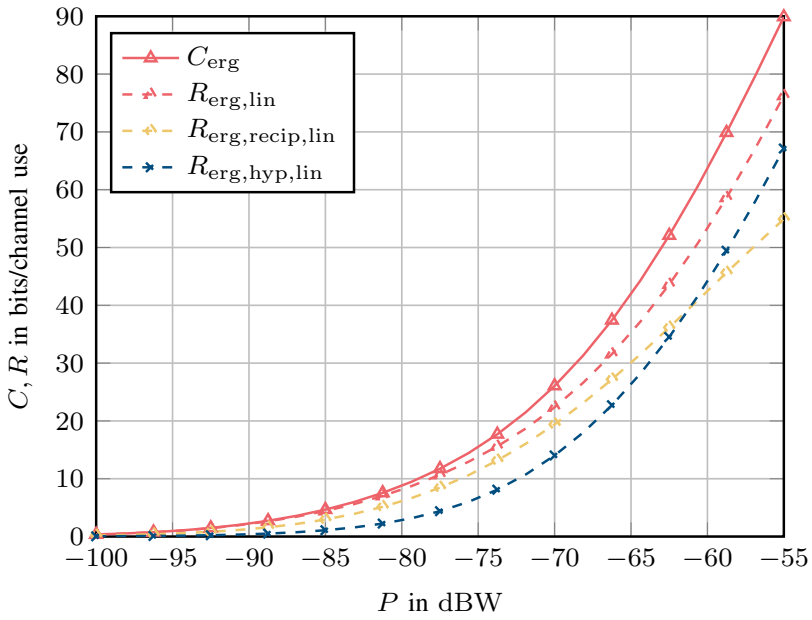

Fig. 3.11. Ergodic downlink sum rates for a UCA with 33 $\lambda/2$-dipoles at the base station and two users with a 9 $\lambda/2$-dipole UCA, all three with 0.4λ antenna spacing, in a MU-MIMO i.i.d. channel [21]. (©IEEE 2020)

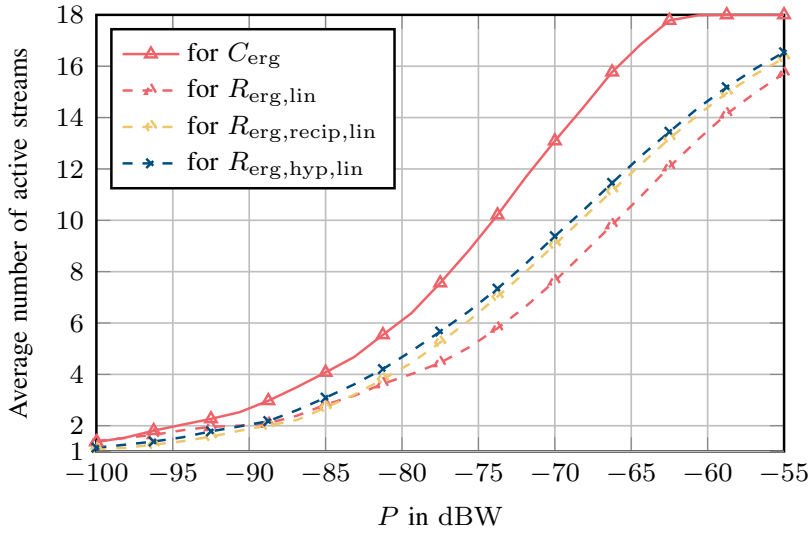

Fig. 3.12. Average number of active streams for a UCA with 33 $\lambda/2$-dipoles at the base station and two users with a 9 $\lambda/2$-dipole UCA, all three with 0.4λ antenna spacing, in a MU-MIMO i.i.d. channel [21]. (©IEEE 2020)

3.5 Simulations with the QuaDRiGa Channel Generator

QuaDRiGa [10, 11] is a channel generator written in MATLAB, which allows channels to be generated that are more realistic than i.i.d. channels. It is compatible with the current 3GPP channel model, 3GPP TS 38.901 [12], valid from $500\,\text{MHz}$ to $100\,\text{GHz}$. As in [52], we consider a single non-sectored base station site in the urban macrocell (UMa) model, but without mobility. The model assumes a hexagonal grid of cells with base station sites at certain corners of the hexagons. When the base station serves all mobiles closest to it, it serves a hexagon with edge length $(500/\sqrt{3})\,\text{m}$ and is located at its center, see Fig. 3.13. The $\lambda/2$-dipoles at the base station and at the mobiles

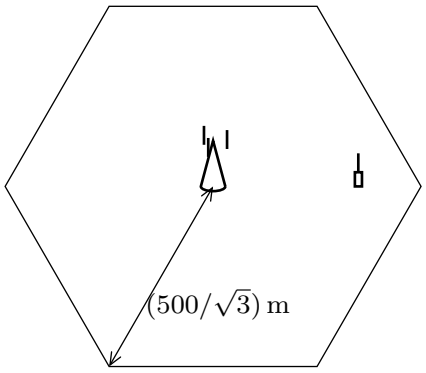

Fig. 3.13. A base station serving a mobile in a hexagonal cell [52].

are all oriented vertically, and the arrays are centered around the position of the respective base station or mobile. The mobiles are distributed uniformly in the hexagon outside of a circle with radius $35\,\mathrm{m}$ around the base station. The altitude of the base station is $25\,\mathrm{m}$ and that of the mobiles is determined according to [12]. The continuous time channels obtained by QuaDRiGa need to be scaled by $\mathrm{Re}(Z_\mathrm{A})$ so that they fit the circuit-theoretical model and the receive power matches. Let us denote the scaled continuous time channels as

$$\boldsymbol{Z}_{21}(t) = \sum_{n_\mathrm{path}=1}^{N_\mathrm{path}} \delta(t - t_{n_\mathrm{path}}) \boldsymbol{Z}_{21,n_\mathrm{path}}, \tag{3.40}$$

consisting of N_path paths described by a Delta distribution δ, with a delay t_{n_path} and coefficients $\boldsymbol{Z}_{21,n_\mathrm{path}}$. Additionally, they need to be filtered by a transmit and a receive filter and sampled, since the QuaDRiGa continuous time channels are impulse trains for each individual channel between a transmit and a receive antenna. We use root-raised cosine transmit and receive filters with $\Delta f = 15\,\mathrm{kHz}$ and roll-off factor 1 at the center frequency $3.5\,\mathrm{GHz}$, because it does not introduce any noise correlations in time-domain after sampling. The bandwidth is similar to an LTE subcarrier. Regarding the noise parameters, the same parameters as for the i.i.d. channels are used, but the noise (co-)variances are scaled by $15/740$, so they match the smaller bandwidth, maintaining the same noise power per bandwidth. We assume that we can approximate the system to be frequency flat at the center frequency $3.5\,\mathrm{GHz}$, as the relative bandwidth is only about $0.000\,43\,\%$. The channel in discrete time then is

$$\boldsymbol{Z}_{21}[l] = \frac{1}{\Delta f} \left(h_\mathrm{RC} * \boldsymbol{Z}_{21}\right)\left(\frac{l}{\Delta f}\right) = \frac{1}{\Delta f} \sum_{n_\mathrm{path}=1}^{N_\mathrm{path}} h_\mathrm{RC}\left(\frac{l}{\Delta f} - t_{n_\mathrm{path}}\right) \boldsymbol{Z}_{21,n_\mathrm{path}}, \quad l \in \mathbb{Z}, \tag{3.41}$$

where $h_\mathrm{RC}(t)$ is the impulse response of a raised cosine filter with symbol rate Δf and roll-off factor 1. Note that the factor $1/\Delta f$ is needed such that the units match when $\boldsymbol{Z}_{21}[l]$ is convolved with $\boldsymbol{u}_1[l]$, and to fulfill the Nyquist criterion when $\boldsymbol{Z}_{21}(t)$ is a unit impulse. We also assume $\boldsymbol{Z}_{21}[l]$ to be frequency flat, so it is sufficient to consider the channel at the base band frequency $\nu = 0\,\mathrm{Hz}$. To evaluate it there, we compute the discrete-time Fourier transform of $\boldsymbol{Z}_{21}[l]$, which can be simplified using the Poisson summation formula

$$\sum_{l=-\infty}^{\infty} h_\mathrm{RC}\left(\frac{l}{\Delta f} - t_{n_\mathrm{path}}\right) e^{-j2\pi\nu l/\Delta f} = \Delta f \sum_{k=-\infty}^{\infty} e^{-j2\pi(k\Delta f+\nu)t_{n_\mathrm{path}}} H_\mathrm{RC}(k\Delta f + \nu), \tag{3.42}$$

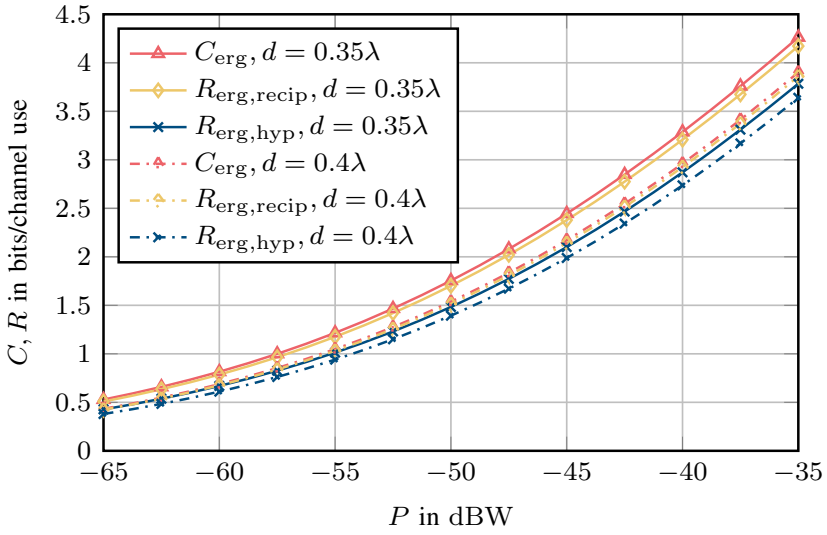

Fig. 3.14. Ergodic downlink rates for a UCA with 9 $\lambda/2$-dipoles, and 0.35λ and 0.4λ antenna spacing in a SU-MISO QuaDRiGa channel [21]. (©IEEE 2020)

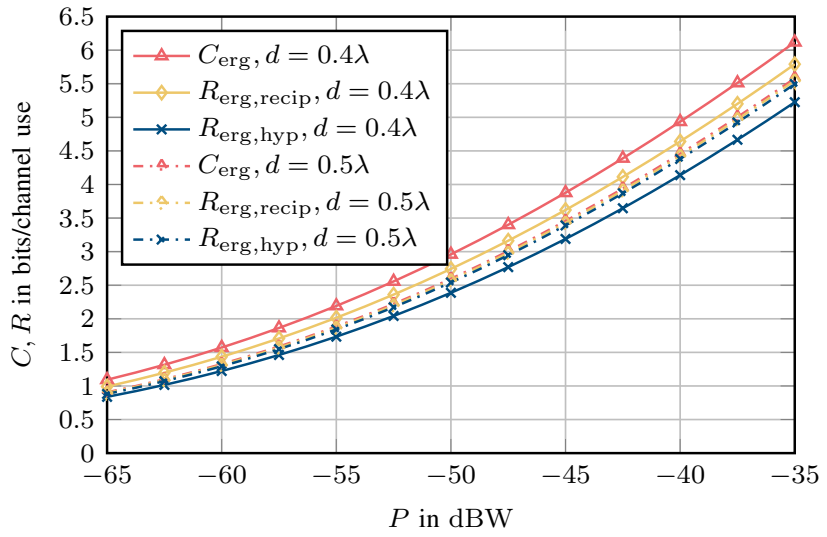

Fig. 3.15. Ergodic downlink rates for a UCA with 33 $\lambda/2$-dipoles and 0.4λ and 0.5λ antenna spacing in a SU-MISO QuaDRiGa channel [21]. (©IEEE 2020)

as inspired by [67], where $H_{\text{RC}}(f)$ is the Fourier transform of $h_{\text{RC}}(t)$. As the raised cosine pulse is sufficiently frequency-limited, for $\nu = 0\,\text{Hz}$ only the summand with $k = 0$ is non-zero, and the discrete-time Fourier transform evaluated at this ν is

$$\boldsymbol{Z}_{21} = \sum_{l=-\infty}^{\infty} \boldsymbol{Z}_{21}[l] e^{-j2\pi\nu l/\Delta f}|_{\nu=0\,\text{Hz}} = \sum_{n_{\text{path}}=1}^{N_{\text{path}}} H_{\text{RC}}\left(0\Delta f\right) \boldsymbol{Z}_{21,n_{\text{path}}} = \sum_{n_{\text{path}}=1}^{N_{\text{path}}} \boldsymbol{Z}_{21,n_{\text{path}}}. \tag{3.43}$$

Let us now compare the simulation results for the SU-MISO and MU-MIMO scenarios in the i.i.d. channel with those in the QuaDRiGa scenario. The attenuation of the channels generated by QuaDRiGa is larger than for the i.i.d. channel, so the ergodic (sum) rates are plotted for a larger P such that similar ergodic (sum) rates are achievable, see Figs. 3.14, 3.15 and 3.17. For SU-MISO in the range plotted, the slope of the ergodic rates is smaller than in the i.i.d. channel at a similar

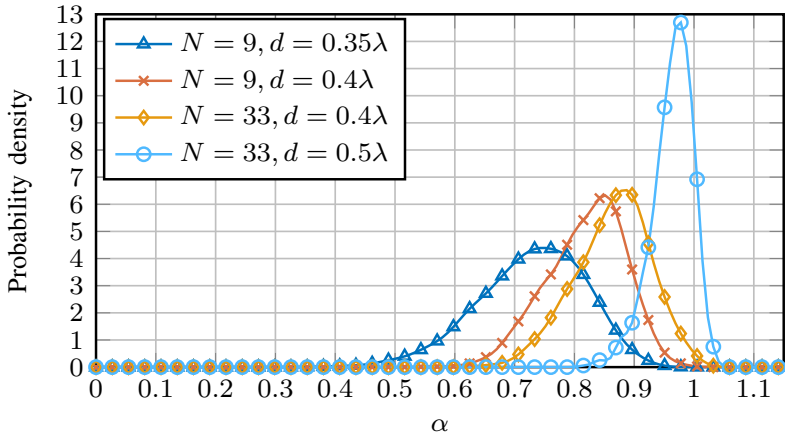

Fig. 3.16. Probability density of α for a UCA for four scenarios in a SU-MISO QuaDRiGa channel [21]. (©IEEE 2020)

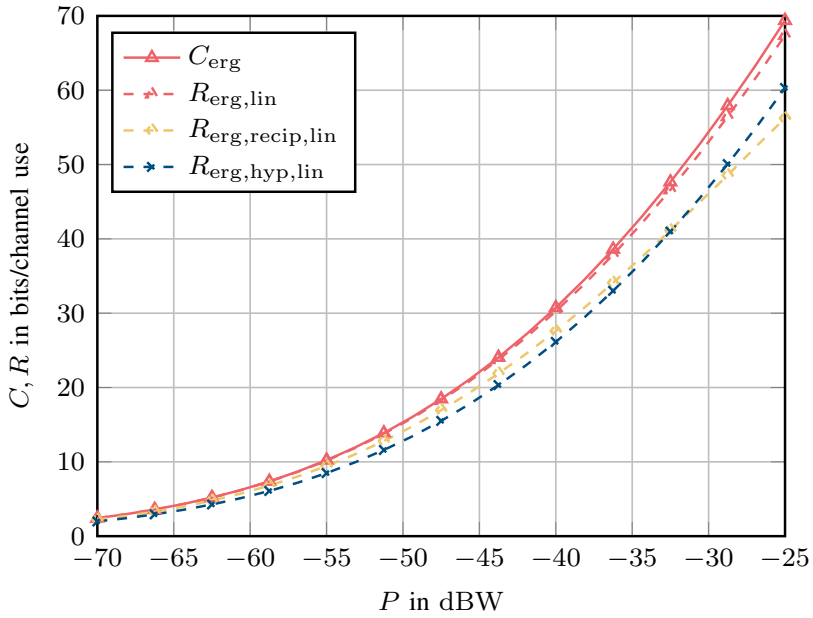

Fig. 3.17. Ergodic downlink sum rates for a UCA with 33 $\lambda/2$-dipoles at the base station and two users with a 9 $\lambda/2$-dipole UCA, all three with 0.4λ antenna spacing, in a MU-MIMO QuaDRiGa channel [21]. (©IEEE 2020)

ergodic rate. This means that for many channel realizations, the channel attenuation is large and the slope of $\log_2(1 + \text{SNR})$ is smaller than 1 in logarithmic scale. There is a similar rate loss if the base station uses the ordinary reciprocity relation as in the i.i.d. channel. Similarly, C_{erg} and $R_{\text{erg,recip}}$ are larger for $N = 33$ than for $N = 9$, and larger for smaller d than for larger d. Therefore, a smaller d is also advantageous and desirable here. Also similarly, on average less power is radiated than predicted if the base station uses conventional modeling. For $d = 0.35\lambda$ and 0.4λ, the loss due to this and due to the suboptimal beamforming is smaller for the channels generated by QuaDRiGa, but for $d = 0.5\lambda$, they are about the same. This smaller loss for $d = 0.35\lambda$ and 0.4λ corresponds to the distribution of α being shifted a bit closer to 1, see Fig. 3.16. Furthermore, the variation of α also gets slightly smaller for $d = 0.35\lambda$ and 0.4λ, but larger for $d = 0.5\lambda$. As in the i.i.d. channel, using the ordinary reciprocity relation leads to higher ergodic rates than conventional modeling.

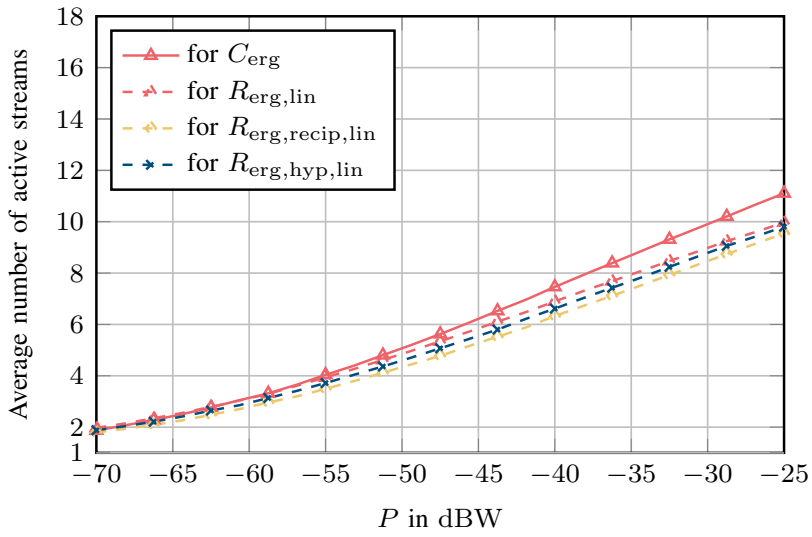

Fig. 3.18. Average number of active streams for a UCA with 33 $\lambda/2$-dipoles at the base station and two users with a 9 $\lambda/2$-dipole UCA, all three with 0.4λ antenna spacing, in a MU-MIMO QuaDRiGa channel [21]. (©IEEE 2020)

In the MU-MIMO scenario, the ergodic sum rates look similar as in the i.i.d. channels, see Figs. 3.11 and 3.17, but the losses due to using the ordinary reciprocity relation or ignoring the coupling are smaller and linear ZF is closer to DPC. Regarding the average number of active streams, see Figs. 3.12 and 3.18, fewer are active for the same sum rate in the QuaDRiGa channels than in the i.i.d. channels. This can be explained by the larger correlation of the QuaDRiGa per-user channels. Furthermore, the difference between the numbers of active streams for linear ZF and for DPC is smaller for the QuaDRiGa channels. As the linear ZF exploits cooperation between the antennas belonging to the same users using the SVD, the advantage of DPC is that it can remove inter-user interference. Due to the random placing of the users in the QuaDRiGa model, the channels to different users are almost orthogonal, so DPC is less beneficial than for the i.i.d. channel model.

3.6 Conclusion

We have analyzed the reciprocity of a MU-MIMO TDD system based on Multiport Communication Theory. We have seen that by incorporating the physical noise model and the power consistency, the ordinary (pseudo-physical) reciprocity relation between the information-theoretic up- and downlink channel does not hold in general – even if the noiseless relation between the transmit voltage sources and the receive load voltages is reciprocal. Instead, a physically consistent reciprocity relation holds. We have shown how the base station can achieve capacity using this relation when it computes the downlink channel from the uplink channel: namely, by using the power-coupling matrix it needs to know anyway to obtain the information-theoretic channel and by using a database of noise covariance matrices of the mobiles.

We have shown that when the base station uses the ordinary reciprocity relation, it will use suboptimal beamforming vectors and suboptimal power allocations that can significantly decrease the (sum) rate of the downlink, depending on the array geometry and on the type of antennas used. When the base station uses conventional modeling, i.e., if it ignores the coupling, there can also be a significant rate loss. Furthermore it cannot even predict the power it radiates accurately and the

radiated power can vary greatly. In multi-user systems, using the ordinary reciprocity relation is similar to having a channel estimation error, which leads to intra-cell interference between different users. The loss in achievable rate when ignoring mutual coupling is larger for a reduced antenna spacing, but capacity increases at the same time. Compactness is therefore advantageous for better performance.

These conclusions hold both for i.i.d. channels and for channels based on the 3GPP TS 38.901 UMa model generated by QuaDRiGa. This highlights the importance of taking the mutual coupling into account, and its effects on the reciprocity in the information-theoretic channel. It is sensible to take it into account by using two matrix multiplications with matrices that can be determined offline at the design stage.

Although our numerical results are based on canonical minimum scattering antennas to enable an analytic calculation of the impedance matrices of the arrays, the analysis is not limited to these types of antenna elements. For other antenna elements, the impedance matrices must be computed numerically with an appropriate electromagnetic solver or must be measured. Similarly, although we have only provided numerical results for i.i.d. channels and 3GPP TS 38.901 UMa channels, the approach presented is not limited to these types of channels.

4. On the Impact of the Mutual Impedance on Power and Achievable Rate

In this chapter, we consider the mutual reactance of hypothetical isotropic radiators and the influence of the mutual reactance on antenna arrays with zero mutual resistance. We compute the mutual reactance of hypothetical isotropic radiators using passivity, which has not been considered in wireless communications literature. We show that when an antenna array with zero mutual resistance is excited by ideal current sources, the mutual reactance does not have any influence on the radiated power. However, practical radio frequency amplifiers are not ideal current sources, but can often be modeled as linear sources. Then the radiated power depends on the mutual reactance. Furthermore in receive mode, the mutual reactance introduces noise correlations between the antennas. Numerical results show the impact of neglecting the mutual reactance on the radiated power and on the ergodic up- and downlink rates in an i.i.d. channel for a base station using a ULA consisting of hypothetical isotropic radiators spaced by $\lambda/2$, or a UCA consisting of 3 $\lambda/2$-dipoles. The analysis is extended to ULAs that consist of $\lambda/2$-dipoles, which are more realistic than isotropic radiators, and have a small mutual reactance. Numerical results are given in an i.i.d. channel, as well as in more realistic channels generated by QuaDRiGa.

Parts of this chapter have been published in [68] (©IEEE 2018) and presented at the 22nd International ITG Workshop on Smart Antennas (WSA 2018) [52].

4.1 Mutual Impedance of Isotropic Radiators

Antenna arrays are becoming more and more important in wireless communications, especially with Massive MIMO. The wireless communications literature typically considers ULAs consisting of (hypothetical) isotropic radiators spaced by $\lambda/2$, where λ is the wavelength of the carrier.

Hypothetical isotropic radiators are a special kind of antenna element: they radiate power uniformly into all directions (e.g. [36, Section 1.13]). They are hypothetical, since there are neither isotropic sources of coherent electromagnetic radiation nor of uniform spherical electromagnetic waves, but they are useful for theory [36, Sections 1.13 & 4.4]. Our intention is to find the mutual impedance between two hypothetical isotropic radiators.

According to literature [69], the mutual resistance between two hypothetical isotropic radiators is

$$R_{\text{hir}}(j\omega) = R_{\text{r}}\frac{\sin(\omega\tau)}{\omega\tau} = R_{\text{r}}\frac{\sin(kd)}{kd} = R_{\text{hir}}(jkc) \tag{4.1}$$

where R_{r} is the radiation resistance, ω is the angular frequency, τ is the time an electromagnetic wave needs to propagate the distance d between the radiators at the speed of light c and $k = 2\pi/\lambda = \omega/c$

is the angular wavenumber. Equation (4.1) has been derived by integration over a sphere enclosing the radiators while assuming that they are lossless, i.e., the entire power flowing into the radiators from some source is radiated.

In signal processing and wireless communications literature, the mutual impedance is usually assumed to be zero. For a ULA consisting of hypothetical isotropic radiators with an antenna separation d that is an integer multiple of $\lambda/2$, this is reasonable, since

$$R_{\mathrm{hir}} = 0\,\Omega \quad \text{for} \quad d = m\lambda/2, m \in \mathbb{N}. \tag{4.2}$$

But the imaginary part of the mutual impedance, i.e., the mutual reactance still has to be determined.

The mutual impedance between two hypothetical isotropic radiators, which are assumed to be canonical minimum scattering antennas [37], is [9]

$$Z_{\mathrm{hir}}(j\omega) = Z_{\mathrm{hir}}(jkc) = -\frac{R_{\mathrm{r}} e^{-jkd}}{jkd} = -\frac{R_{\mathrm{r}} e^{-j\omega\tau}}{j\omega\tau} \tag{4.3}$$

for large distances d. Its real part

$$\mathrm{Re}\left(Z_{\mathrm{hir}}\right) \equiv R_{\mathrm{hir}}, \tag{4.4}$$

c.f. (4.1), not only in the far-field, but also for arbitrary close distances, while in general, the near- and far-field of antennas is different. If (4.3) is also valid for arbitrary distances, the mutual reactance

$$X_{\mathrm{hir}}(j\omega) = \mathrm{Im}\left(Z_{\mathrm{hir}}(j\omega)\right) = R_{\mathrm{r}} \frac{\cos(\omega\tau)}{\omega\tau} = R_{\mathrm{r}} \frac{\cos(kd)}{kd} \tag{4.5}$$

should form a Hilbert transform pair together with $R_{\mathrm{hir}}(j\omega)$ [70, Ch. 8], as the transmission from one hypothetical isotropic radiator to another is passive, and thus $Z_{\mathrm{hir}}(j\omega)$ is the transfer function of a passive system. A similar relation holds for the radiation resistance $R_{\mathrm{r}}(j\omega)$ and the reactance $X_{\mathrm{r}}(j\omega)$ [70], which is used e.g. in [71]. In physics, these relations between the real and imaginary part of such a transfer function are called dispersion relations [72]:

$$R_{\mathrm{hir}}(j\omega) = \mathcal{H}\left\{X_{\mathrm{hir}}\right\}(j\omega) = \frac{1}{\pi}\,\mathrm{PV}\int_{-\infty\,\mathrm{s}^{-1}}^{\infty\,\mathrm{s}^{-1}} \frac{X_{\mathrm{hir}}(j\zeta)}{\omega - \zeta} d\zeta, \tag{4.6}$$

$$X_{\mathrm{hir}}(j\omega) = -\mathcal{H}\left\{R_{\mathrm{hir}}\right\}(j\omega) = -\frac{1}{\pi}\,\mathrm{PV}\int_{-\infty\,\mathrm{s}^{-1}}^{\infty\,\mathrm{s}^{-1}} \frac{R_{\mathrm{hir}}(j\zeta)}{\omega - \zeta} d\zeta, \tag{4.7}$$

where $\mathcal{H}\left\{X_{\mathrm{hir}}\right\}(j\omega)$ denotes the Hilbert transform of $X_{\mathrm{hir}}(j\omega)$ and PV stands for the Cauchy principal value. Technically, these relations are valid only if $Z_{\mathrm{hir}}(j\omega)$ does not have a pole at $\omega = 0\,\mathrm{s}^{-1}$ [72], but $Z_{\mathrm{hir}}(j\omega)$ does have such a pole. For a $Z_{\mathrm{hir}}(j\omega)$ that fulfills certain conditions, an additional summand on the right side of (4.7) is needed [72]. These conditions are[1]

1) $\lim\limits_{\omega\to\infty} Z_{\mathrm{hir}}(j\omega) = 0$.
2) $Z_{\mathrm{hir}}(\sigma + j\omega)$ needs to be holomorphic in the right half-plane, i.e., where $\sigma > 0$.

[1] In [72], a generalized susceptibility $\alpha(\omega) = \alpha'(\omega) + j\alpha''(\omega)$ is considered, which fulfills condition 1, and $\alpha(\omega' + j\omega'')$ is holomorphic in the upper half-plane ($\omega'' > 0$). In the transfer function described by the generalized susceptibility, the losses are caused by its imaginary part, whereas in an impedance, the losses are caused by its real part. Condition 2 results from an adaptation of the proof in [72] to an impedance, taking into account this different behavior and the changed variables in the argument.

The first condition holds. The second condition also holds, because $Z_{\mathrm{hir}}(j\omega)$ is the transfer function of a passive system [70, Section 8.1].

As $Z_{\mathrm{hir}}(j\omega)$ fulfills the required conditions, the dispersion relations for a transfer function with a pole at $\omega = 0$ hold [72]:

$$R_{\mathrm{hir}}(j\omega) = -\mathcal{H}\left\{X_{\mathrm{hir}}\right\}(j\omega) = \frac{1}{\pi}\,\mathrm{PV}\int_{-\infty\,\mathrm{s}^{-1}}^{\infty\,\mathrm{s}^{-1}} \frac{X_{\mathrm{hir}}(j\zeta)}{\omega-\zeta}d\zeta, \tag{4.8}$$

$$X_{\mathrm{hir}}(j\omega) = \mathcal{H}\left\{R_{\mathrm{hir}}\right\}(j\omega) + \frac{A}{\omega} = -\frac{1}{\pi}\,\mathrm{PV}\int_{-\infty\,\mathrm{s}^{-1}}^{\infty\,\mathrm{s}^{-1}} \frac{R_{\mathrm{hir}}(j\zeta)}{\omega-\zeta}d\zeta + \frac{A}{\omega}, \tag{4.9}$$

with $A = R_{\mathrm{r}}/\tau$ as $Z_{\mathrm{hir}}(j\omega)$ behaves like $jR_{\mathrm{r}}/(\omega\tau)$ near $\omega = 0$. These relations are derived in [72] by solving a contour integral in two different ways, and comparing the result: i) evaluating the integral directly, and ii) using the Cauchy integral theorem. The contour includes the entire imaginary axis, indented right at the poles of the integrand, and an infinite semicircle that closes the contour. When there is a pole at $\omega = 0\,\mathrm{s}^{-1}$, an additional infinitesimal semicircle is needed, which contributes the extra summand. The relations were used in [73] to compute the mutual reactance from the mutual resistance.

Using Hilbert transform tables [74, Ch. 13.7], we get

$$\mathcal{H}\left\{R_{\mathrm{hir}}\right\}(j\omega) + \frac{A}{\omega} = R_{\mathrm{r}}\frac{\cos(\omega\tau)-1}{\omega\tau} + \frac{R_{\mathrm{r}}}{\omega\tau} = \frac{\cos(\omega\tau)}{\omega\tau} \equiv X_{\mathrm{hir}}(j\omega), \tag{4.10}$$

i.e., this is identical to $X_{\mathrm{hir}}(j\omega)$. Therefore $Z_{\mathrm{hir}}(j\omega)$ is a valid function for the mutual impedance of hypothetical isotropic radiators for any distance d. For the considered case of electromagnetic radiation, the isotropic radiators are hypothetical, but they are of course realisitc in acoustics. With the corresponding free-space Green's function of the scalar Helmholtz equation, it can easily be verified that the mutual impendance derived by the dispersion relations is correct.

In [68], the difficulty with the pole was worked around by extending $Z_{\mathrm{hir}}(j\omega)$ to the complex variable $s = \sigma + j\omega, \sigma > 0\,\mathrm{s}^{-1}$ and evaluating the real part of $Z_{\mathrm{hir}}(s)$ as $\sigma \to 0\,\mathrm{s}^{-1}$. This yielded the same result as the procedure described in [70, Section 8.2] that consists in moving the pole of Z_{hir} from $\omega = 0\,\mathrm{s}^{-1}$ to some $s = \beta$ and evaluating the real part in the limit of moving the pole back, where $\beta < 0\,\mathrm{s}^{-1}$ to maintain stability. This workaround introduced an additional summand $-R_{\mathrm{r}}\pi/\tau\,\delta(\omega)$ in $Z_{\mathrm{hir}}(j\omega)$. Note however that $Z_{\mathrm{hir}}(j\omega)$ and $Z_{\mathrm{hir}}(j\omega) - R_{\mathrm{r}}\pi/\tau\,\delta(\omega)$ coincide for any $\omega \neq 0\,\mathrm{s}^{-1}$, i.e., there is no difference between them for a typical wireless communications scenario.

To the authors' best knowledge, this verification that Z_{hir} is a valid transfer function of a passive system for any distance d, has not been considered in literature yet.

Coming back to the ULA with antenna separation $d = m\lambda/2$, when we evaluate the mutual reactance, $X_{\mathrm{hir}} \neq 0\,\Omega$, i.e., the assumption that the mutual impedance is zero is not valid. We will assess the impact of still having this assumption in the next section.

4.2 Impact on Arrays with Zero Mutual Resistance

We consider a narrowband flat fading system with a base station having an antenna array consisting of N identical antenna elements with resistance R_{r} and reactance X_{r}, whose mutual resistance is zero, and assess the impact of the mutual reactance based on Multiport Communications Theory [8, 9]. In particular, we use the simplified model from Section 2.2 that does not consider a matching network.

The impedance matrix $\boldsymbol{Z}_{\mathrm{BS}} \in \mathbb{C}^{N\times N} \cdot \Omega$ of such an array fulfills

$$\boldsymbol{Z}_{\mathrm{BS}} = R_{\mathrm{r}}\boldsymbol{I} + j\boldsymbol{X}_{\mathrm{BS}}, \quad \mathrm{diag}(\boldsymbol{X}_{\mathrm{BS}}) = X_{\mathrm{r}}\boldsymbol{I}. \tag{4.11}$$

The impedance of infinitely thin $\lambda/2$-dipoles and the mutual impedance between them can be found in Section 2.4. For the isotropic radiators, we assume that their impedance is $R_{\mathrm{r}} = \mathrm{Re}(Z_{\lambda/2})$, i.e., that their reactance $X_{\mathrm{r}} = 0\,\Omega$.

4.2.1 Downlink

If we excite the antennas in the array with ideal current sources creating the current vector $\boldsymbol{i}$, the (instantaneous) radiated power is [9]

$$P_{\mathrm{T,i}} = \mathrm{Re}\left(\boldsymbol{i}^H\boldsymbol{u}\right) = \boldsymbol{i}^H\,\mathrm{Re}\left(\boldsymbol{Z}_{\mathrm{BS}}\right)\boldsymbol{i} = R_r\|\boldsymbol{i}\|_2^2, \tag{4.12}$$

which matches the notion that $P_{\mathrm{T,i}}$ is proportional to $\|\boldsymbol{i}\|_2^2$. Note that here, $P_{\mathrm{T,i}}$ is independent of $\boldsymbol{X}_{\mathrm{BS}}$, i.e., $P_{\mathrm{T,i}}$ is predicted correctly also when the mutual reactance $\boldsymbol{X}_{\mathrm{BS}}$ is ignored.

However in a real system, each antenna is excited by a power amplifier, which can be modeled as a linear voltage source with open load voltage $\boldsymbol{u}_{\mathrm{G}}$ and inner resistance $\boldsymbol{R} = R\boldsymbol{I}$, similar to Section 2.2. The (instantaneous) radiated power is [9]

$$P_{\mathrm{T,i}} = \frac{\boldsymbol{u}_{\mathrm{G}}^H\boldsymbol{B}\boldsymbol{u}_{\mathrm{G}}}{R}, \quad \boldsymbol{B} = R\left(\boldsymbol{Z}_{\mathrm{BS}} + \boldsymbol{R}\right)^{-H} R_{\mathrm{r}}\left(\boldsymbol{Z}_{\mathrm{BS}} + \boldsymbol{R}\right)^{-1}, \tag{4.13}$$

similar to (2.17), where $\boldsymbol{Z}_{11} = \boldsymbol{Z}_{\mathrm{BS}}$ and $R_{\mathrm{G}} = R$. This expression *does* depend on $\boldsymbol{X}_{\mathrm{BS}}$, i.e., if we neglect $\boldsymbol{X}_{\mathrm{BS}}$ and predict the (instantaneous) radiated power similarly to (3.18) and (3.20), we have

$$P_{\mathrm{T,p,i}} = \frac{\boldsymbol{u}_{\mathrm{G}}^H\hat{\boldsymbol{B}}\boldsymbol{u}_{\mathrm{G}}}{R}, \quad \hat{\boldsymbol{B}} = R\frac{R_{\mathrm{r}}}{(R_{\mathrm{r}}+R)^2 + X_{\mathrm{r}}^2}\boldsymbol{I}, \tag{4.14}$$

and obtain some $P_{\mathrm{T,p,i}} \neq P_{\mathrm{T,i}}$. Note that in contrast to $P_{\mathrm{T,i}}$, $P_{\mathrm{T,p,i}}$ does not depend on the direction of $\boldsymbol{u}_{\mathrm{G}}$ [22].

Section 2.2 shows how Multiport Communications Theory introduces a transform from the random transmit vectors $\boldsymbol{x}$ and $\hat{\boldsymbol{x}}$ to the information theoretic domain and to the information theoretic domain neglecting the mutual reactance, such that

$$P_{\mathrm{T}} = \mathrm{E}[P_{\mathrm{T,i}}] \;\; = \mathrm{E}[\|\boldsymbol{x}\|_2^2], \tag{4.15}$$

$$P_{\mathrm{T,p}} = \mathrm{E}[P_{\mathrm{T,p,i}}] = \mathrm{E}[\|\hat{\boldsymbol{x}}\|_2^2]. \tag{4.16}$$

At the receiver side, the received signal $\boldsymbol{y}$ in the information theoretic domain is obtained by a noise whitening of the load voltage $\boldsymbol{u}_{\mathrm{L}}$, which is measured across the input impedance $Z_{\mathrm{L}} = R$ of the LNA in each RF chain [9], see Section 2.2.2. We choose $R = R_{\mathrm{r}}$ in the simulations, such that there is power matching at the receiver and at the transmitter for hypothetical isotropic radiators, and a matching of the resistance for $\lambda/2$-dipoles, which is heuristic. In the simulations, we will use the noise parameters from [66], but with input impedance R of the LNA.

We consider the (hypothetical) predicted radiated power $P_{\mathrm{T,p}}$ when neglecting the mutual reactance and the ergodic rates in the downlink transmitting to a mobile with a single hypothetical isotropic radiator as an antenna.

Let us assume the i.i.d. channel similar to Section 3.4, where $\boldsymbol{Z}_{21} = \boldsymbol{z}^T$,

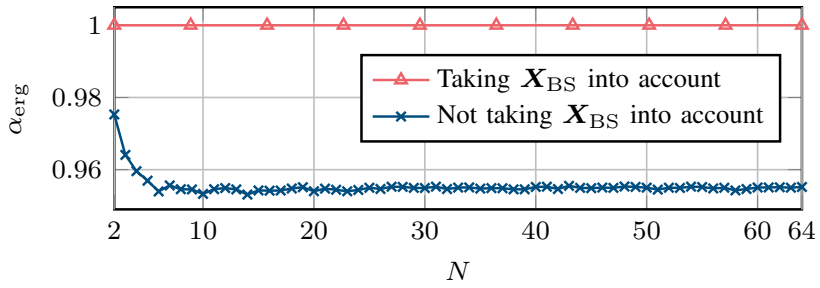

Fig. 4.1. Ergodic ratio of true and predicted power for a ULA consisting of hypothetical isotropic radiators spaced by $\lambda/2$ [68]. (©IEEE 2018)

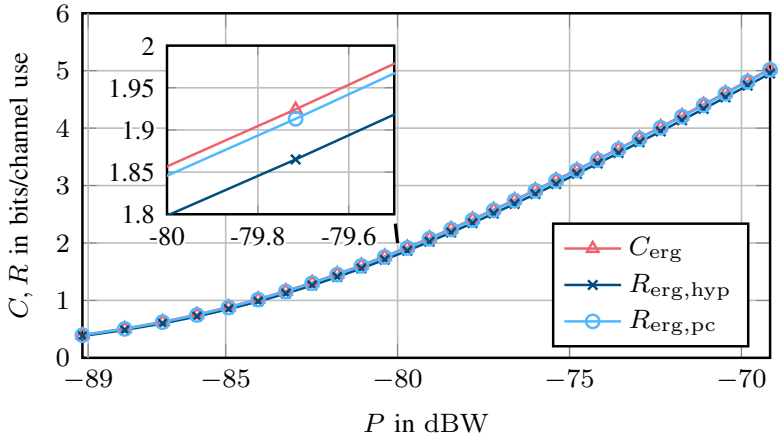

Fig. 4.2. Ergodic downlink rates of a ULA consisting of 64 isotropic radiators spaced by $\lambda/2$ with and without neglecting $\boldsymbol{X}_{\mathrm{BS}}$ [68]. (©IEEE 2018)

$$\boldsymbol{z} \sim \mathcal{N}_{\mathbb{C}}(\boldsymbol{0}\,\Omega, \sigma_z^2 \boldsymbol{I}), \quad \boldsymbol{D} = \frac{R}{R_{\mathrm{r}} + jX_{\mathrm{r}} + R} \boldsymbol{z}^T (\boldsymbol{Z}_{\mathrm{BS}} + \boldsymbol{R})^{-1}. \tag{4.17}$$

We assume that the base station obtains perfect channel knowledge of $\boldsymbol{d}$, e.g. through channel state feedback or through exploiting reciprocity and estimating the channel in the uplink.

The ergodic capacity C_{erg} and the hypothetical rate when neglecting the mutual reactance $R_{\mathrm{erg,hyp}}$, for a given power P, can be computed in the same way as when taking and not taking the mutual coupling into account, as shown in Section 3.3. Note that when the mutual reactance is neglected, there are two kinds of losses: the suboptimal beamforming vector $\boldsymbol{f}_{\mathrm{hyp}}$, see (3.24), is chosen to obtain $R_{\mathrm{erg,hyp}}$, and the base station does not know how to compute P_{T}, and computes $R_{\mathrm{erg,hyp}}$ based on $P_{\mathrm{T,p}}$ instead. To separate both losses, we consider the ratio (3.26) and compute the power corrected ergodic rate

$$R_{\mathrm{erg,pc}}(P) = \mathrm{E}\left[R_{\mathrm{hyp}}(P/\alpha)\right], \tag{4.18}$$

where power corrected means that $P_{\mathrm{T}} = P$ holds, but $\boldsymbol{f}_{\mathrm{hyp}}$ is used. This way, $R_{\mathrm{erg,pc}}(P) \approx R_{\mathrm{erg,hyp}}(P/\alpha_{\mathrm{erg}})$ for high SNR, where

$$\alpha_{\mathrm{erg}} = \exp(\ln(2)\,\mathrm{E}[\log_2 \alpha]), \tag{4.19}$$

i.e., for high SNR, $R_{\mathrm{erg,pc}}$ is $R_{\mathrm{erg,hyp}}$ shifted by $-10\log_{10}(\alpha_{\mathrm{erg}})\,\mathrm{dB}$ in a semi-log plot.

The capacities, rates and α are computed by a Monte Carlo simulation of 1000 channel realizations with $\sigma_z \approx 0.019\,085\,\Omega$. α_{erg} then becomes the geometric mean of α over all channel

Table 4.1. Ergodic ratio of true and predicted power for a UCA consisting of 3 $\lambda/2$-dipoles spaced by d_1 [68]. (©IEEE 2018)

	Taking $\boldsymbol{X}_{\mathrm{BS}}$ into account	Not taking $\boldsymbol{X}_{\mathrm{BS}}$ into account
α_{erg}	1 (by design)	0.912 ($\approx -0.40\,\mathrm{dB}$)

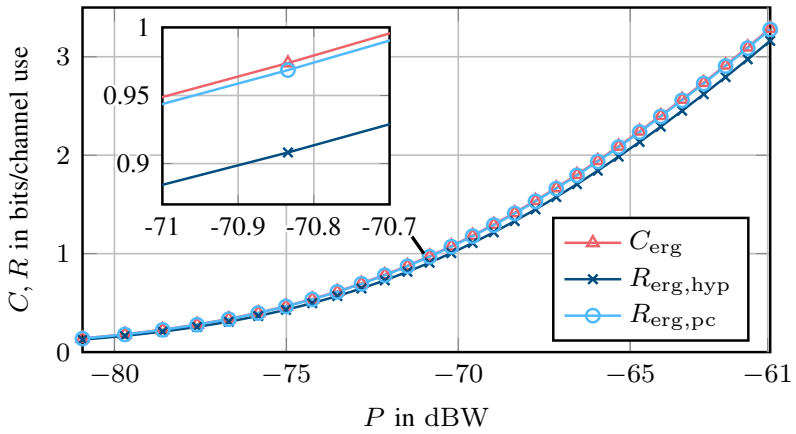

Fig. 4.3. Ergodic downlink rates of a 3 antenna UCA consisting of $\lambda/2$-dipoles spaced d_1 with and without neglecting $\boldsymbol{X}_{\mathrm{BS}}$ [68]. (©IEEE 2018)

realizations. Firstly, let us consider a ULA consisting of hypothetical isotropic radiators spaced by $\lambda/2$ at the base station. Fig. 4.1 shows α_{erg}. It decreases as the number of antennas increases and saturates around $95.5\,\% \approx -0.2\,\mathrm{dB}$, i.e., on average $0.2\,\mathrm{dB}$ less power is radiated than predicted when the mutual reactance is neglected. For one stream, this translates to a loss of about $0.066\,\mathrm{bpcu}$ (bits per channel use), but $R_{\mathrm{erg,hyp}}$ at high SNR is even $0.081\,\mathrm{bpcu}$ smaller than C_{erg} (Fig. 4.2) due to the suboptimal beamforming vector.

Secondly, let us consider a UCA consisting of 3 $\lambda/2$-dipoles spaced by $d_1 \approx 0.42967\lambda$, the first zero of the mutual resistance of lossless and infinitely thin $\lambda/2$-dipoles. As the distance between all dipoles is identical, the mutual resistance between every pair of them is zero. For more antennas, it is not possible to find a planar array with zero mutual resistance in general, since the zeros of the mutual resistance are not equidistant, in contrast to hypothetical isotropic radiators. Here, the impact of neglecting the mutual reactance is even larger, as $R_{\mathrm{erg,hyp}}$ at high SNR is $0.14\,\mathrm{bpcu}$ smaller than C_{erg}, and the smaller than predicted radiated power accounts for about $0.40\,\mathrm{dB} \approx 0.13\,\mathrm{bpcu}$ (c.f Table 4.1), i.e., it dominates over the impact of the suboptimal beamforming vector $\boldsymbol{f}_{\mathrm{hyp}}$ here (Fig. 4.3), just as for the ULA (Fig 4.2).

4.2.2 Uplink

Consider receiving from a single antenna mobile with a hypothetical isotropic radiator using the same model as in the downlink, (2.18), but with the transposed channel $\boldsymbol{z}$, i.e., $\boldsymbol{x}$ is a scalar x, $\boldsymbol{h} = \boldsymbol{H}$ and $\hat{\boldsymbol{h}} = \hat{\boldsymbol{H}}$. The receiver will use the matched filter

$$\boldsymbol{g} = \boldsymbol{h}/\|\boldsymbol{h}\|_2, \quad \tilde{x} = \boldsymbol{g}^H \boldsymbol{y}, \tag{4.20}$$

which achieves the capacity $C_{\mathrm{UL,erg}}$. Namely for a given P_{T},

$$C_{\mathrm{UL,erg}}(P_{\mathrm{T}}) = \mathrm{E}\left[\log_2\left(1 + \|\boldsymbol{h}\|_2^2 P_{\mathrm{T}}/\sigma_\vartheta^2\right)\right]. \tag{4.21}$$

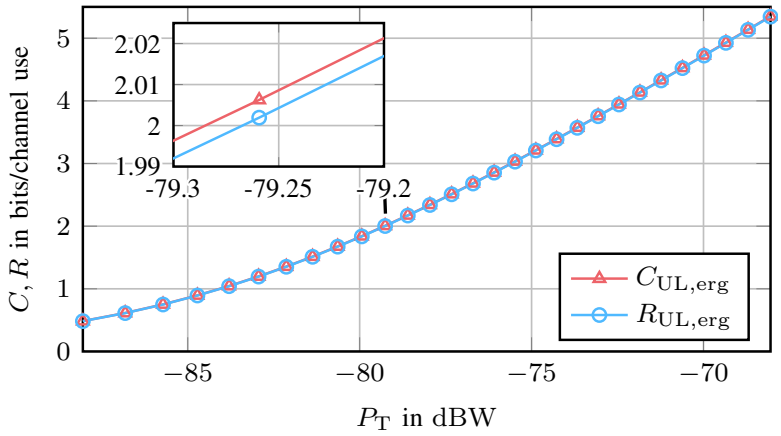

Fig. 4.4. Ergodic uplink rates of a ULA consisting of 64 isotropic radiators spaced by $\lambda/2$ with and without neglecting $\boldsymbol{X}_{\mathrm{BS}}$ [68]. (©IEEE 2018)

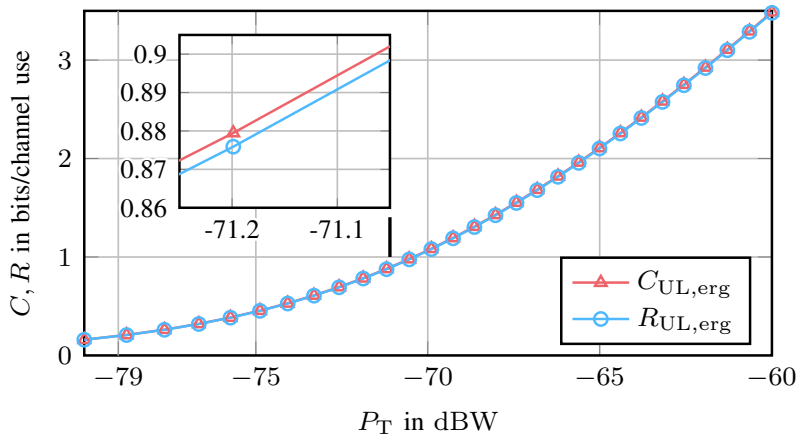

Fig. 4.5. Ergodic uplink rates of a 3 antenna UCA consisting of $\lambda/2$-dipoles spaced by d_1 with and without neglecting $\boldsymbol{X}_{\mathrm{BS}}$ [68]. (©IEEE 2018)

The mutual reactance makes the noise between the antennas correlated according to the model for $\boldsymbol{R}_\eta$ from Section 2.2.1, while it is uncorrelated with zero mutual reactance, as the mutual resistance of the arrays we consider is zero as well. Let $\hat{\boldsymbol{R}}_\eta$ be the covariance matrix of $\boldsymbol{\eta}$ the base station assumes when it does not take the mutual reactance into account, i.e., the entries of $\boldsymbol{\eta}$ are uncorrelated and $\hat{\boldsymbol{R}}_\eta$ is diagonal. Let us assume that the base station estimates this matrix without any error. According to (2.19) and with the mapping

$$\hat{\boldsymbol{y}} = \sigma_\vartheta / \sqrt{R} \hat{\boldsymbol{R}}_\eta^{-1/2} \boldsymbol{u}_{\mathrm{L}}, \quad \hat{\boldsymbol{R}}_\eta = \mathrm{diag}(\boldsymbol{R}_\eta), \tag{4.22}$$

the information theoretic model when not taking the mutual reactance into account is

$$\begin{aligned} \hat{\boldsymbol{y}} &= \hat{\boldsymbol{h}} x + \hat{\boldsymbol{\vartheta}}, \quad \hat{\boldsymbol{h}} = \sigma_\vartheta \hat{\boldsymbol{R}}_\eta^{-1/2} \boldsymbol{D} \boldsymbol{B}^{-H/2}, \\ \hat{\boldsymbol{\vartheta}} &\sim \mathcal{N}_{\mathbb{C}}(\boldsymbol{0}\sqrt{\mathrm{W}}, \boldsymbol{R}_{\hat{\vartheta}}), \quad \boldsymbol{R}_{\hat{\vartheta}} = \hat{\boldsymbol{R}}_\eta^{-1/2} \boldsymbol{R}_\eta \hat{\boldsymbol{R}}_\eta^{-H/2}, \end{aligned} \tag{4.23}$$

although $\hat{\boldsymbol{\vartheta}}$ is expected to be white noise. After applying the matched filter

$$\hat{\boldsymbol{g}} = \hat{\boldsymbol{h}} / \|\hat{\boldsymbol{h}}\|_2, \quad \tilde{\hat{x}} = \hat{\boldsymbol{g}}^H \hat{\boldsymbol{y}}, \tag{4.24}$$

the rate when not taking the mutual reactance into account is

$$R_{\mathrm{UL,erg}}(P_{\mathrm{T}}) = \mathrm{E}\left[\log_2\left(1 + P_{\mathrm{T}}\|\hat{\boldsymbol{h}}\|_2^4/(\hat{\boldsymbol{h}}^H\boldsymbol{R}_{\hat{\vartheta}}\hat{\boldsymbol{h}})\right)\right]. \tag{4.25}$$

Let us consider the impact of ignoring the mutual reactance on the rates in the uplink for the same base station antenna arrays as in Section 4.2.1. As in the downlink, the ergodic rates $C_{\mathrm{UL,erg}}$ and $R_{\mathrm{UL,erg}}$ are computed by a Monte Carlo simulation over 1000 channel realizations, c.f. Fig. 4.4 for the ULA and Fig. 4.5 for the UCA. Compared to the downlink, there is a smaller gap between ergodic capacity and rate when the mutual reactance is neglected, since there is only a loss due to the suboptimal equalizer $\hat{\boldsymbol{g}}$, but no difference in the radiated power, i.e., $P_{\mathrm{T,p}} = P_{\mathrm{T}}$ as the mobile only has a single antenna.

4.3 Impact on Arrays with a Small Mutual Resistance

In the previous section, we have considered lossless antenna arrays with identical antenna elements at the base station, where the mutual resistance between the elements is zero. As isotropic radiators are hypothetical, other types of antennas need to be used in practice, but in general arrays consisting of these antennas do not have zero mutual resistance, but some (small) mutual resistance since the zeros of the mutual resistance are not equidistant in general. Thus in this section, we want to consider more practical antenna arrays with small mutual resistance. The following analysis also applies if it is not small, but that would lead to different simulation results. The impedance matrix of the array can be written

$$\boldsymbol{Z}_{\mathrm{BS}} = \boldsymbol{R}_{\mathrm{BS}} + j\boldsymbol{X}_{\mathrm{BS}}, \tag{4.26}$$

where $\boldsymbol{R}_{\mathrm{BS}}$ is the mutual resistance matrix, which is symmetric positive semidefinite.

In this case, the (instantaneous) radiated power is

$$P_{\mathrm{T,i}} = \boldsymbol{i}^H \operatorname{Re}(\boldsymbol{Z}_{\mathrm{BS}})\,\boldsymbol{i} = \boldsymbol{i}^H\boldsymbol{R}_{\mathrm{BS}}\boldsymbol{i}, \tag{4.27}$$

when the antennas in the array are excited by ideal current sources $\boldsymbol{i}$. Note that due to the mutual resistance, $P_{\mathrm{T,i}}$ is still directly proportional to $\|\boldsymbol{i}\|_2^2$, but contrary to (4.12), the proportionality factor is not constant and different from R_{r} in general.

If more realistic linear power amplifiers are used to excite the antenna array, similarly to (4.13), the (instantaneous) radiated power can be computed as

$$P_{\mathrm{T,i}} = \frac{\boldsymbol{u}_{\mathrm{G}}^H\boldsymbol{B}\boldsymbol{u}_{\mathrm{G}}}{R}, \qquad \boldsymbol{B} = R\left(\boldsymbol{Z}_{\mathrm{BS}} + \boldsymbol{R}\right)^{-H}\boldsymbol{R}_{\mathrm{BS}}\left(\boldsymbol{Z}_{\mathrm{BS}} + \boldsymbol{R}\right)^{-1}, \tag{4.28}$$

similarly to (4.13), and P_{T} according to (4.15), but with this updated definition of $P_{\mathrm{T,i}}$, similarly to (2.16). If the base station neglects the mutual impedance, i.e., it assumes that $\boldsymbol{Z}_{\mathrm{BS}}$ is diagonal, it predicts the (hypothetical instantaneous) radiated power via (4.14) and (4.16), similarly as when the mutual reactance is neglected for an array with zero mutual resistance.

We will compare the results for the ULA consisting of hypothetical isotropic radiators spaced by $\lambda/2$ with one consisting of $\lambda/2$-dipoles. For the latter,

$$\max_{\substack{k,l\\k\neq l}} |[\boldsymbol{R}_{\mathrm{BS}}]_{k,l}| \approx 0.171\,[\boldsymbol{R}_{\mathrm{BS}}]_{k,k} \tag{4.29}$$

holds for $N = 2, \ldots, 64$, and the maximum is attained for $|k - l| = 1$, i.e., the mutual resistance is indeed small.

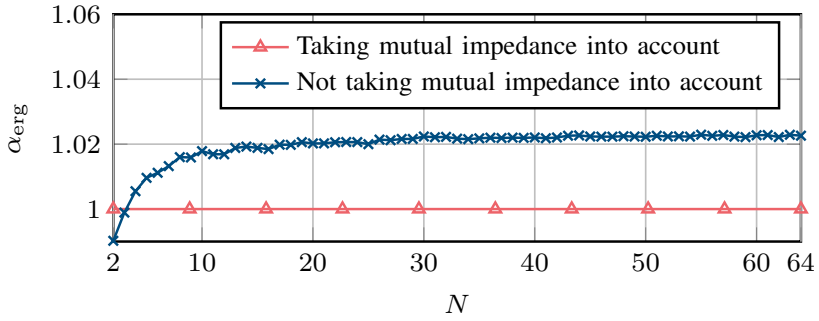

Fig. 4.6. Ergodic ratio α_{erg} of true and predicted power for a ULA consisting of $\lambda/2$-dipoles spaced by $\lambda/2$ in an i.i.d. channel [52].

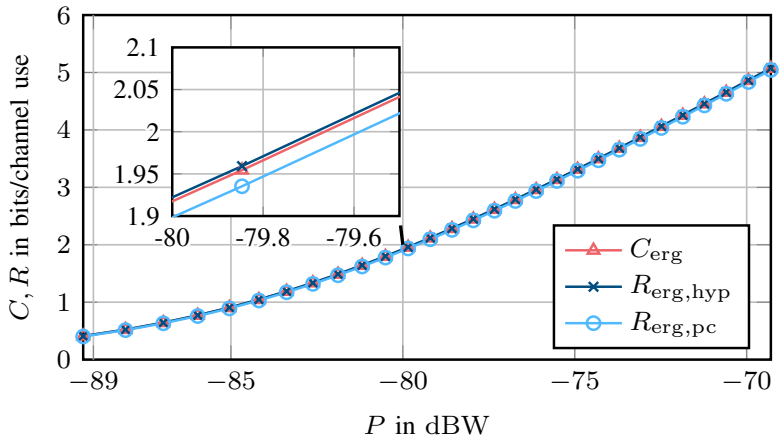

Fig. 4.7. Ergodic downlink rates of a ULA consisting of 64 $\lambda/2$-dipoles spaced by $\lambda/2$ with and without neglecting the mutual impedance in an i.i.d. channel [52].

4.3.1 Downlink

In the downlink, we consider the transmission of the base station to a mobile with a single $\lambda/2$-dipole as an antenna, similarly as in Section 4.2.1. Firstly, consider the ergodic ratio of true and predicted radiated power α_{erg}. Let us compare Figs. 4.1 and 4.6. Note that not taking $\boldsymbol{X}_{\text{BS}}$ into account and not taking the mutual impedance into account is the same for the ULA consisting of hypothetical isotropic radiators, since its mutual resistance is zero. We see that for this type of array, α_{erg} saturates around $95.5\,\%$ already at about $N = 7$, but with $\lambda/2$-dipoles, it saturates for larger N and reaches about $102.3\,\%$. That means, for larger N, on average a slightly different amount of power than predicted is radiated by the arrays – about $0.2\,\text{dB}$ less for the former (see Section 4.2.1) and about $0.099\,\text{dB}$ more for the latter.

Secondly, consider the ergodic capacity C_{erg}, the hypothetical rate $R_{\text{erg,hyp}}$ and the power corrected ergodic rate $R_{\text{erg,pc}}$ for a given power P. Consider the ULAs with $N = 64$ antennas. Fig. 4.2 corresponds to that consisting of hypothetical isotropic radiators and shows that R_{hyp} is $0.081\,\text{bpcu}$, smaller than C_{erg} at high SNR, where using $P_{\text{T,p}}$ results in a smaller average radiated power that accounts for $0.066\,\text{bpcu}$, which is exactly the gap between $R_{\text{erg,hyp}}$ and $R_{\text{erg,pc}}$ at high SNR, see Section 4.2.1. That means, here the influence of the smaller average radiated power dominates over the suboptimal beamforming vector. Let us compare that to the ULA consisting of $\lambda/2$-dipoles, see Fig. 4.7. Here $R_{\text{erg,hyp}}$ is slightly larger than C_{erg} – $0.0061\,\text{bpcu}$ at high SNR – due to the larger

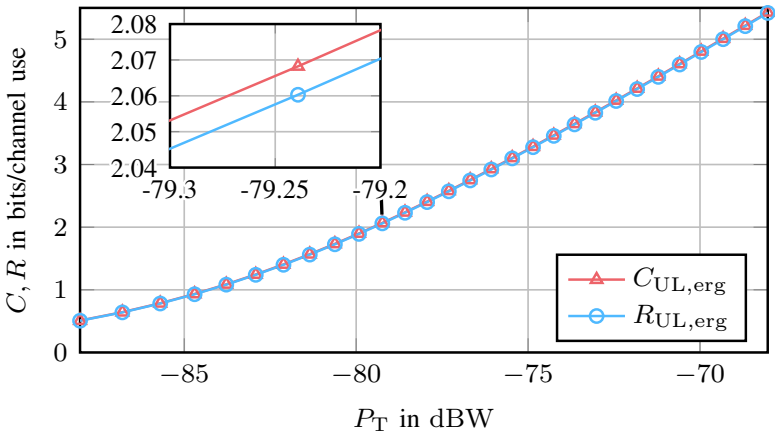

Fig. 4.8. Ergodic uplink rates of a ULA consisting of 64 $\lambda/2$-dipoles spaced by $\lambda/2$ with and without neglecting the mutual impedance in an i.i.d. channel [52].

average radiated power. The gap between $R_{\mathrm{erg,pc}}$ and C_{erg} is $0.025\,\mathrm{bpcu}$, i.e., the effect of the larger radiated power and that of the suboptimal beamforming vector are about the same scale.

The gap between C_{erg} and $R_{\mathrm{erg,pc}}$ and between $R_{\mathrm{erg,pc}}$ and $R_{\mathrm{erg,hyp}}$ is a bit larger for the ULA consisting of $\lambda/2$-dipoles than for that consisting of isotropic radiators, but still on the same order of magnitude. However, neglecting the mutual impedance leads to a larger instead of a smaller radiated power and $R_{\mathrm{erg,hyp}}$ for the former.

4.3.2 Uplink

In the uplink, the mobile transmits over the transposed channel, similarly to Section 4.2.2. When we compare the results for ergodic capacity and rate neglecting the mutual impedance for both arrays (see Figs. 4.4 and 4.8), the rates are almost the same. In both cases, $R_{\mathrm{UL,erg}}$ is a little bit smaller than $C_{\mathrm{UL,erg}}$, about $0.0058\,\mathrm{bpcu}$ with the isotropic radiators and $0.010\,\mathrm{bpcu}$ with the $\lambda/2$-dipoles at high SNR. The gap between them only results from a suboptimal equalizer that does not take into account the noise correlations between the antennas, introduced by the mutual impedance. The predicted and (true) radiated power are the same, as the mobile only has a single antenna. That means, also in the uplink, the gap for the ULA consisting of hypothetical isotropic radiators and that for the ULA consisting of $\lambda/2$-dipoles are on the same order of magnitude.

So far, we have only considered an i.i.d. channel. In the next section, we consider a more realistic channel model.

4.4 Simulation Results with QuaDRiGa

In this section, we consider the QuaDRiGa channel model, see Section 3.5. QuaDRiGa assumes that isotropic radiators are vertically polarized. The orientation of the ULA at the base station is such that it is parallel to the ground, centered and perpendicular to one of the long diagonals of the hexagon. In this section, we compare the two ULAs we already compared for the i.i.d. channel: one consisting of isotropic radiators and one consisting of $\lambda/2$-dipoles. All antenna elements are oriented vertically.

In Figs. 4.9 and 4.10, we can see that compared to Figs. 4.1 and 4.6, α_{erg} saturates at lower values, $91\,\% \approx -0.41\,\mathrm{dB}$ and $93\,\% \approx -0.32\,\mathrm{dB}$. That means for more realistic channels it may be more important not to neglect the mutual impedance than in an i.i.d. channel. Interestingly for

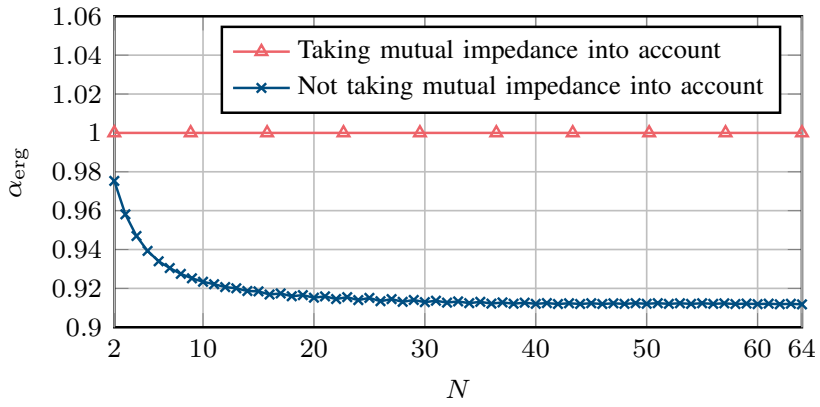

Fig. 4.9. Ergodic ratio α_{erg} of true and predicted power for a ULA consisting of isotropic radiators spaced by $\lambda/2$ in a UMa channel [52].

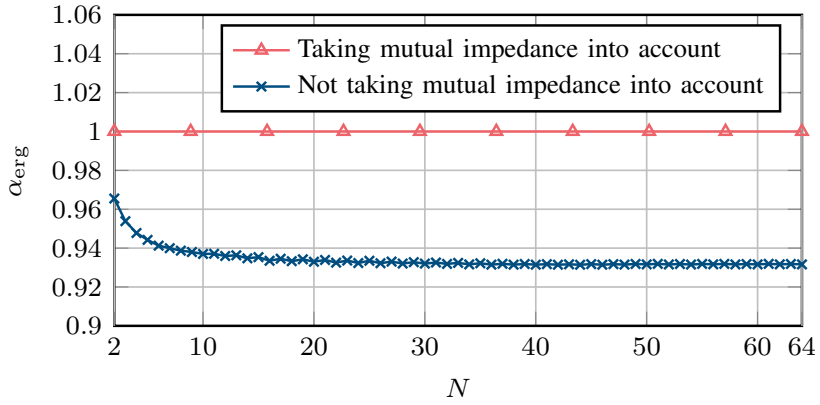

Fig. 4.10. Ergodic ratio α_{erg} of true and predicted power for a ULA consisting of $\lambda/2$-dipoles spaced by $\lambda/2$ in a UMa channel [52].

the ULA of $\lambda/2$-dipoles, $\alpha_{\text{erg}} < 1$ in the UMa channel model, but $\alpha_{\text{erg}} > 1$ for $N \geq 4$ in the i.i.d. channel model, see Figs. 4.6 and 4.10.

Let us assume that the base station radiates $10\,\text{W}$ in a channel bandwidth of $20\,\text{MHz}$. If the power is equally spread among this bandwidth, $7.5\,\text{mW} \approx -21\,\text{dBW}$ are radiated on one subcarrier with $15\,\text{kHz}$ bandwidth. Similarly a transmit power of the mobile of $100\,\text{mW}$ corresponds to $75\,\mu\text{W} \approx -41\,\text{dBW}$.

Compared to the i.i.d. channel, significantly more power is needed to achieve the same ergodic capacity or rate, as σ_z for the i.i.d. channel (see (4.17)) at $3.5\,\text{GHz}$ center frequency corresponds to a line-of-sight (LOS) channel in free space between two parallel $\lambda/2$-dipoles spaced roughly $85.7\,\text{m}$. In the UMa model however, there is additional attenuation since mobiles can be indoor or have non-LOS reception. Also, the mobiles can be further away from the base station, between $35\,\text{m}$ and about $289\,\text{m}$. This leads to a large variation in the rates, see Fig. 4.15 for the cumulative distribution function of the downlink capacity and rates for $N = 64$. Note that this distribution is only for one narrowband subcarrier and as the channel is frequency selective due to multi-path propagation, for one channel realization, other subcarriers may support a significantly higher or smaller rate, so a good resource allocation is needed.

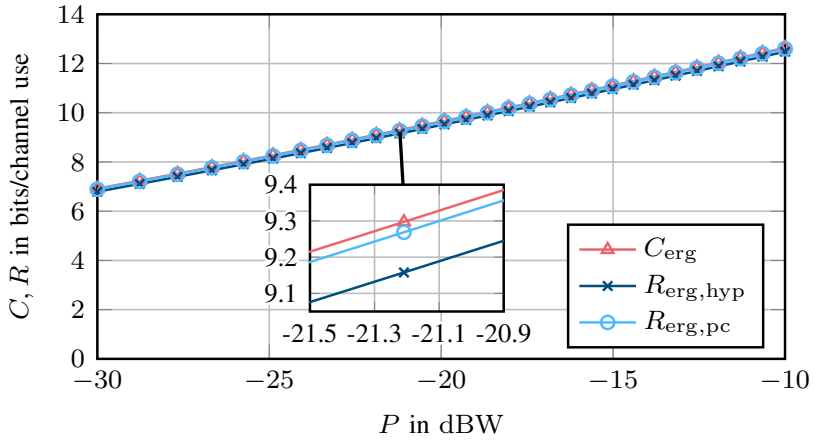

Fig. 4.11. Ergodic downlink rates of a ULA consisting of 64 isotropic radiators spaced by $\lambda/2$ with and without neglecting the mutual impedance in a UMa channel (modified from [52]).

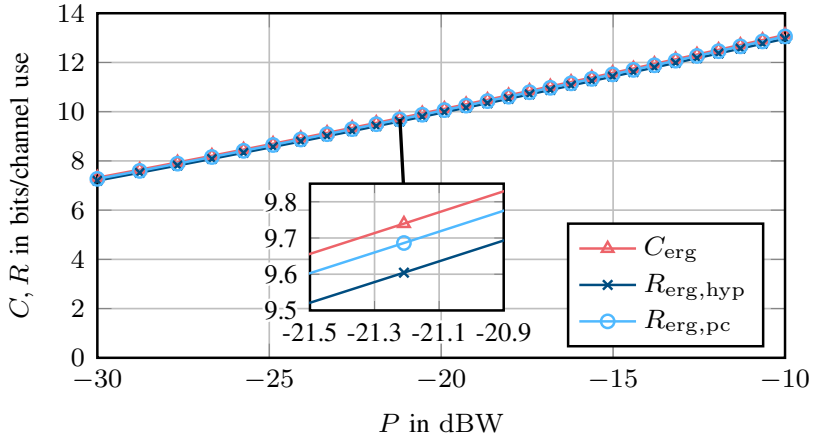

Fig. 4.12. Ergodic downlink rates of a ULA consisting of 64 $\lambda/2$-dipoles spaced by $\lambda/2$ with and without neglecting the mutual impedance in a UMa channel (modified from [52]).

When we compare Figs. 4.11 and 4.12, and 4.13 and 4.14, we can see that the ergodic rates and capacities are higher with the $\lambda/2$-dipoles at the base station, which means that the directivity of the $\lambda/2$-dipoles is beneficial in the UMa channel model.

In the downlink the gap between C_{erg} and $R_{\mathrm{erg,hyp}}$ at high SNR is significantly larger than in the i.i.d. channel model – $0.16\,\mathrm{bpcu}$ for the isotropic radiators and $0.17\,\mathrm{bpcu}$ for the $\lambda/2$-dipoles compared to $0.081\,\mathrm{bpcu}$ and $0.0015\,\mathrm{bpcu}$ respectively. In power, at $P = 7.5\,\mathrm{mW}$, this translates to a loss of $0.43\,\mathrm{dB}$ and $0.37\,\mathrm{dB}$, which is not negligible.

In the uplink, the gap between $C_{\mathrm{UL,erg}}$ and $R_{\mathrm{UL,erg}}$ at high SNR is larger as well, $0.0095\,\mathrm{bpcu}$ for the isotropic radiators and $0.014\,\mathrm{bpcu}$ for the $\lambda/2$-dipoles compared to $0.0058\,\mathrm{bpcu}$ and $0.010\,\mathrm{bpcu}$ respectively. At $P_{\mathrm{T}} = 75\,\mu\mathrm{W}$, this translates to a loss of $0.017\,\mathrm{dB}$ and $0.030\,\mathrm{dB}$ respectively, which might be negligible in practice.

4.5 Conclusion

In this chapter, we have computed the mutual reactance of hypothetical isotropic radiators based on passivity and the dispersion relations, and we have investigated the influence of the mutual impedance

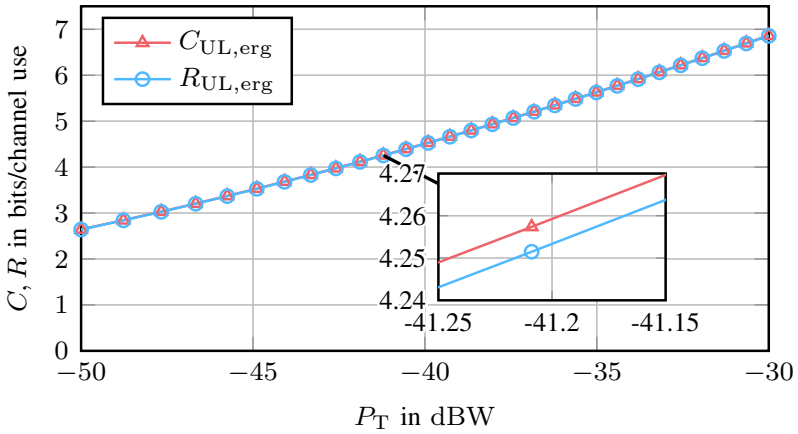

Fig. 4.13. Ergodic uplink rates of a ULA consisting of 64 isotropic radiators spaced by $\lambda/2$ with and without neglecting the mutual impedance in a UMa channel (modified from [52]).

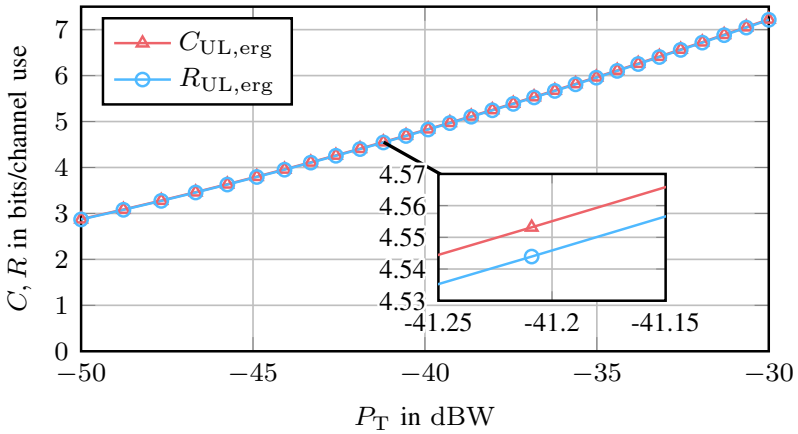

Fig. 4.14. Ergodic uplink rates of a ULA consisting of 64 $\lambda/2$-dipoles spaced by $\lambda/2$ with and without neglecting the mutual impedance in a UMa channel (modified from [52]).

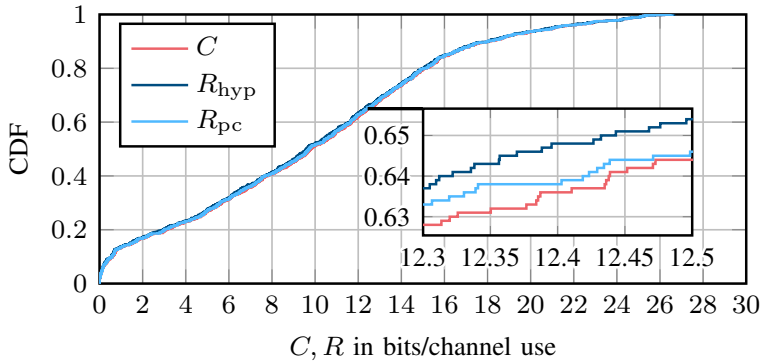

Fig. 4.15. Cumulative distribution function (CDF) of the downlink rates of a ULA consisting of 64 $\lambda/2$-dipoles spaced by $\lambda/2$ with and without neglecting the mutual impedance in a UMa channel for $P = 7.5\,\mathrm{mW}$ (modified from [52]).

on antenna arrays with zero mutual resistance, and on arrays with a small mutual resistance. We have found that in receive mode, the mutual impedance makes the noise correlated between the antennas, and in transmit mode it changes the amount of radiated power when they are driven by linear radio frequency amplifiers instead of ideal current sources. We have also compared the achievable rates when neglecting the mutual impedance and the capacities numerically in an i.i.d. channel. The impact of neglecting the mutual impedance on the radiated power and on the rates in the scenarios considered is relatively small. The impact for the ULAs consisting of $\lambda/2$-dipoles on the ergodic rates is a bit larger compared to that consisting of hypothetical isotropic radiators, but still on the same order of magnitude.

Furthermore, simulation results for a more realistic channel model without mobility, based on the TS 38.901 UMa channel model in QuaDRiGa, show that the effect of neglecting the mutual impedance is larger there, than in an i.i.d. channel, and that the losses in the downlink are non-negligible. Also in with these channels, the losses with the $\lambda/2$-dipoles are larger than with hypothetical isotropic radiators.

The impact of neglecting the mutual impedance on the radiated power and on the rates should be taken into account. The power-coupling matrix and the noise correlations it creates can be determined offline at the design stage, as they do not depend on the time-variance of the mobile communication channel.

5. Limits of Array Gain

5.1 Introduction

In this chapter, we consider the transmit and receive antenna array gain of massive MIMO systems. In particular, we look at their dependence on the number of antennas in the array, and the antenna spacing for uniform linear and uniform circular arrays. It is known that the transmit array gain saturates at a certain antenna spacing, but the receive array gain had not been considered. With our physically consistent analysis based on the Multiport Communication Theory, we show that the receive array gain does not saturate, but that there is a peak at a certain antenna spacing when there is no decoupling network at the receiver. As implementing a decoupling network for massive MIMO would be almost impossible, this is a reasonable assumption. Furthermore, we analyze how the array gain changes depending on the antenna spacing and the size of the antenna array and derive design recommendations.

Massive MIMO is an important building block of future wireless systems, as, depending on the scenario, a larger number of base station antennas is believed to increase the achievable transmit and receive array gain, i.e., it allows for a larger SNR at the same transmit power, a lower bit error ratio by exploiting diversity, or to serve more mobiles at the same time. Indeed, the seminal paper [4] that introduced massive MIMO is based on the assumption that there is an unlimited number of base station antennas. However for realistic systems, does increasing the number of base station antennas always improve performance?

In [13], it has been shown for a UCA at the base station transmitting to a mobile over an LOS channel (without reflections) that in general the minimum energy per bit $E_{\mathrm{b,min}}$, which is inversely proportional to the transmit array gain, decreases as the number of antennas at the base station increases, but at a certain number of base station antennas, $E_{\mathrm{b,min}}$ saturates. The analysis is based on Multiport Communication Theory [8, 9], which is in turn based on circuit theory and ensures that the analysis is physically consistent.

One contribution of this chapter is to extend the analysis to the receive array gain. We also want to extend the analysis to antenna arrays, where the antenna separation is fixed rather than the array size. Note that transmit and receive array gain are different, unless the noise at the receiver fulfills certain properties [8], as we define array gain as the ratio of SNRs instead of powers. Another contribution of this chapter is to look at how the array gain changes if both antenna spacing and array size vary and derive design recommendations. The influence of mutual coupling on transmit array gain has already been investigated early [75]. Experimental results were provided in [76], but only for small arrays and without investigating the difference between transmit and receive array gain.

URAs are the most common antenna array type employed in today's cellular mobile systems at the base station site. They consist of several rows and columns. Typically the antenna elements are realized as dual-polarized elements with $\pm 45^\circ$ polarization. A novel dual-polarized antenna element on a substrate for this application can be found, e.g., in [77]. In the first part of this chapter, we analyze the transmit array gain for ULAs and UCAs in the far field, where all antennas are polarized vertically. In the second part, we want to extend the analysis to URAs, and to dual-polarized crossed $\lambda/2$-dipoles with $\pm 45^\circ$ polarization.

The analysis of vertically polarized ULAs and UCAs has been presented at the 2020 IEEE Wireless Communications and Networking Conference (WCNC) [78] (©IEEE 2020) and that of ULAs and URAs with dual-polarized dipoles at the 24th International ITG Workshop on Smart Antennas (WSA 2020) [23].

5.2 Theory

Similarly to [13], we consider a multi-antenna transmitter and a single antenna receiver, and do not use the unilateral approximation, because the currents in the receive antennas do influence the transmit antennas, so that the near field is important to the analysis. See [8, 9], for more details on the unilateral approximation. In addition, we also consider the reverse link with a single antenna transmitter and a multi-antenna receiver.

Consider the circuit model for a setup with N transmit and M receive antennas, see Fig. 5.1, which additionally models losses in the antennas compared to Fig. 2.2. Power matching is employed at the transmitter, i.e.,

$$Z_{\mathrm{G}} = Z_{\mathrm{A}}^*. \tag{5.1}$$

Let

$$\boldsymbol{Z}_{11,\mathrm{r}} = \boldsymbol{Z}_{11} + \gamma R_{\mathrm{r}} \boldsymbol{I}, \quad \boldsymbol{Z}_{22,\mathrm{r}} = \boldsymbol{Z}_{22} + \gamma R_{\mathrm{r}} \boldsymbol{I}, \tag{5.2}$$

where the dissipation resistance γR_{r}, which is connected in series, is used to model the losses in the antennas, see Fig. 5.1. The impedance matrices seen at the input and the output are

$$\boldsymbol{Z}_{\mathrm{in}} = \boldsymbol{Z}_{11,\mathrm{r}} - \boldsymbol{Z}_{12}(Z_{\mathrm{L}}\boldsymbol{I} + \boldsymbol{Z}_{22,\mathrm{r}})^{-1}\boldsymbol{Z}_{21}, \tag{5.3}$$

$$\boldsymbol{Z}_{\mathrm{out}} = \boldsymbol{Z}_{22,\mathrm{r}} - \boldsymbol{Z}_{21}(Z_{\mathrm{G}}\boldsymbol{I} + \boldsymbol{Z}_{11,\mathrm{r}})^{-1}\boldsymbol{Z}_{12}. \tag{5.4}$$

The communication system in Fig. 5.1 can then be described using the physical model, which is based on [13] and (2.17), but where the following matrices are redefined compared to Section 2.2.1 to take into account the losses:

$$\boldsymbol{R}_\eta = \frac{|Z_{\mathrm{L}}|^2}{R_{\mathrm{L}}}(\boldsymbol{Z}_{\mathrm{out}} + Z_{\mathrm{L}}\boldsymbol{I})^{-1}\boldsymbol{Q}(\boldsymbol{Z}_{\mathrm{out}} + Z_{\mathrm{L}}\boldsymbol{I})^{-H} \tag{5.5}$$

$$\boldsymbol{B} = R_{\mathrm{G}}(\boldsymbol{Z}_{\mathrm{in}} + Z_{\mathrm{G}}\boldsymbol{I})^{-H}\,\mathrm{Re}(\boldsymbol{Z}_{\mathrm{in}})(\boldsymbol{Z}_{\mathrm{in}} + Z_{\mathrm{G}}\boldsymbol{I})^{-1}, \tag{5.6}$$

$$\boldsymbol{D} = Z_{\mathrm{L}}(\boldsymbol{Z}_{22} + Z_{\mathrm{L}}\boldsymbol{I})^{-1}\boldsymbol{Z}_{21}(\boldsymbol{Z}_{\mathrm{in}} + Z_{\mathrm{G}}\boldsymbol{I})^{-1}, \tag{5.7}$$

$$\boldsymbol{Q} = \sigma_u^2\boldsymbol{I} + \sigma_i^2\boldsymbol{Z}_{\mathrm{out}}\boldsymbol{Z}_{\mathrm{out}}^H - 2\sigma_u\sigma_i\,\mathrm{Re}(\rho^*\boldsymbol{Z}_{\mathrm{out}}) + \boldsymbol{R}_{\mathrm{A}}, \tag{5.8}$$

$$\boldsymbol{R}_{\mathrm{A}} = 4k_{\mathrm{B}}T_{\mathrm{A}}\Delta f\,\mathrm{Re}(\boldsymbol{Z}_{\mathrm{out}}). \tag{5.9}$$

The corresponding information-theoretic model is the same as in (2.18), but the specific $\boldsymbol{B}^{1/2}$ and $\boldsymbol{R}_\eta^{1/2}$ to transform between the physical model (2.17) and the model (2.18) analogously to (2.21)

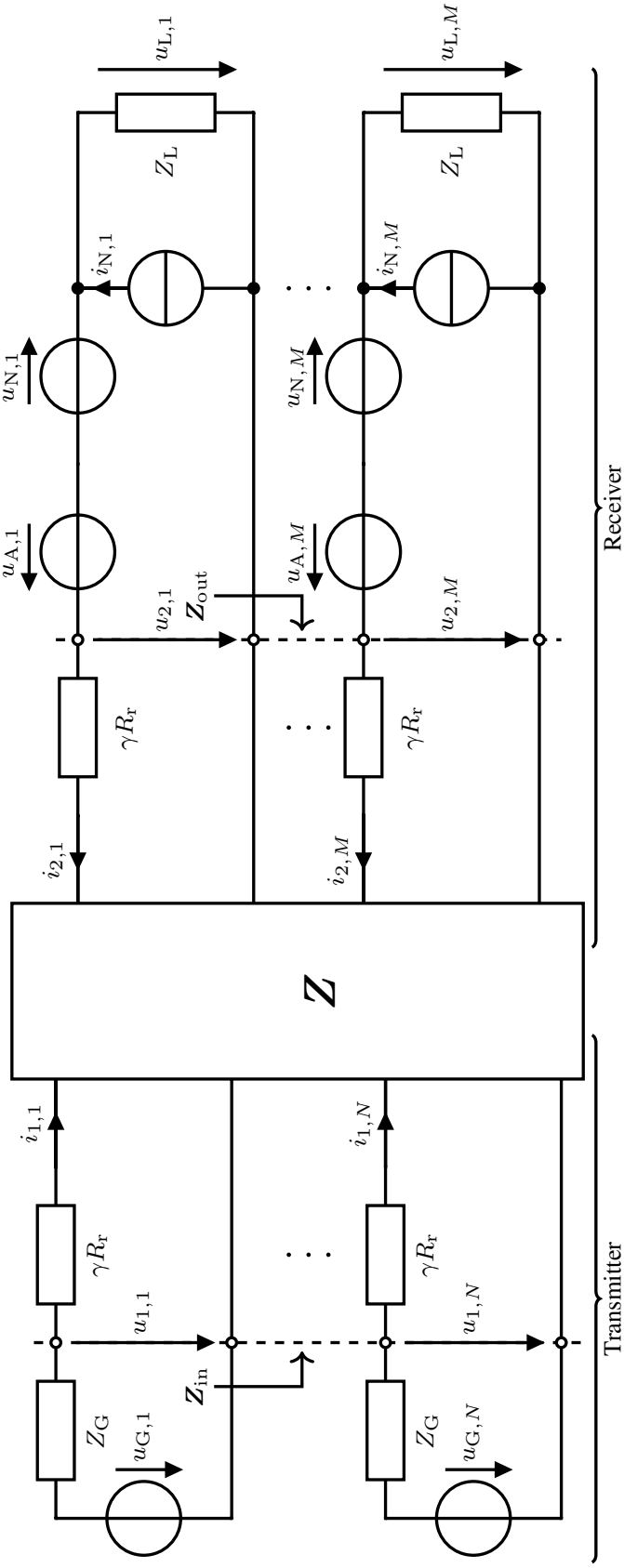

Fig. 5.1. Circuit model with losses in the antennas (modified from [21]) [78]. (©IEEE 2020)

and (2.22), need to be redefined as well,

$$\boldsymbol{B}^{1/2} = \sqrt{R_{\mathrm{G}}}(\boldsymbol{Z}_{\mathrm{in}} + Z_{\mathrm{G}}\boldsymbol{I})^{-H}\,\mathrm{Re}(\boldsymbol{Z}_{\mathrm{in}})^{1/2} \quad \text{s.t.} \quad \mathrm{Re}(\boldsymbol{Z}_{\mathrm{in}}) = \mathrm{Re}(\boldsymbol{Z}_{\mathrm{in}})^{1/2}\,\mathrm{Re}(\boldsymbol{Z}_{\mathrm{in}})^{1/2}, \tag{5.10}$$

$$\boldsymbol{R}_{\eta}^{1/2} = \frac{Z_{\mathrm{L}}}{\sqrt{R_{\mathrm{L}}}}(\boldsymbol{Z}_{\mathrm{out}} + Z_{\mathrm{L}}\boldsymbol{I})^{-1}\boldsymbol{Q}^{1/2}. \tag{5.11}$$

This gives the information theoretic channel

$$\boldsymbol{H} = \sigma_{\vartheta}\boldsymbol{Q}^{-1/2}\boldsymbol{Z}_{21,\mathrm{eff}}\,\mathrm{Re}(\boldsymbol{Z}_{\mathrm{in}})^{-1/2}, \tag{5.12}$$

$$\boldsymbol{Z}_{21,\mathrm{eff}} = \boldsymbol{Z}_{21} - \boldsymbol{Z}_{21}(Z_{\mathrm{G}}\boldsymbol{I} + \boldsymbol{Z}_{11,\mathrm{r}})^{-1}\boldsymbol{Z}_{12}(Z_{\mathrm{L}}\boldsymbol{I} + \boldsymbol{Z}_{22,\mathrm{r}})^{-1}\boldsymbol{Z}_{21}, \tag{5.13}$$

where $\boldsymbol{Z}_{21,\mathrm{eff}}$ is the effective mutual impedance matrix between transmitter and receiver.

5.2.1 Receive Array Gain

For the receive array gain, we consider an uplink scenario with a mobile with one antenna transmitting to a base station with N_{BS} antennas, i.e., $N = 1, M = N_{\mathrm{BS}}$. This implies that $\boldsymbol{H}$ becomes a vector $\boldsymbol{h} \coloneqq \boldsymbol{H}$ and similarly $\boldsymbol{z}_{21,\mathrm{eff}} \coloneqq \boldsymbol{Z}_{21,\mathrm{eff}}$ and $Z_{\mathrm{in}} \coloneqq \boldsymbol{Z}_{\mathrm{in}}$. The receive array gain is defined as [8]

$$A_{\mathrm{Rx}} \coloneqq \left.\frac{\max \mathrm{SNR}}{\mathrm{SNR}|_{M=1,\gamma=0}}\right|_{P_{\mathrm{T}}=\mathrm{const.}}, \tag{5.14}$$

where

$$\max \mathrm{SNR} = \frac{\|\boldsymbol{h}\|_2^2}{\sigma_{\vartheta}^2}P_{\mathrm{T}} = \frac{\boldsymbol{z}_{21,\mathrm{eff}}^H\boldsymbol{Q}^{-1}\boldsymbol{z}_{21,\mathrm{eff}}}{\mathrm{Re}(Z_{\mathrm{in}})}P_{\mathrm{T}} \tag{5.15}$$

is obtained by use of a matched filter at the receiver and the SNR for $M = 1$ lossless receive antennas is obtained in a similar way. Then

$$A_{\mathrm{Rx}} = \frac{\mathrm{Re}(Z_{\mathrm{in},0})}{\mathrm{Re}(Z_{\mathrm{in}})}\frac{\boldsymbol{z}_{21,\mathrm{eff}}^H\boldsymbol{Q}^{-1}\boldsymbol{z}_{21,\mathrm{eff}}\sigma_{q,0}^2}{|z_{21,\mathrm{eff},0}|^2}, \tag{5.16}$$

where

$$Z_{\mathrm{in},0} \coloneqq \boldsymbol{Z}_{\mathrm{in}}|_{M=1,\gamma=0}, \qquad \sigma_{q,0}^2 \coloneqq \boldsymbol{Q}|_{M=1,\gamma=0}, \qquad z_{21,\mathrm{eff},0} \coloneqq \boldsymbol{z}_{21,\mathrm{eff}}|_{M=1,\gamma=0}. \tag{5.17}$$

5.2.2 Transmit Array Gain

For the transmit array gain, we consider a downlink scenario with a base station with N_{BS} antennas transmitting to a mobile with one antenna, i.e., $N = N_{\mathrm{BS}}, M = 1$. Here, $\boldsymbol{h} \coloneqq \boldsymbol{H}^T$ and $\boldsymbol{z}_{21,\mathrm{eff}} \coloneqq \boldsymbol{Z}_{21,\mathrm{eff}}^T$ to make them column vectors and $\boldsymbol{Q}$ becomes a scalar σ_q^2. The transmit array gain is defined as [8]

$$A_{\mathrm{Tx}} \coloneqq \left.\frac{\max \mathrm{SNR}}{\mathrm{SNR}|_{N=1,\gamma=0}}\right|_{P_{\mathrm{T}}=\mathrm{const.}}, \tag{5.18}$$

where

$$\max \mathrm{SNR} = \frac{\|\boldsymbol{h}\|_2^2}{\sigma_{\vartheta}^2}P_{\mathrm{T}} = \frac{\boldsymbol{z}_{21,\mathrm{eff}}^H\,\mathrm{Re}(\boldsymbol{Z}_{\mathrm{in}})^{-1}\boldsymbol{z}_{21,\mathrm{eff}}}{\sigma_q^2}P_{\mathrm{T}} \tag{5.19}$$

is obtained by using a matched filter at the transmitter and the SNR for $N = 1$ lossless transmit antennas is obtained in a similar way. Then,

$$A_{\mathrm{Tx}} = \frac{\mathrm{Re}(Z_{\mathrm{in},0})}{\sigma_q^2} \frac{\boldsymbol{z}_{21,\mathrm{eff}}^H \mathrm{Re}(\boldsymbol{Z}_{\mathrm{in}})^{-1} \boldsymbol{z}_{21,\mathrm{eff}} \sigma_{q,0}^2}{|z_{21,\mathrm{eff},0}|^2}, \tag{5.20}$$

where $Z_{\mathrm{in},0}, \sigma_{q,0}^2$ and $z_{21,\mathrm{eff},0}$ are defined as in (5.17), but for $N = 1, \gamma = 0$.

Considering the transmit array gain is equivalent to considering the minimum transmitted energy per bit $E_{\mathrm{b,min}}$ as in [13]. This can be shown as follows: by adding the losses in the antennas to the model in [13] and for the more general noise distribution assumed in this paper,

$$E_{\mathrm{b,min}} = \frac{\sigma_q^2 \ln 2}{\Delta f \boldsymbol{z}_{21,\mathrm{eff}}^H \mathrm{Re}(\boldsymbol{Z}_{\mathrm{in}})^{-1} \boldsymbol{z}_{21,\mathrm{eff}}}. \tag{5.21}$$

This means

$$A_{\mathrm{Tx}} \propto E_{\mathrm{b,min}}^{-1}. \tag{5.22}$$

Note that transmitting with $E_{\mathrm{b,min}}$ leads to the well-known minimum received energy per bit $\sigma_\vartheta^2 \ln(2)/(\Delta f)$, see [79].

5.2.3 Channel for a Single Polarization

In Sections 5.3 and 5.4, we assume that all antennas at the base station and the mobile are parallel infinitely thin but lossless $\lambda/2$-dipoles in series with the dissipation resistance γR_{r}. Then for an LOS channel, the entries of $\boldsymbol{Z}$ can be computed according to the analytical formulas using the sinusoidal current approximation, see Section 2.4, including $\boldsymbol{z}_{21}$.

However, for a receiver located in the far field in direction (θ, φ), where θ and φ are the zenith and azimuth angles of the usual spherical coordinate system, see Fig. 5.2,

$$\boldsymbol{z}_{21} = R_{\mathrm{r}} \boldsymbol{a}(\theta, \varphi), \tag{5.23}$$

where $\boldsymbol{a}(\theta, \varphi)$ is the steering vector pointing into direction (θ, φ), i.e.,

$$a_n(\theta, \varphi) = e^{-j\frac{2\pi}{\lambda} \boldsymbol{r}_n^T \boldsymbol{r}}, \quad \boldsymbol{r} = \begin{bmatrix} \cos(\varphi)\sin(\theta) \\ \sin(\varphi)\sin(\theta) \\ \cos(\theta) \end{bmatrix}, \tag{5.24}$$

and $\boldsymbol{r}_n$ is the position vector of the n-th antenna, see e.g., [80]. We choose the coordinate system such that the origin coincides with the center of the array. The $\lambda/2$-dipoles are oriented parallel to $\theta = 0$, the ULAs are oriented such that they lie in $\varphi = \pi/2$ and the UCAs are oriented such that one antenna lies in $\varphi = 0$.

Extending the consideration to the far field,

$$\begin{aligned} Z_{\mathrm{in},0} \to Z_{\mathrm{A}}, \quad \boldsymbol{z}_{21,\mathrm{eff}} \to \boldsymbol{z}_{21}, \quad \boldsymbol{Z}_{\mathrm{in}} \to \boldsymbol{Z}_{11,\mathrm{r}}, \\ \sigma_q^2 \to \sigma_{q,0}^2, \quad z_{21,\mathrm{eff},0} \to z_{21,0}, \quad \boldsymbol{Z}_{\mathrm{out}} \to \boldsymbol{Z}_{22,\mathrm{r}}, \end{aligned} \tag{5.25}$$

where $\boldsymbol{z}_{21}$ and $z_{21,0}$ are defined analogously to $\boldsymbol{z}_{21,\mathrm{eff}}$ and $z_{21,\mathrm{eff},0}$. That means, A_{Tx} in the far field is [8]

$$A_{\mathrm{Tx}} = R_{\mathrm{r}} \frac{\boldsymbol{z}_{21}^H \mathrm{Re}(\boldsymbol{Z}_{11,\mathrm{r}})^{-1} \boldsymbol{z}_{21}}{|z_{21,0}|^2}. \tag{5.26}$$

Different arrays vary in $\mathrm{Re}(\boldsymbol{Z}_{11,\mathrm{r}})$ and in $\boldsymbol{a}(\theta, \varphi)$. The former is Toeplitz for ULAs and circulant for UCAs.

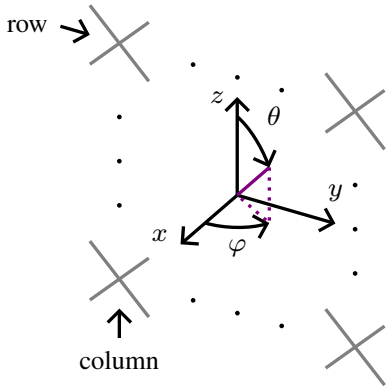

Fig. 5.2. URA lying in the yz-plane in the coordinate system [23].

5.2.4 Extension to Dual-Polarized Arrays

For arrays with dual-polarized antennas, consider the transmit gain for vertically and horizontally polarized receivers, $G_{\mathrm{V,Tx}}$ and $G_{\mathrm{H,Tx}}$, with the corresponding $\boldsymbol{z}_{\mathrm{V},21}$ and $\boldsymbol{z}_{\mathrm{H},21}$. They are defined as

$$G_{\mathrm{V/H,Tx}} \coloneqq \left.\frac{\max \mathrm{SNR}}{\mathrm{SNR}|_{N=1,\gamma=0,\mathrm{iso}}}\right|_{P_{\mathrm{T}}=\mathrm{const.}} = R_{\mathrm{r}} \frac{\boldsymbol{z}_{\mathrm{V/H},21}^{H} \operatorname{Re}(\boldsymbol{Z}_{11,\mathrm{r}})^{-1} \boldsymbol{z}_{\mathrm{V/H},21}}{|z_{\mathrm{iso},21,0}|^2}, \tag{5.27}$$

which can be derived using the same steps as for (5.26), but with $\mathrm{SNR}|_{N=1,\gamma=0,\mathrm{iso}}$ being the SNR for a transmitter with a single lossless isotropic radiator matching the receiver's polarization and having the same radiation resistance R_{r} as the dual-polarized antennas. $z_{\mathrm{iso},21,0}$ is the corresponding channel. Furthermore, we need to consider polarization in the steering vectors for a receiver with horizontal and vertical polarization, $\boldsymbol{a}_{\mathrm{H}}(\theta,\varphi)$ and $\boldsymbol{a}_{\mathrm{V}}(\theta,\varphi)$. They are related to $\boldsymbol{z}_{\mathrm{V},21}$ and $\boldsymbol{z}_{\mathrm{H},21}$ similarly as in (5.23). In our coordinate system, the horizontal and vertical polarization at the transmitter can be described using the unit vectors $\boldsymbol{e}_y$ and $\boldsymbol{e}_z$ respectively. Similarly, at the receiver, they are described by $\boldsymbol{e}_\varphi$ and $-\boldsymbol{e}_\theta$.

Let $\boldsymbol{t}_n$ be the tangent vector describing transmit antenna n's polarization and $f_n(\theta,\varphi)$ its radiation pattern. The radiation pattern of $\lambda/2$-dipoles is given in Section 2.4. The steering vectors' entries are

$$a_{\mathrm{H},n}(\theta,\varphi) = e^{-j\frac{2\pi}{\lambda}\boldsymbol{r}_n^T\boldsymbol{r}} f_n(\theta,\varphi)\boldsymbol{t}_n^T\boldsymbol{e}_\varphi(\theta,\varphi), \tag{5.28}$$

$$a_{\mathrm{V},n}(\theta,\varphi) = -e^{-j\frac{2\pi}{\lambda}\boldsymbol{r}_n^T\boldsymbol{r}} f_n(\theta,\varphi)\boldsymbol{t}_n^T\boldsymbol{e}_\theta(\theta,\varphi). \tag{5.29}$$

In Section 5.5, we assume that the antennas at the base station are N_{BS} dual-polarized crossed $\lambda/2$-dipoles, where $N = 2N_{\mathrm{BS}}$. $\boldsymbol{Z}_{11}$ can be computed according to the sinusoidal current approximation: the off-diagonal elements using the formulas in Section 2.5, and the elements on the diagonal are the self-impedance of $\lambda/2$-dipoles, see Section 2.4.

5.3 Numerical Results with Parallel λ/2-dipoles

Consider the distance d_{bm} between the base station and the mobile, see Fig. 5.3. In the following section,

$$d_{\mathrm{bm}} \in \{10^{i/2}\lambda \mid i = 4,\ldots,8\}. \tag{5.30}$$

Table 5.1 shows the value of these distances for the following frequency bands:

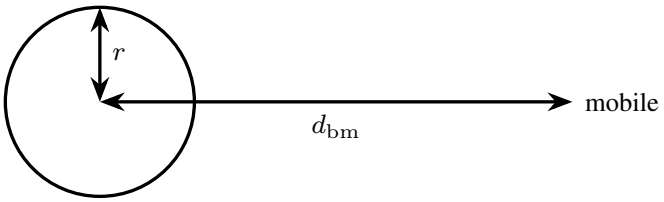

(a) UCA with fixed radius.

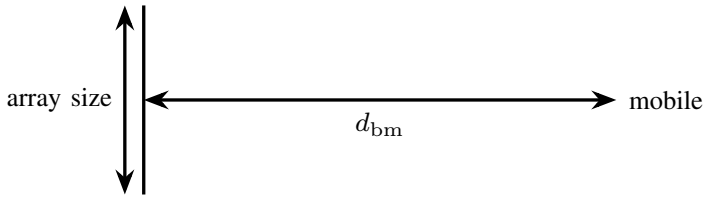

(b) ULA transmitting into frontfire direction.

Fig. 5.3. Scenarios [78]. (©IEEE 2020)

Table 5.1. Overview of the distances between the base station and the mobile at the different frequencies [78]. (©IEEE 2020)

d_{bm}	@ $f_c = 680.5\,\mathrm{MHz}$ (n71 uplink)	@ $f_c = 3.55\,\mathrm{GHz}$ (n78)	@ $f_c = 27.925\,\mathrm{GHz}$ (n261)
$10^2\lambda$	44.1 m	8.44 m	1.07 m
$10^{2.5}\lambda$	139 m	26.7 m	3.39 m
$10^3\lambda$	441 m	84.4 m	10.7 m
$10^{3.5}\lambda$	1.39 km	267 m	33.9 m
$10^4\lambda$	4.41 km	844 m	107 m

Table 5.2. Overview of 3GPP 38.901 channel model parameters [78]. (©IEEE 2020)

	RMa	UMa	UMi
Base station altitude	35 m	25 m	10 m
Mobile altitude	1.5 m	between 1.5 m and 22.5 m	
Minimum horizontal distance	35 m		10 m
Inter site distance	5000 m	500 m	200 m
⇒ Minimum distance	48.4 m	35.1 m	10.0 m
⇒ Maximum distance	2.89 km	290 m	116 m

- The uplink in LTE (5G NR) band 71 (n71), which spans $663\,\mathrm{MHz}$ to $698\,\mathrm{MHz}$ [81, 82], i.e., $f_\mathrm{c} = 680.5\,\mathrm{MHz}$, which is one of the lowest frequency bands currently supported for mobile broadband.
- Band n78, from $3.3\,\mathrm{GHz}$ to $3.8\,\mathrm{GHz}$ [82], i.e., $f_\mathrm{c} = 3.55\,\mathrm{GHz}$.
- 5G NR mmWave band n261, which spans $27.5\,\mathrm{GHz}$ to $28.35\,\mathrm{GHz}$ [83], i.e. $f_\mathrm{c} = 27.925\,\mathrm{GHz}$.

All three bands are among the first for 5G NR deployment.

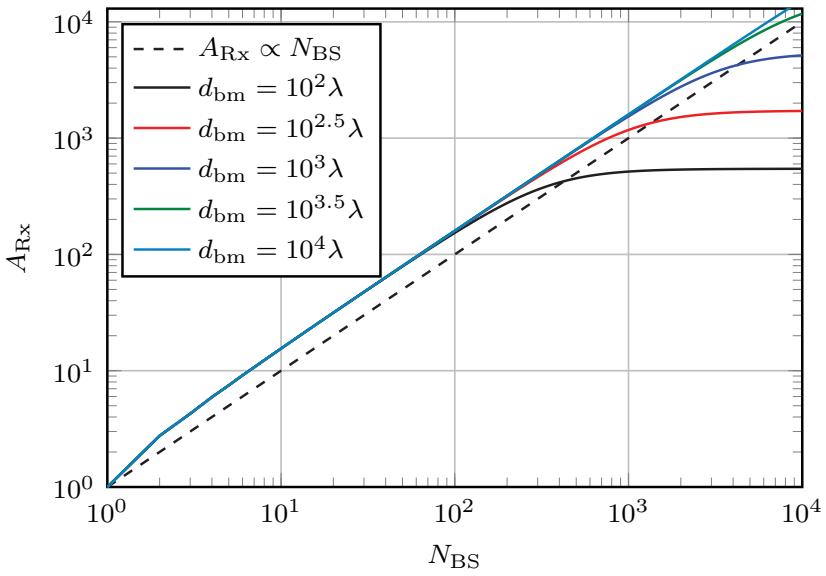

Fig. 5.4. A_{Rx} for a ULA in frontfire with fixed antenna separation $d = \lambda/2$ [78]. (©IEEE 2020)

Let us compare these distances to the ones in the 3GPP 38.901 channel model [12]. For band n71, consider the rural macro (RMa), for band n78 the UMa and for band n261 the urban micro (UMi) scenario. The base station altitude, mobile height, minimum 2D distance and inter site distance are as shown in Table 5.2. According to these parameters, a d_{bm} between 100λ and 10000λ almost entirely covers the various scenarios. In the remainder of this section, the various frequency bands will be analyzed jointly with all distances normalized to λ.

In this section, we consider A_{Rx} and A_{Tx} according to (5.16) and (5.20) for reception and transmission from and to frontfire direction ($\theta = \pi/2, \varphi = 0$). We use the measured noise parameters from [66, Tables IV & VI], i.e., in particular $Z_{\mathrm{L}} = (186 - 31.6\mathrm{j})\,\Omega$, and assume that the loss factor $\gamma = 10^{-3}$.

5.3.1 Fixed Distance

Consider a ULA with a fixed antenna separation $d = \lambda/2$ and between $N_{\mathrm{BS}} = 1$ and $N_{\mathrm{BS}} = 10000$ base station antennas transmitting into the frontfire direction, see Fig. 5.3b. A_{Rx} and A_{Tx} for this scenario are shown in Figs. 5.4 and 5.5. They are almost identical here. According to conventionally modeled systems, which neglect mutual coupling, we expect

$$A_{\mathrm{Rx}} = N_{\mathrm{BS}}, \qquad A_{\mathrm{Tx}} = N_{\mathrm{BS}}. \tag{5.31}$$

However, when N_{BS} increases from 1, the array gain becomes slightly larger than N_{BS}. Furthermore for a larger N_{BS}, the array gain starts to saturate, with saturation occurring at a lower N_{BS} the smaller the d_{bm}. For $d_{\mathrm{bm}} = 100\lambda$, the onset of saturation starts at values as low as $N_{\mathrm{BS}} = 100$ to 300, corresponding to an array size between 49.5λ and 149.5λ, whereas for $d_{\mathrm{bm}} = 10^{3.5}\lambda$ only the very start of the saturation near $N_{\mathrm{BS}} = 10^4$ can be seen and for $d_{\mathrm{bm}} = 10^4$, the array gain only saturates for an even larger value of N_{BS}. When we compare the array size at which saturation starts to d_{bm}, we can see that the array size there is on the same order of magnitude as d_{bm}. This indicates that saturation occurs as the additional antennas' path-loss increases so they contribute less. For typical cellular systems, whose array size is significantly smaller than the distance between the base station and the mobile, this is not a practical limitation.

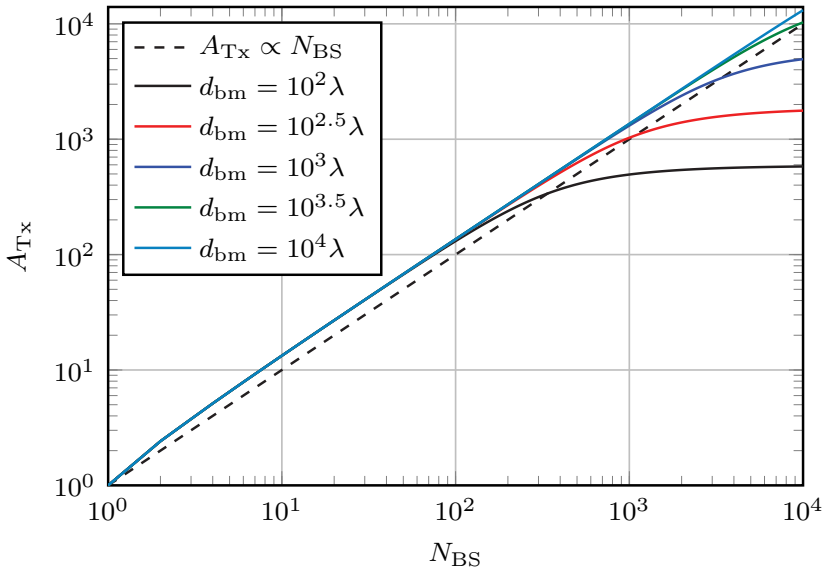

Fig. 5.5. A_{Tx} for a ULA in frontfire with fixed antenna separation $d = \lambda/2$ [78]. (©IEEE 2020)

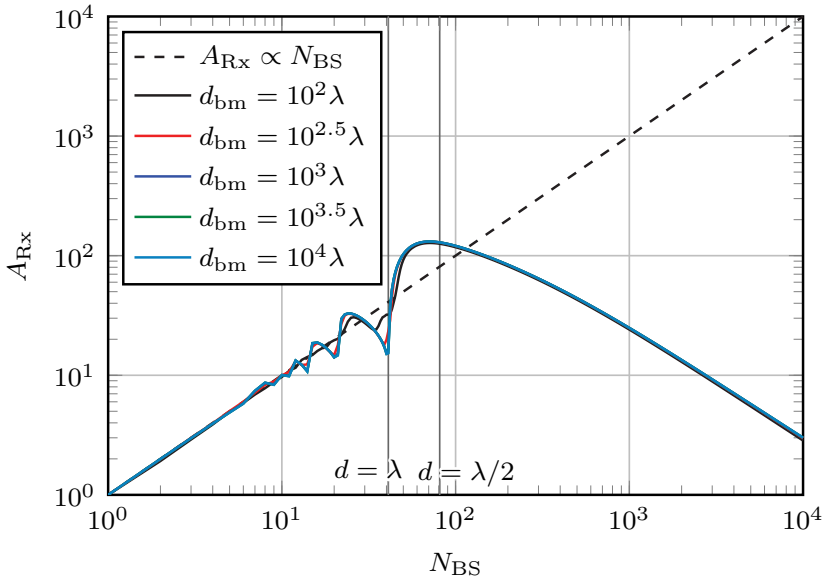

Fig. 5.6. A_{Rx} for a ULA in frontfire with a fixed array size of 40λ [78]. (©IEEE 2020)

5.3.2 Fixed Radius

Consider a ULA with array size 40λ and a UCA with radius $r = 20\lambda$, see Fig. 5.3. As N_{BS} increases, the antenna separation d decreases. A_{Rx} and A_{Tx} are shown in Figs. 5.6 to 5.9 for different distances between the base station and the mobile. The curves for the ULA show that even for values slightly greater than $N_{\mathrm{BS}} = 10$ antennas, A_{Rx} and A_{Tx} deviate from the linear increase expected from conventionally modeled systems, see (5.31). For the UCA, for $d > 1.26\lambda$ (corresponding to $N_{\mathrm{BS}} \leq 100$), (5.31) holds approximately. Technically there is a small gap to N_{BS} in the array gain when the receiver is close to the base station, see the curve for $d_{\mathrm{bm}} = 100\lambda$.

However for smaller distances between the antennas, the trend for A_{Rx} and A_{Tx} is different. Considering the former, for the ULA there is a maximum at about 71 antennas ($d \approx 0.571\lambda$) and for the UCA at about 275 antennas ($d \approx 0.457\lambda$), and if the number of base station antennas is

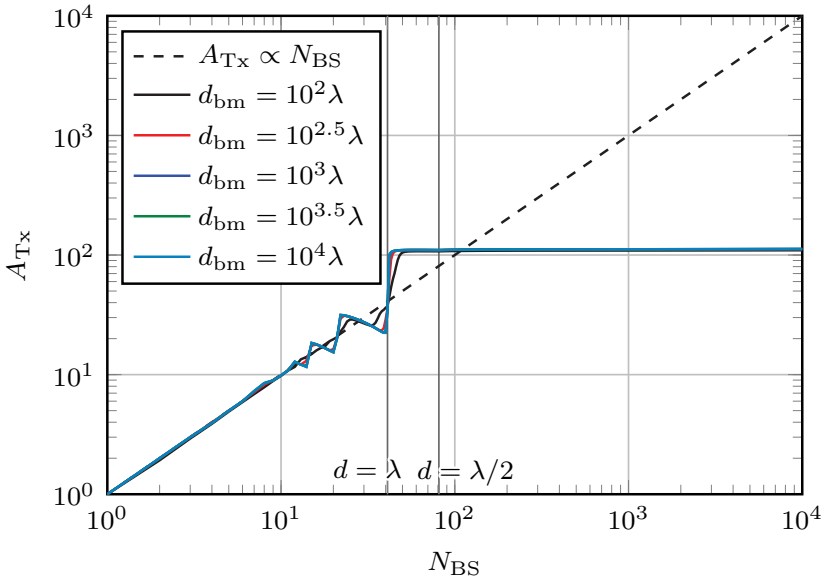

Fig. 5.7. A_{Tx} for a ULA in frontfire with a fixed array size of 40λ [78]. (©IEEE 2020)

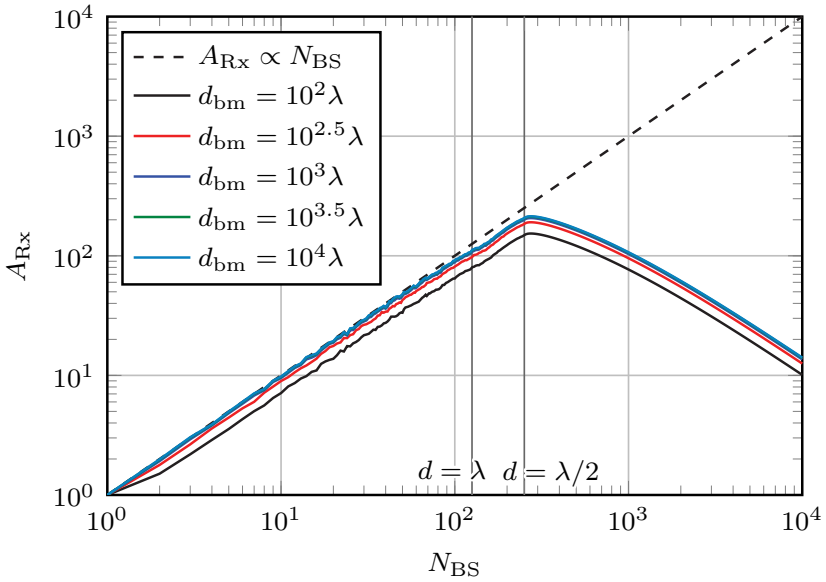

Fig. 5.8. A_{Rx} for a UCA with fixed radius $r = 20\lambda$ [78]. (©IEEE 2020)

increased further, A_{Rx} decreases. Considering A_{Tx}, it (almost) saturates at about 68 antennas for the ULA and 275 antennas for the UCA. If the number of base station antennas is increased further, A_{Tx} only increases slightly. Notably, the number of antennas for which the maximum A_{Rx} is obtained, and for which A_{Tx} starts to saturate, is (almost) independent of the distance to the mobile. There is a saturation, as the achievable array gain for a certain array size is bounded. The sharp increase in array gain for the ULA at about $d = \lambda$ can be explained by an increasing number of antennas, and a decreasing antenna separation at the same time, compared to [8].

In Fig. 5.10, the receive array gain for the UCA is shown for the case when there is only the noise of the antennas, i.e., $\sigma_u = 0\,\mathrm{V}, \sigma_i = 0\,\mathrm{A}$. In this case, the curves for A_{Rx} are (almost) the same as the curves for A_{Tx} in Fig. 5.9, i.e., the coupling of the noise of the LNA and other analog components between the receive chain causes the decrease in A_{Rx}.

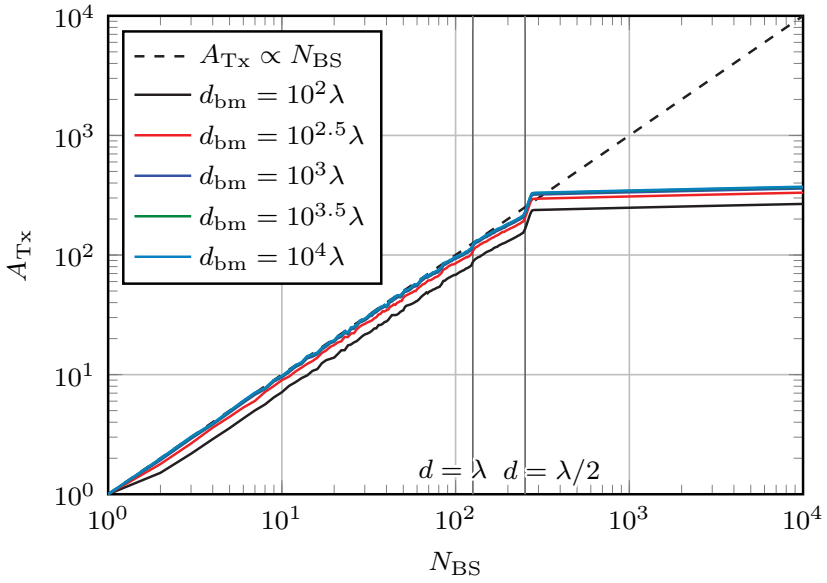

Fig. 5.9. A_{Tx} for a UCA with fixed radius $r = 20\lambda$ [78]. (©IEEE 2020)

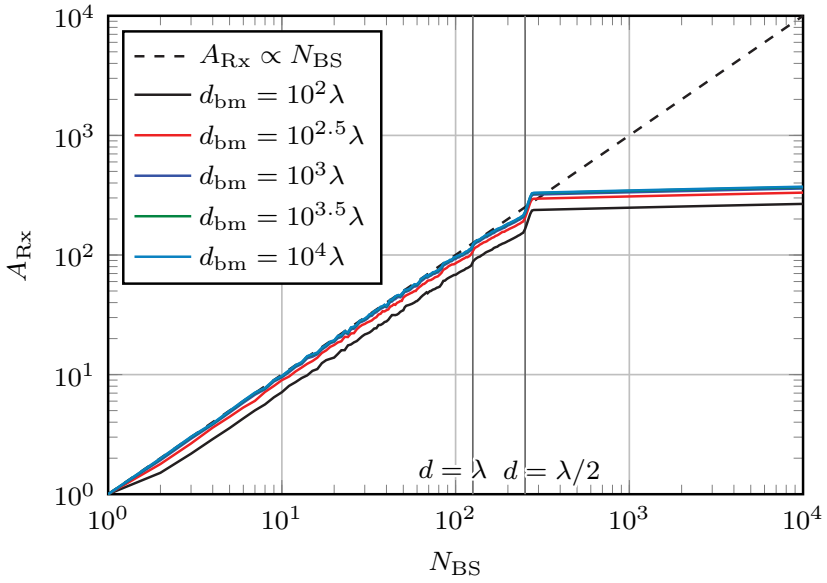

Fig. 5.10. A_{Rx} for a UCA with fixed radius $r = 20\lambda$, antenna noise only [78]. (©IEEE 2020)

5.4 Numerical Results for the Array Gain in the Far Field

In this section, we consider the transmit array gain in the far field for $\theta = \pi/2$, see (5.26), for ULAs and UCAs with various sizes and numbers of antennas N_{BS}. Firstly, consider the ULA in three scenarios: beamforming into the endfire ($\varphi = 90°$), into the $\varphi = 60°$ and into the frontfire direction ($\varphi = 0°$), see Figs. 5.11 to 5.13. The cut for frontfire direction with an array size of 40λ corresponds to Fig. 5.7 with $d_{\mathrm{bm}} \to \infty\lambda$. We can see that A_{Tx} depends on which directions the beamforming vector points to. Consider a fixed antenna array size. Then for the frontfire direction, saturation starts slightly below $d = \lambda$, but for the $60°$ direction, saturation only starts slightly below $d = 0.54\lambda$ and for the endfire direction saturation starts slightly below $d = \lambda/2$. Further, we can observe that the larger the N_{BS}, the closer the saturation starts to $d = \lambda, d \approx 0.54\lambda$ and $d = \lambda/2$ respectively.

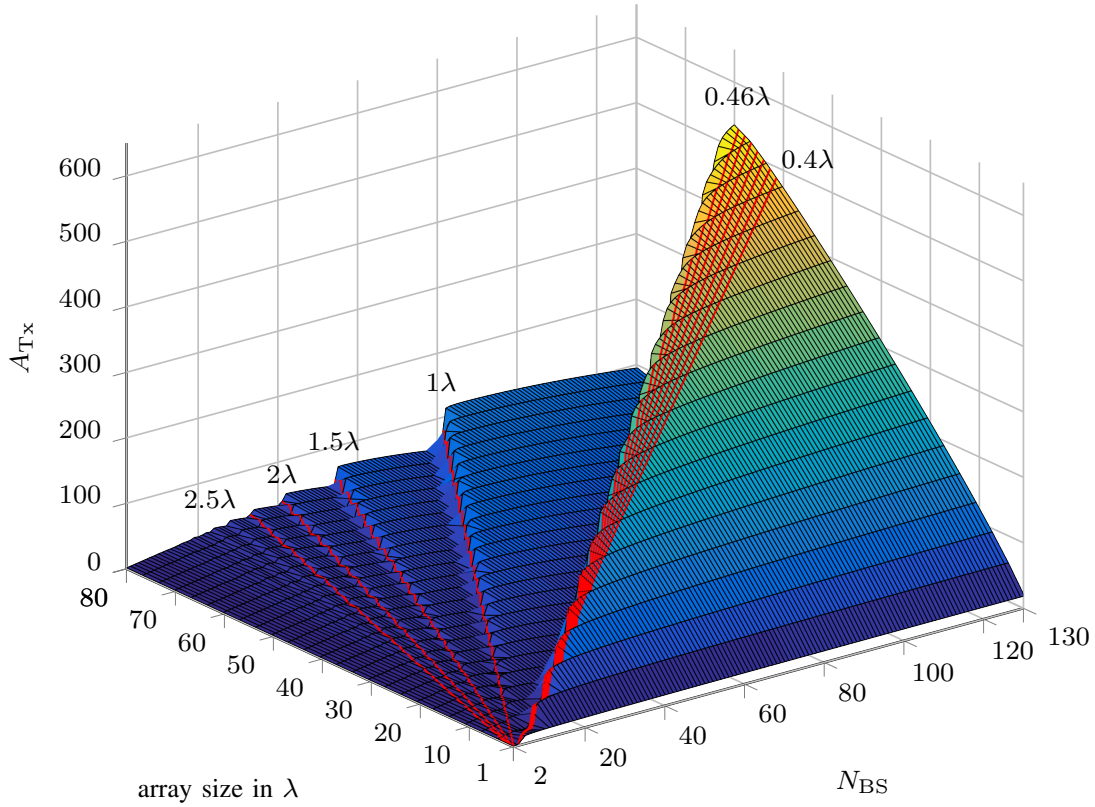

Fig. 5.11. A_{Tx} for a ULA transmitting into endfire direction ($\varphi = 90°$), where the lines for $d = 0.4\lambda$ to 0.46λ are in 0.01λ increments [78]. (©IEEE 2020)

To maximize A_{Tx} the array should be positioned so that its endfire direction points to the angle of interest. If this is not possible, to optimize A_{Tx} for angles $-\varphi_0 \leq \varphi \leq \varphi_0$, where φ_0 is the maximum angle of interest that the array is transmitting to, N_{BS} should be chosen such that d is at a peak for $\varphi = \varphi_0$. The maximum peak is slightly below $d = \lambda/2$ to $d = \lambda$ depending on φ_0 – unless the loss factor γ is too large. On the one hand, if N_{BS} is chosen to be slightly smaller, A_{Tx} falls into a valley for $|\varphi|$ close to φ_0. On the other hand, N_{BS} is chosen to be slightly larger, either A_{Tx} only increases slightly for $d < \lambda/2$ and A_{Tx} becomes more sensitive to tolerances in the position of the antennas in the array, or A_{Tx} decreases again ($d > \lambda/2$).

Secondly, consider a UCA with beamforming into a direction that lies on the line between an antenna and the center of the array (w.l.o.g. $\varphi = 0$), see Fig. 5.14. Here, similarly the cut for an array size of 40λ corresponds to Fig. 5.9 with $d_{\mathrm{bm}} \to \infty\lambda$. Similarly to the ULA transmitting into the endfire direction, A_{Tx} starts to saturate close to $d = \lambda/2$. The UCA behaves differently to the ULA. For transmission into the plane of the UCA, A_{Tx} is independent of φ for an odd N_{BS}, while for an even N_{BS} it only oscillates slightly with φ. Therefore, for maximum A_{Tx}, N_{BS} should be chosen such that A_{Tx} is at the largest peak, i.e., the peak near $d = \lambda/2$, unless γ is too large; then the peak of A_{Tx} near $d = \lambda$ is the largest.

According to the expectation from conventionally modeled systems, (5.31) should hold, but for the ULA there are significantly larger maximum transmit array gains for front- and especially endfire ($A_{\mathrm{Tx}} \approx 219$ and 533 for $N_{\mathrm{BS}} = 130$), but also smaller maximum transmit array gains as seen for $\varphi = 60°$ ($A_{\mathrm{Tx}} \approx 99$ for $N_{\mathrm{BS}} = 130$). For the UCA, there is not such a large direction-dependent variation, but the maximum is $A_{\mathrm{Tx}} \approx 152$ for $N_{\mathrm{BS}} = 130$.

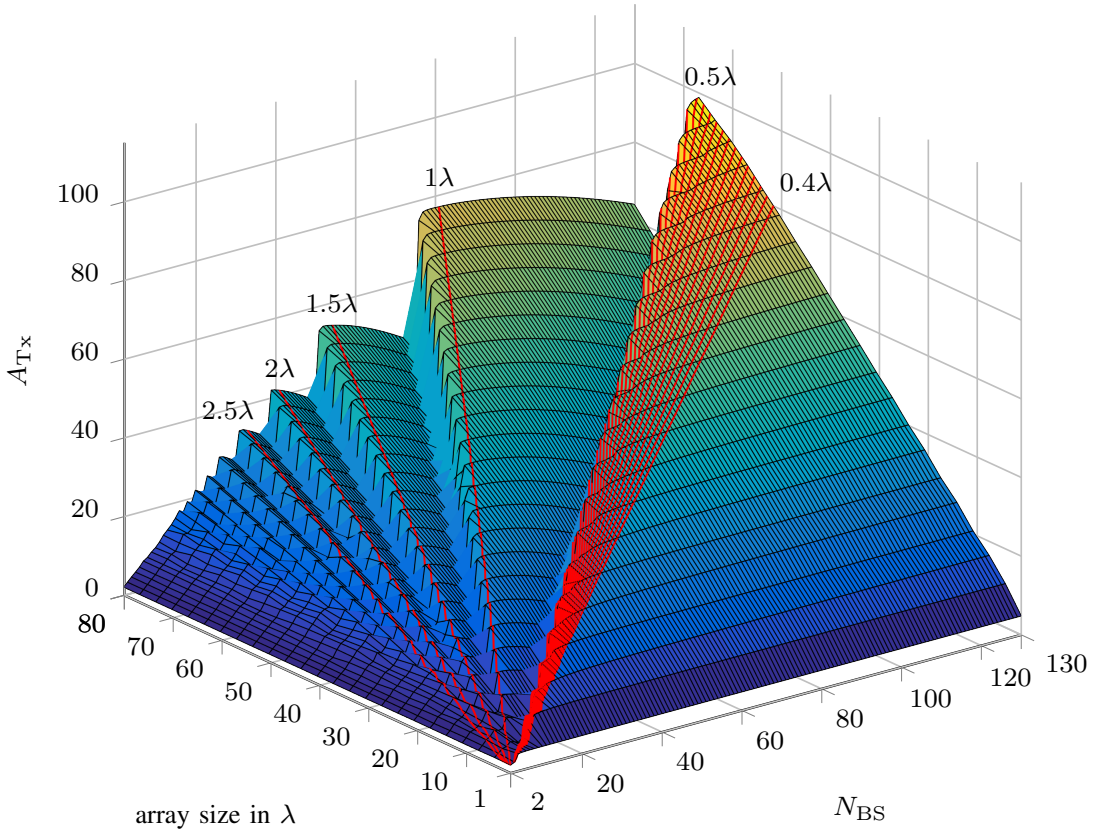

Fig. 5.12. A_{Tx} for a ULA transmitting into $\varphi = 60°$ direction, where the lines for $d = 0.4\lambda$ to 0.5λ are in 0.01λ increments [78]. (©IEEE 2020)

These figures could be used for further evaluations, e.g., whether using a single UCA for a base station deployment rather than non-cooperating ULAs in the typical 3 sectors leads to higher performance, with the same number of antennas in both scenarios.

Consider for example a ULA that should transmit into all azimuth directions, i.e., φ_0 is at its maximum value, $\varphi_0 = 90°$, as the directions with $90° < \varphi \leq 180°$ are covered by symmetry. Based on (5.26), the average transmit array gain over all azimuth directions is

$$\bar{A}_{\mathrm{Tx}} = \frac{1}{2\pi} \int_{\varphi=0}^{2\pi} A_{\mathrm{Tx}} d\varphi = \frac{R_{\mathrm{r}}}{2\pi |z_{21,0}|^2} \operatorname{tr}\left(\boldsymbol{A} \operatorname{Re}(\boldsymbol{Z}_{11,\mathrm{r}})^{-1} \right), \quad \boldsymbol{A} = \int_{\varphi=0}^{2\pi} \boldsymbol{z}_{21} \boldsymbol{z}_{21}^H d\varphi. \tag{5.32}$$

For the ULA, the entries of $\boldsymbol{A}$ are given by

$$A_{ki} = \int_{\varphi=0}^{2\pi} \exp\left(-j \frac{2\pi}{\lambda} |k-i| d \sin(\varphi) \right) d\varphi = 2\pi J_0\left(\frac{2\pi}{\lambda} |k-i| d \right), \tag{5.33}$$

where $J_0(x)$ is the Bessel function of the first kind with order 0.

Fig 5.15 shows $\bar{A}_{\mathrm{Tx}}$ for a ULA transmitting into all azimuth directions with uniform probability. According to the analysis for transmission into a fixed direction φ, the maximum array gain is expected slightly below $d < \lambda/2$. For $N_{\mathrm{BS}} = 130$, the peak in endfire direction is at about $d = 0.46\lambda$, see Fig. 5.11, whereas for $\bar{A}_{\mathrm{Tx}}$ the maximum is at about $d = 0.49\lambda$. This means that the practical

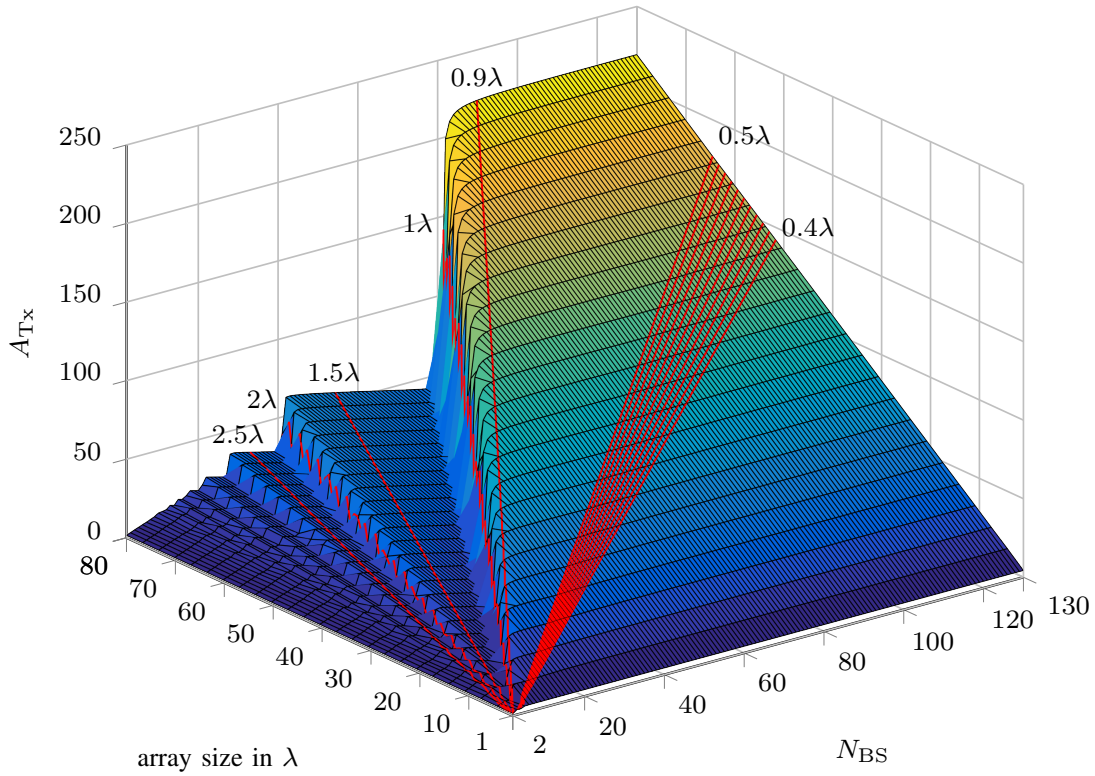

Fig. 5.13. A_{Tx} for a ULA transmitting into frontfire direction ($\varphi = 0°$), where the lines for $d = 0.4\lambda$ to 0.5λ are in 0.01λ increments [78]. (©IEEE 2020)

design recommendation based on looking into the array gain for a single direction provides a good approximation for the average array gain over all azimuth directions. Note that the maximum $\bar{A}_{\mathrm{Tx}}$ is larger than N_{BS} ($\bar{A}_{\mathrm{Tx}} \approx 133.9$ at $N_{\mathrm{BS}} = 130$), although there is a range of azimuth angles for which A_{Tx} is smaller than N_{BS}, for example at $\varphi = 60°$, see Fig. 5.12. This is overcompensated by those ranges of φ, where A_{Tx} is larger and significantly larger than N_{BS}, such that the maximum $\bar{A}_{\mathrm{Tx}}$ is larger than N_{BS}.

5.5 Numerical Results with Dual-Polarized λ/2-dipoles

In this section, we look at a ULA and a URA with $\pm 45°$ dual-polarized crossed $\lambda/2$-dipoles. It is assumed that the URA's center coincides with the origin of the coordinate system and that the URA is oriented such that it lies in the yz-plane, and that its columns are parallel to the z-axis. This means that $\boldsymbol{t}_n = (\boldsymbol{e}_{\mathrm{y}} \pm \boldsymbol{e}_{\mathrm{z}})/\sqrt{2}$. The ULA can also be considered a URA with only a single row. The URA is assumed to be square with identical column and row antenna spacing d. The ULA's array size is $d(N_{\mathrm{BS}} - 1)$, and the square URA's is the length of its diagonal, $\sqrt{2}d(\sqrt{N_{\mathrm{BS}}} - 1)$. Only $d > \lambda/(2\sqrt{2}) + \lambda/100$ is considered to ensure a minimum distance of $\lambda/100$ between the tips of the crossed dipoles, so they do not overlap.

5.5.1 ULA

First, consider the transmit gain for a ULA with dual-polarized dipoles. Fig. 5.16 shows the transmit gain in frontfire direction with a vertically polarized receiver. The maximum $G_{\mathrm{V,Tx}}$ is achieved for d a bit smaller than λ, or smaller. $G_{\mathrm{V,Tx}}$ is roughly $G_{\lambda/2} A_{\mathrm{Tx}}$, where A_{Tx} is computed for the ULA

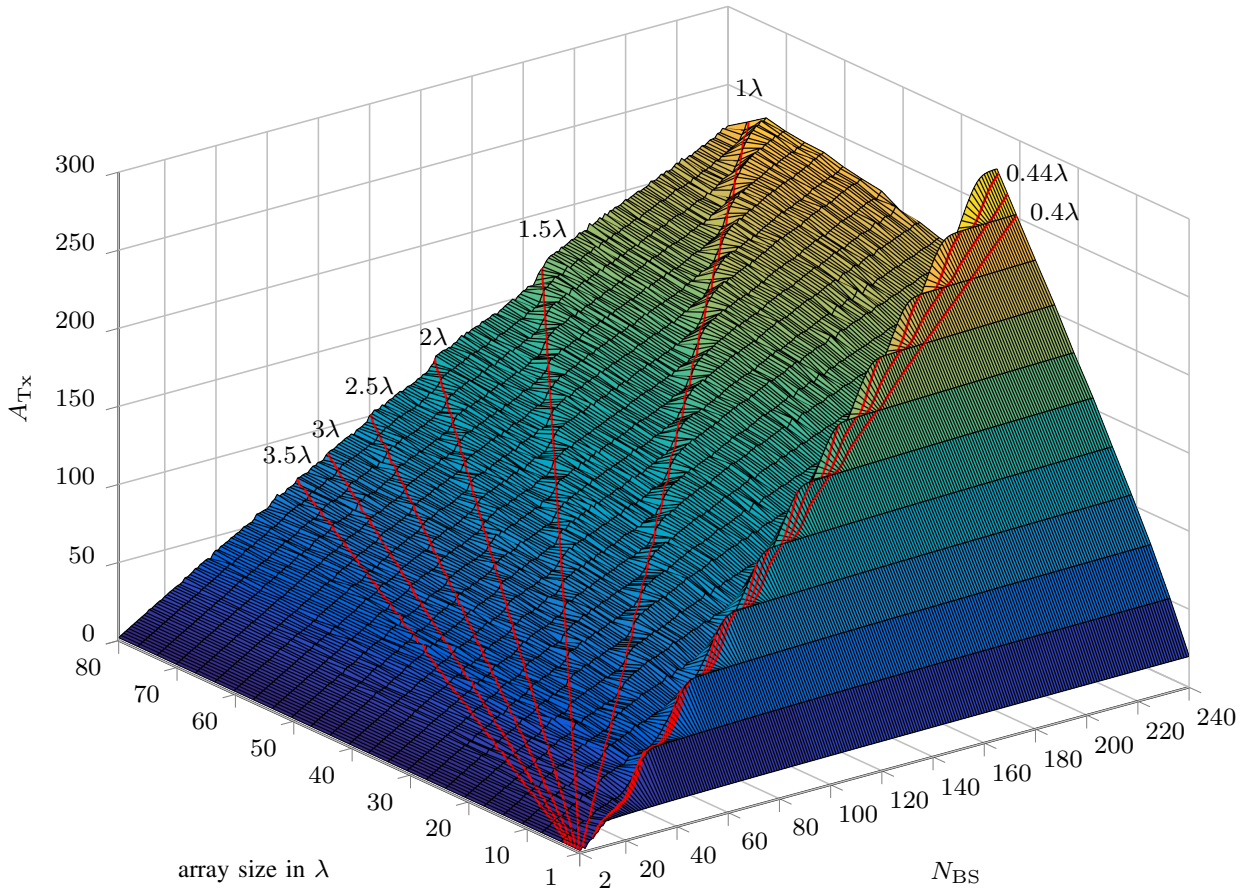

Fig. 5.14. A_{Tx} for a UCA, where the lines for $d = 0.4\lambda$ to 0.44λ are in 0.02λ increments [78]. (©IEEE 2020)

with parallel $\lambda/2$-dipoles in Fig. 5.13, and $G_{\lambda/2}$ is the gain of a single $\lambda/2$-dipole ($G_{\lambda/2} \approx 1.64$, see [36, Ch. 11.5]). When we compare the figures in this section with those in Section 5.4, a pair of dual-polarized $\lambda/2$-dipoles corresponds to one $\lambda/2$-dipole. We can draw the same conclusion here as in Section 5.4 that it is optimal to use an antenna spacing a bit smaller than $d = \lambda$ or smaller for the frontfire direction.

For endfire direction, see Fig. 5.20, there is a peak in $G_{\mathrm{V,Tx}}$ at d a bit smaller than $\lambda/2$: $G_{\mathrm{V,Tx}} \approx 422$ for $N_{\mathrm{BS}} = 130$. This optimum antenna separation is similar as in Section 5.4 with the parallel $\lambda/2$-dipoles. For a horizontally polarized receiver, the transmit gain is zero in endfire direction, as the polarizations are orthogonal in this direction due to the geometry.

5.5.2 URA with a Fixed Number of Antennas

Second, consider the transmit gain of a 5 x 5 URA with $d = \lambda/\sqrt{2}$ over (θ, φ), see Fig. 5.18. For frontfire direction ($\theta = \pi/2, \varphi = 0$), $G_{\mathrm{V,Tx}} = G_{\mathrm{H,Tx}} \approx 72$. This direction is at the maximum of the dipoles' radiation patterns, so if the mutual coupling is ignored,

$$G_{\mathrm{V/H,Tx}} = G_{\lambda/2} N_{\mathrm{BS}} \tag{5.34}$$

is expected, which is about 41 for $N_{\mathrm{BS}} = 25$, but mutual coupling leads to a larger $G_{\mathrm{V,Tx}}$ and $G_{\mathrm{H,Tx}}$. For other directions G_{Tx} mostly decreases, as the direction is not at the maximum of at least half of the dipoles' radiation patterns. Furthermore, as the transmitter's dipoles lie in the yz-plane, they

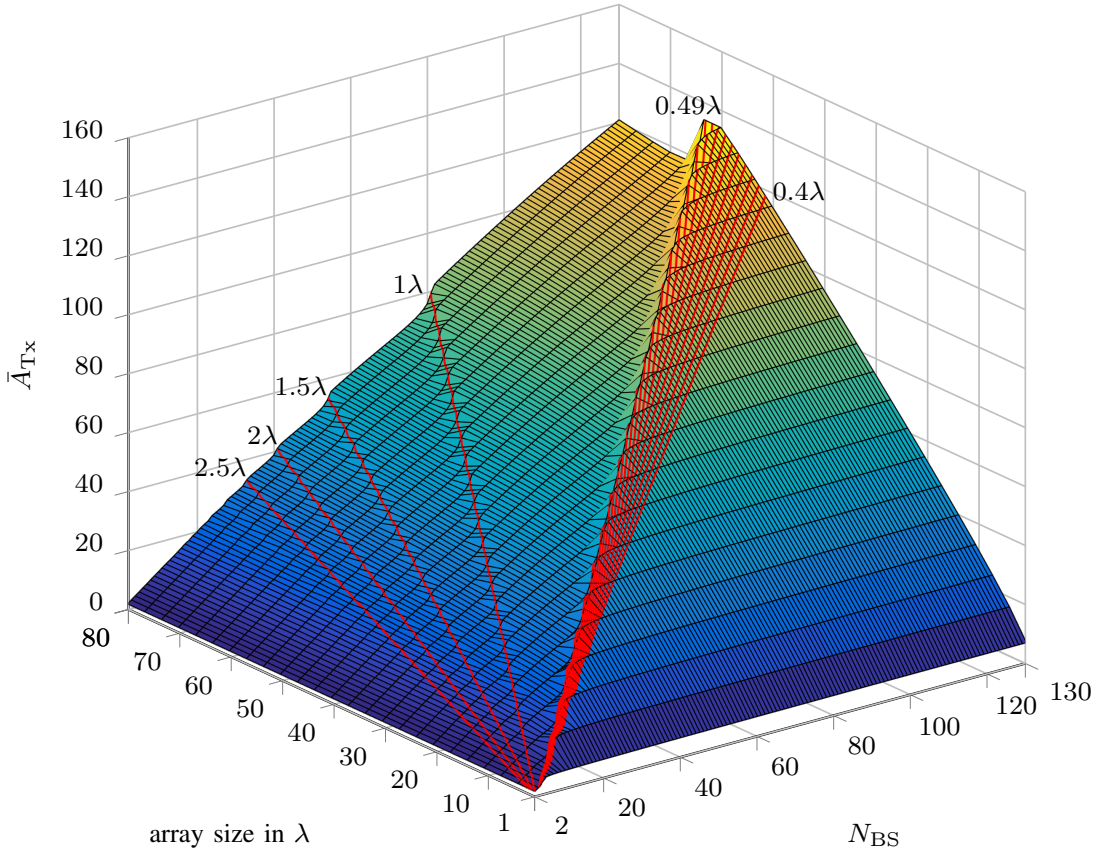

Fig. 5.15. $\bar{A}_{\mathrm{Tx}}$ for a ULA transmitting into all azimuth directions with uniform probability, where the lines for $d = 0.4\lambda$ to 0.49λ are in 0.01λ increments.

are orthogonal to the vertically polarized receiver for $\theta \in \{0, \pi\}$, and to the horizontally polarized receiver for $\varphi = \pi/2$, so $G_{\mathrm{V,Tx}} = 0$ and $G_{\mathrm{H,Tx}} = 0$ at these angles, respectively. That implies, $G_{\mathrm{H,Tx}} = 0$ in endfire direction.

5.5.3 URA in Fixed Directions

Third, consider the array gain for the URA with different antenna spacing d and array size. Fig. 5.19 shows $G_{\mathrm{V,Tx}}$ in frontfire direction, which is the same for vertically and horizontally polarized receivers due to symmetry. There is a large peak at about $d = 0.7\lambda$ for a small number of antennas that moves closer to $d = \lambda$ as the number of antennas increases. If we ignore mutual coupling, we would expect that (5.34) holds, which is about 236 for $N_{\mathrm{BS}} = 144$, but here $G_{\mathrm{V,Tx}} \approx 662$, which is even larger compared to the ULA, see Fig. 5.16. For larger antenna separations, $G_{\mathrm{V,Tx}}$ quickly decreases and then increases again, but not to the same level as the large peak.

For a receiver in $\varphi = 60°$ direction and vertical polarization, see Fig. 5.21a, there are two peaks with almost the same height, one close to $d = \lambda$ ($G_{\mathrm{V,Tx}} \approx 157$ for $N_{\mathrm{BS}} = 144$) and the other one close to $d = 1.5\lambda$ ($G_{\mathrm{V,Tx}} \approx 159$ for $N_{\mathrm{BS}} = 144$). Both of them are not nearly as high as the one in frontfire direction. It is expected that it is not as large, as this direction is not at the maximum of the dipoles' radiation patterns. Between the peaks, there is a large variation in transmit gain, e.g., between $d = \lambda$ and $d = 1.5\lambda$ it can be as low as about 102 for $N_{\mathrm{BS}} = 144$. For a horizontally oriented receiver, see Fig. 5.21b, the largest peak is a bit below $d = \lambda/2$, and only about half as high

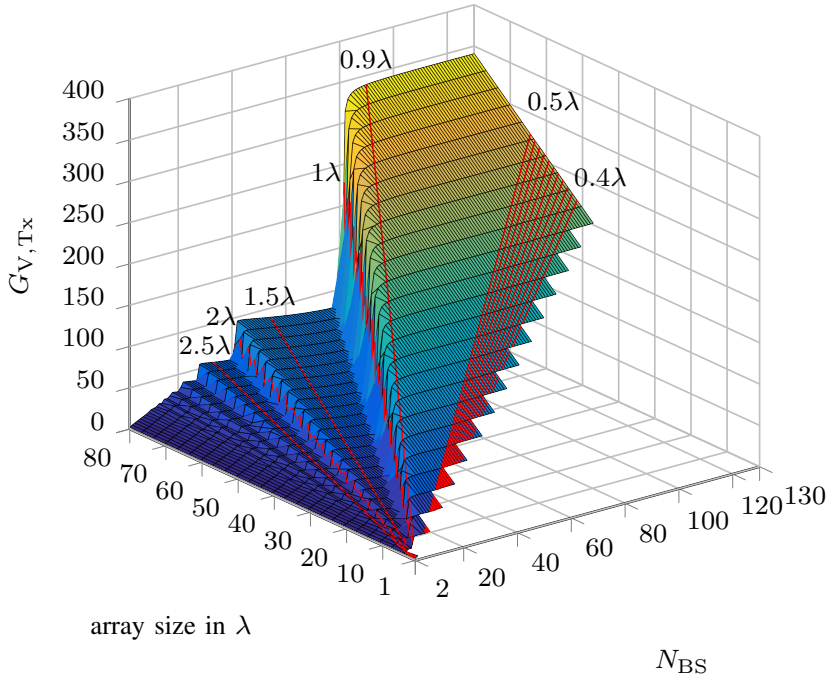

Fig. 5.16. Transmit gain for a ULA with dual-polarized $\lambda/2$-dipoles transmitting into frontfire direction ($\theta = \pi/2, \varphi = 0$) with a vertically polarized receiver, where the lines for $d = 0.4\lambda$ to 0.5λ are in 0.01λ increments [23].

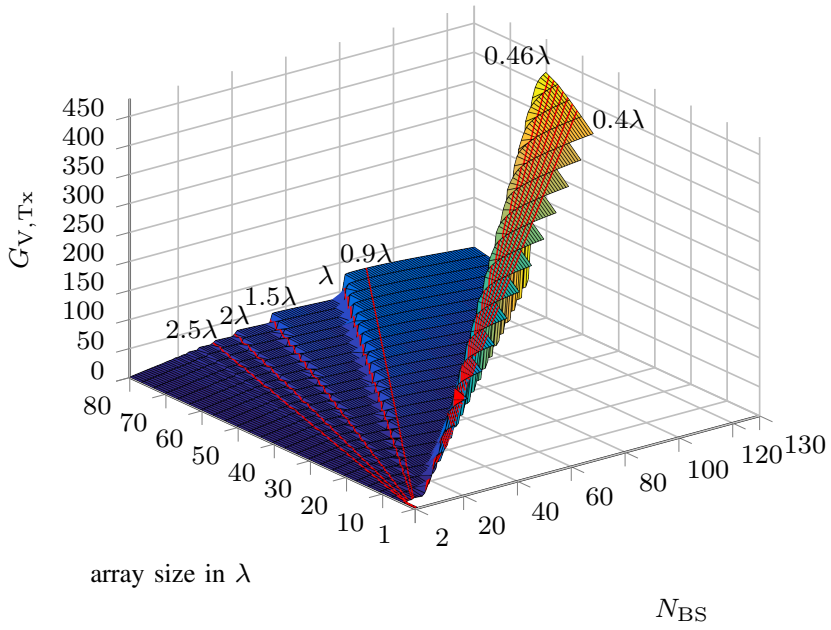

Fig. 5.17. Transmit gain for a ULA with dual-polarized $\lambda/2$-dipoles transmitting into endfire direction ($\theta = \pi/2, \varphi = \pi/2$) with a vertically polarized receiver, where the lines for $d = 0.4\lambda$ to 0.46λ are in 0.01λ increments [23].

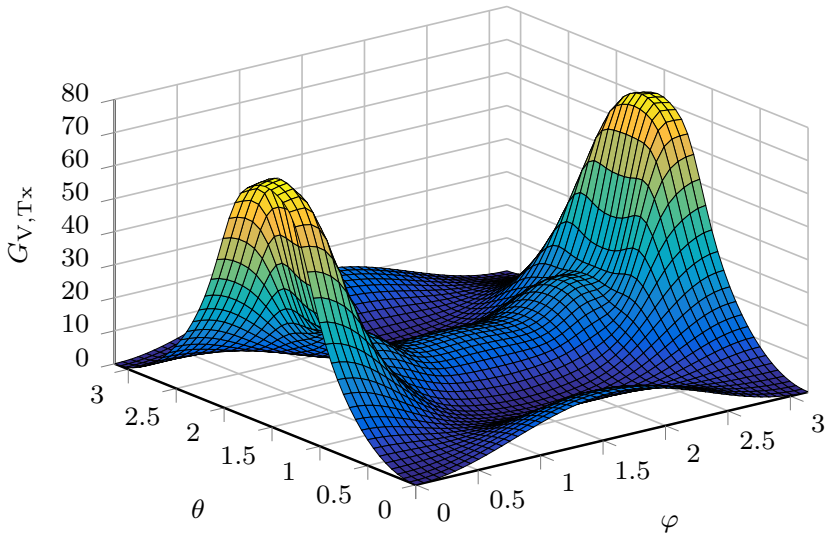

(a) Vertically polarized receiver.

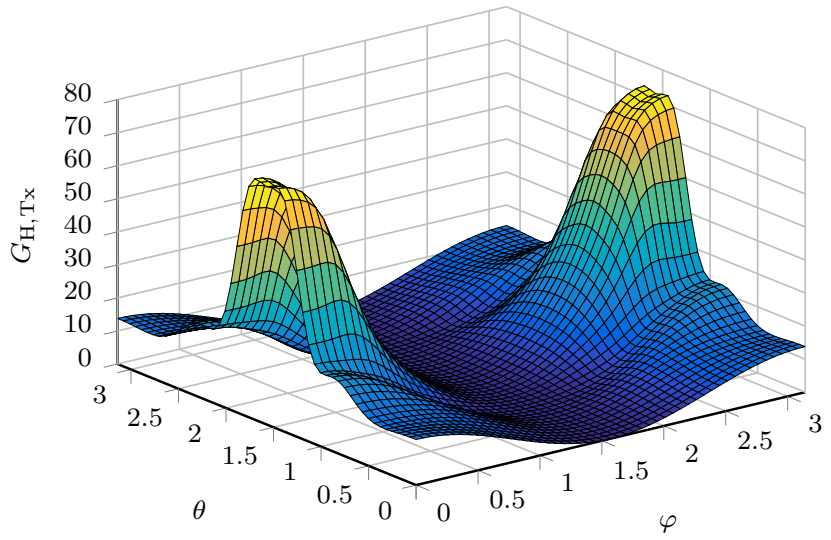

(b) Horizontally polarized receiver.

Fig. 5.18. Transmit gain for a URA with 5×5 dual-polarized $\lambda/2$-dipoles with $d = \lambda/\sqrt{2}$ antenna spacing [23].

as those for vertical polarization ($G_{\mathrm{H,Tx}} \approx 76$ for $N_{\mathrm{BS}} = 144$). There are further peaks for larger d, but $G_{\mathrm{H,Tx}}$ decreases rather quickly to around 35 at $d \approx 2.5\lambda$ and $N_{\mathrm{BS}} = 144$.

For a receiver in endfire direction, $G_{\mathrm{H,Tx}} = 0$ as expected as the transmitter's and receiver's polarization(s) are orthogonal. In vertical polarization, see Fig. 5.20, there are large peaks for d a bit smaller than $\lambda/2$, λ, and 1.5λ, but the largest peaks are at d a bit smaller than 2λ and 2.5λ ($G_{\mathrm{V,Tx}} \approx 108$ and $G_{\mathrm{V,Tx}} \approx 104$ for $N_{\mathrm{BS}} = 144$ respectively).

Therefore, for maximum gain, the URA should be oriented such that the direction of interest is close to the frontfire direction. In particular there should not be any direction of interest close to the endfire direction with a horizontally polarized receiver. If there is only interest in the frontfire direction, the optimum d is a bit smaller than λ, which may be as small as 0.7λ for small N_{BS}. This choice is also a good compromise for other directions of interest.

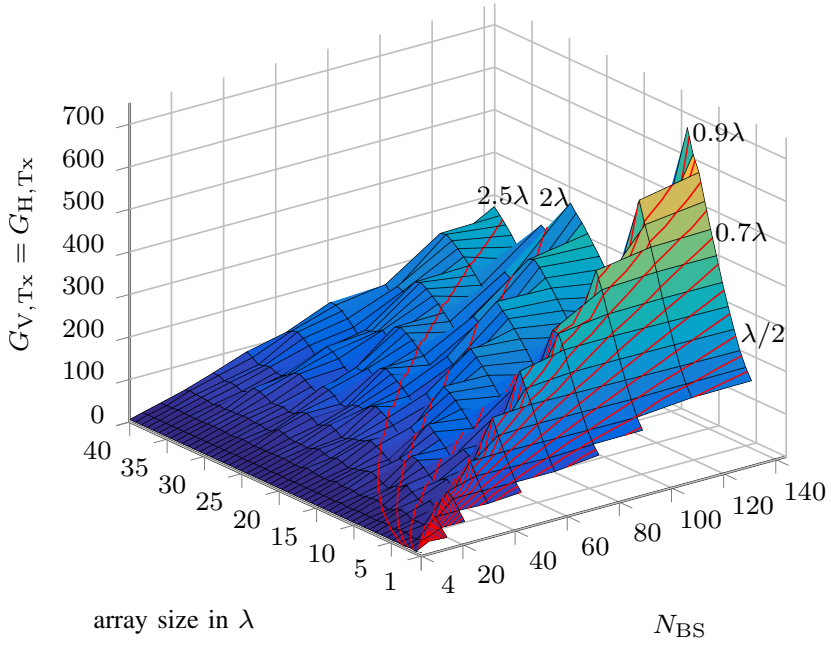

Fig. 5.19. Transmit gain for a square URA with dual-polarized $\lambda/2$-dipoles transmitting into frontfire direction ($\theta = \pi/2, \varphi = 0$) with a vertically or horizontally polarized receiver, where the curves for $d = 0.4\lambda$ to λ are in 0.05λ increments [23].

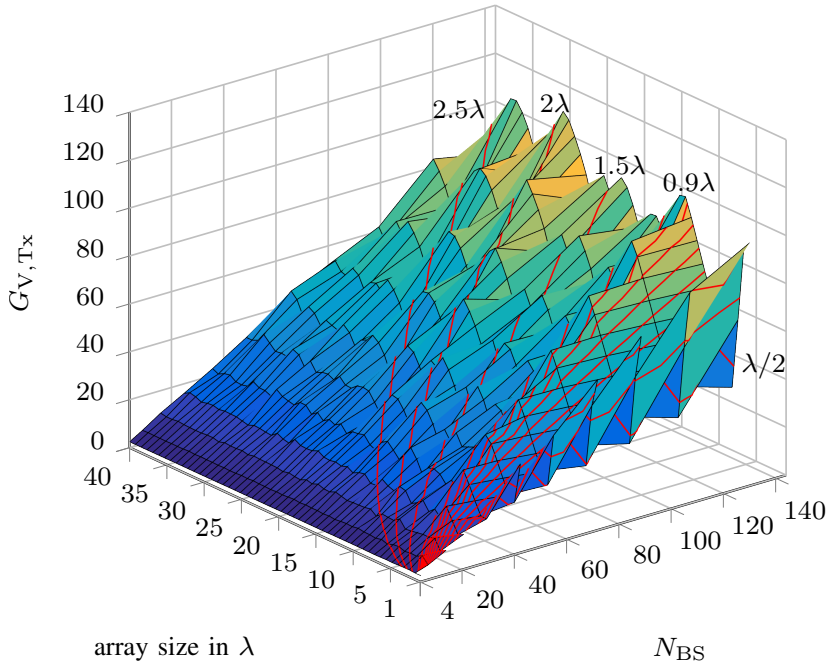

Fig. 5.20. Transmit gain for a square URA with dual-polarized $\lambda/2$-dipoles transmitting into endfire direction ($\theta = \pi/2, \varphi = \pi/2$) with a vertically polarized receiver, where the curves for $d = 0.4\lambda$ to λ are in 0.05λ increments [23].

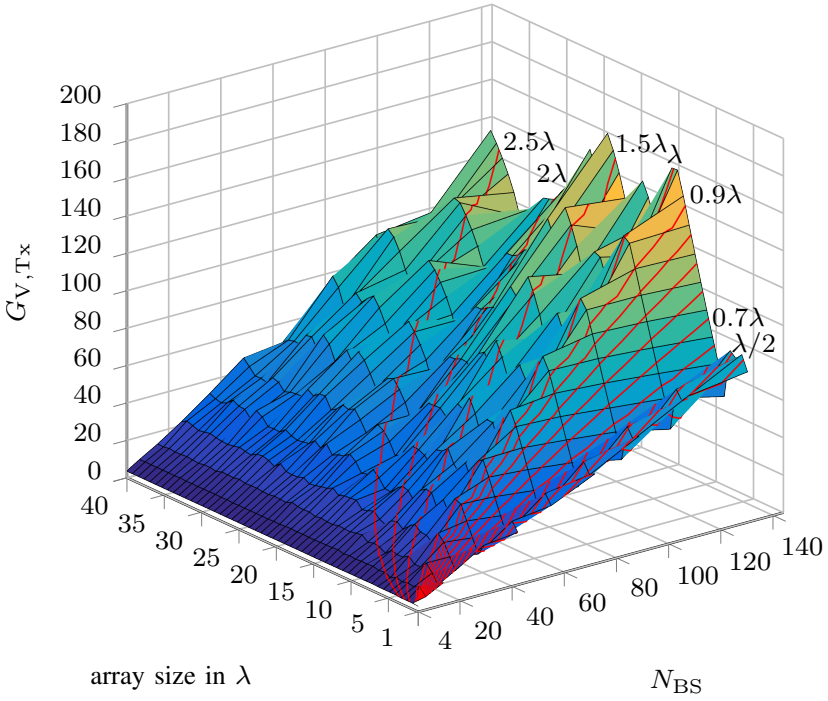

(a) Vertically polarized receiver.

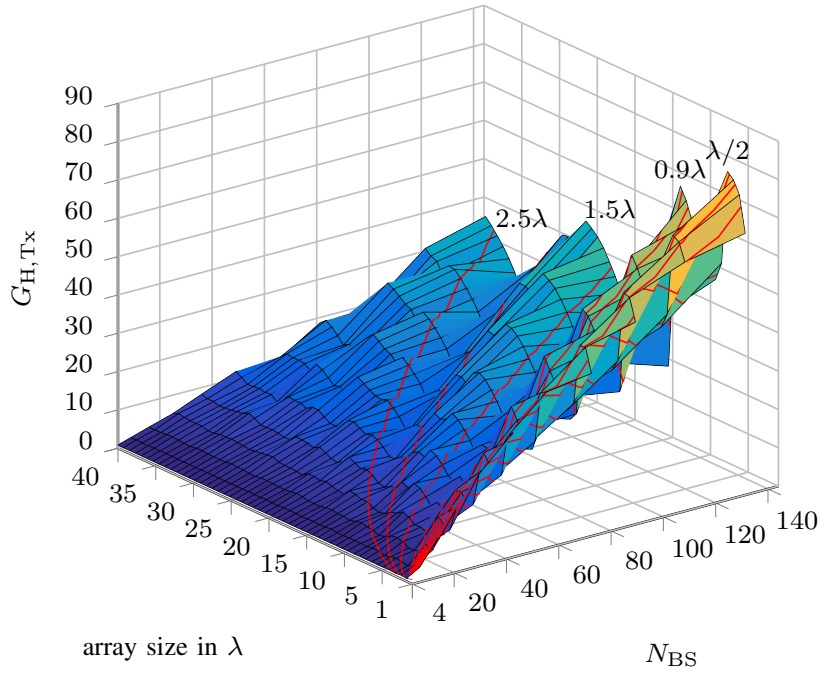

(b) Horizontally polarized receiver.

Fig. 5.21. Transmit gain for a square URA with dual-polarized $\lambda/2$-dipoles transmitting into $\varphi = 60°$ direction ($\theta = \pi/2$), where the curves for $d = 0.4\lambda$ to λ are in 0.05λ increments [23].

5.6 Conclusion

Firstly, we have shown for two different massive MIMO scenarios, one with a fixed distance between the antennas and one with a fixed size of the array, that the transmit array gain saturates above a certain number of antennas – contrary to the expectation of a linear increase with the number of antennas when mutual coupling is neglected. Similarly, the receive array gain saturates when there is only thermal noise from the antennas at the receiver. However, if there is noise from the LNA and other components in the receive chains and no decoupling network, as it would be almost impossible to implement for massive MIMO, the coupling of this noise between the receive chains leads to a maximum of the receive gain for a certain number of antennas, and a decreasing receive gain for a larger number of antennas. Therefore it is essential to take mutual coupling into account in the design of large scale massive MIMO systems because otherwise, large array gains, which are unphysical, may be predicted. Secondly, we have derived practical design recommendations for ULAs and UCAs: ULAs should be oriented such that their endfire direction points in the direction of interest, and for both ULAs and UCAs, the optimum antenna spacing is slightly below $\lambda/2$. Future work includes the analysis of the array gain in a rich scattering environment. We have further investigated the transmit gain for ULAs and square URAs with $\pm 45^\circ$ dual-polarized $\lambda/2$-dipoles and compared it to the transmit array gain of ULAs consisting of vertical $\lambda/2$-dipoles. The maximum transmit gain for the URA is achieved in frontfire direction with an antenna spacing that grows from 0.7λ to below λ with an increasing number of antennas.

6. Conclusion

We have investigated several aspects of physically consistent modeling of multi-antenna systems. In Chapter 2, we have reviewed the Multiport Communication Theory. First, we have reviewed the circuit model of the communication system, as well as matching strategies. Second, we have presented a simple circuit model without DMNs. Next, we reviewed the physically consistent mapping from the circuit model to the typical wireless communication model. Furthermore, we have discussed which matrices change when the mutual coupling is neglected. Moreover, we have reviewed the properties of infinitely thin, but perfectly conducting $\lambda/2$-dipoles, as well as those of UCAs, ULAs and URAs. In addition, we have derived the self and mutual impedance of infinitely thin dipoles with arbitrary rotation. Lastly, we have presented a more realistic array consisting of 200 antenna elements that was simulated in CST Studio Suite.

In Chapter 3, we have investigated the reciprocity of the information theoretic channel in a TDD system, and have found that by incorporating the physical noise model and the power consistency, the ordinary (pseudo-physical) reciprocity relation between the uplink and the downlink channel does not hold. Instead, a physically consistent reciprocity relation holds. Then we have presented a fair comparison between a system with physically consistent modeling and one with conventional modeling for i.i.d. channels and for channels generated by QuaDRiGa. The simulations results show that with conventional modeling, there can be a significant rate loss, and the base station cannot predict the power it radiates accurately. For multi-user transmission, it also leads to intra-cell interference between different users. The results also show that compact antenna arrays can lead to a better performance. We have proposed to take the mutual coupling into account by using two matrix multiplications that can be determined offline.

In Chapter 4, we have first derived the mutual reactance of hypothetical isotropic radiators based on passivity and the dispersion relations. Secondly, we have investigated the impact on the mutual impedance for ULAs with zero mutual resistance and a UCA with zero mutual resistance, all consisting of hypothetical isotropic radiators. Thirdly, we have investigated the impact for ULAs with the same antenna spacing, but with $\lambda/2$-dipoles, which are more realistic. These ULAs have a small mutual resistance. The numerical results for i.i.d. channels and channels generated by QuaDRiGa have shown the impact of neglecting the mutual impedance. This impact should be taken into account.

In Chapter 5, we have investigated the limits of transmit and receive array gain. Firstly, we have considered two massive MIMO scenarios, one with a fixed distance between the antennas and one with a fixed size of the array, and shown that the transmit array gain starts to saturate above a certain number of antennas, whereas a linear increase with the number of antennas is expected when mutual coupling is neglected. Furthermore, we have shown that there is a maximum in the receive array gain due to the noise from the LNA and other components in the receive chains in a system without

DMNs. Secondly, we have derived design recommendations for ULAs and UCAs with parallel $\lambda/2$-dipoles, and for URAs consisting of dual-polarized $\lambda/2$-dipoles.

In conclusion, we have highlighted the importance of physically consistent modeling for wireless communication systems employing antenna arrays with a large number of antennas and a small antenna separation at the transmitter and receiver. It allows to exploit the full performance of the arrays with only a small increase in computational complexity for a given linear multi-port description of the antenna array. Furthermore, we have shown that compact antenna arrays can lead to a better performance. Although the numerical results are based on canonical minimum scattering antennas for an analytic calculation of the impedance matrices of the arrays, the analysis is not limited to these types of antenna elements.

Appendix

A1 Consistency Check

Before using the S-parameters and the radiation patterns CST Studio Suite 2021 provides using the integral equation solver, we have conducted a consistency check of the data, because the numerical results depend on parameters like the mesh.

Consider an antenna array with N antennas at a certain frequency f that is excited at port n with an incident wave and terminated at all other ports with $R = 50\,\Omega$, see Fig. A1. All scattering parameters are assumed to be w.r.t. a reference impedance of $50\,\Omega$. That means the reflection coefficient of all terminations is zero.

The realized antenna efficiency is defined as

$$\eta_{\mathrm{r,ant}} = \frac{P_{\mathrm{rad}}}{P_0}, \tag{A1}$$

where P_{rad} is the radiated power (in the far field), P_0 is the available input power and P_{in} is the accepted power. P_{rad} can be computed based on the Poynting vector component in r-direction S_r:

$$\begin{aligned} P_{\mathrm{rad}} &= \int_{\theta=0}^{\theta=\pi} \int_{\varphi=0}^{2\pi} \mathrm{Re}(S_r) r^2 \sin(\theta)\, d\varphi\, d\theta = \int_{\theta=0}^{\theta=\pi} \int_{\varphi=0}^{2\pi} \frac{|E_\theta(r,\theta,\varphi)|^2 + |E_\varphi(r,\theta,\varphi)|^2}{Z_0} r^2 \sin(\theta)\, d\varphi\, d\theta \\ &= \int_{\theta=0}^{\theta=\pi} \int_{\varphi=0}^{2\pi} \frac{|rE_\theta(r,\theta,\varphi)|^2 + |rE_\varphi(r,\theta,\varphi)|^2}{Z_0} \sin(\theta)\, d\varphi\, d\theta. \end{aligned} \tag{A2}$$

Note that $|rE_\theta(r,\theta,\varphi)|$ and $|rE_\varphi(r,\theta,\varphi)|$ are independent of r in the far-field. Then the realized antenna efficiency is

$$\eta_{\mathrm{r,ant}} = \frac{1}{Z_0 P_0} \int_{\theta=0}^{\theta=\pi} \int_{\varphi=0}^{2\pi} \left(|rE_\theta(r,\theta,\varphi)|^2 + |rE_\varphi(r,\theta,\varphi)|^2 \right) \sin(\theta)\, d\varphi\, d\theta. \tag{A3}$$

With the radiation patterns CST Studio Suite provides, $\eta_{\mathrm{r,ant}}$ is computed for a regular grid of $M+1$ samples of θ and $L+1$ samples of φ by numerical integration of the samples of rE_θ, rE_φ using the trapezoidal rule. This means that $\eta_{\mathrm{r,ant}}$ based on the radiation patterns is computed in the following

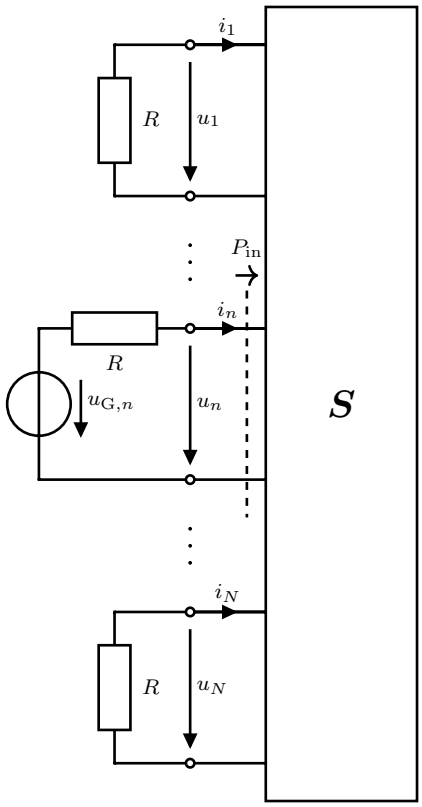

Fig. A1. Circuit model of the transmitter for the consistency check at port n of the antenna array.

way:

$$\theta_m = m\frac{\pi}{M}, \qquad m = 0, \ldots, M, \qquad \varphi_l = l\frac{2\pi}{L}, \qquad l = 0, \ldots, L, \tag{A4}$$

$$\eta_{\mathrm{r,ant}} = \frac{1}{Z_0 P_0} \sum_{m=1}^{M} \frac{\theta_m - \theta_{m-1}}{2} \left[f(\theta_m)\sin(\theta_m) + f(\theta_{m-1})\sin(\theta_{m-1}) \right], \tag{A5}$$

$$\begin{aligned} f(\theta) = \sum_{l=1}^{L} \frac{\varphi_l - \varphi_{l-1}}{2} \big(& |rE_\theta(r,\theta,\varphi_l)|^2 + |rE_\varphi(r,\theta,\varphi_l)|^2 \\ & + |rE_\theta(r,\theta,\varphi_{l-1})|^2 + |rE_\varphi(r,\theta,\varphi_{l-1})|^2 \big). \end{aligned} \tag{A6}$$

Let us now compute an upper bound on $\eta_{\mathrm{r,ant}}$ based on the S-parameter matrix $\boldsymbol{S}$ of the antenna array. To upper bound P_{rad} based on $\boldsymbol{S}$, we compute P_{in} in the following way:

$$P_{\mathrm{in}} = P_0 - \sum_{k=1}^{N} P_{\mathrm{ohm,k}} = \left(1 - \sum_{k=1}^{N} |S_{kn}|^2 \right) P_0, \tag{A7}$$

where $P_{\mathrm{ohm,k}}$ is the power dissipated in the termination at port k. Note that this equation holds as the reflection coefficient of the terminations is zero. Then the inequality

$$P_{\mathrm{in}} = P_{\mathrm{rad}} + P_{\mathrm{loss}} \geq P_{\mathrm{rad}} \tag{A8}$$

holds, where P_{loss} is the power loss in the antenna structure. In other words, the power accepted by the multi-port based on the S-parameters consists of the radiated power plus the losses in the

antenna structure, and therefore the accepted power is larger or equal than the radiated power. Divide (A8) by P_0 on both sides. Then

$$\eta_{\mathrm{r,in}} \coloneqq \frac{P_{\mathrm{in}}}{P_0} = 1 - \sum_{k=1}^{N} |S_{kn}|^2 \geq \frac{P_{\mathrm{rad}}}{P_0} = \eta_{\mathrm{r,ant}}. \tag{A9}$$

In the numerical results, $\eta_{\mathrm{r,in}} \geq \eta_{\mathrm{r,ant}}$ should hold, but $\eta_{\mathrm{r,in}}/\eta_{\mathrm{r,ant}}$ lies between $98.4\,\%$ and $99.3\,\%$ due to numerical inaccuracies. Note that $\eta_{\mathrm{r,in}} < \eta_{\mathrm{r,ant}}$ is inconsistent with a passive system. Since the antenna array obviously is a passive multiport, this means that the computation of the field components E_θ, E_φ and the S-matrix elements S_{kn} is slightly inconsistent due to numerical inaccuracies, but this should be good enough for our purposes. We have also replaced all singular values of $\boldsymbol{S}$ that were slightly larger than 1 due to numerical inaccuracies with 1 to ensure passivity, and ensured that $\boldsymbol{S}$ is symmetric by taking $(\boldsymbol{S} + \boldsymbol{S}^T)/2$, as the antenna array is reciprocal.

A2 Efficient Computation of Impedance Matrices

For a ULA consisting of parallel canonical minimum scattering dipoles, its impedance matrix $\boldsymbol{Z}$ can be computed efficiently by computing the first row of $\boldsymbol{Z}$, $\boldsymbol{z}_1^T$, and then exploiting that $\boldsymbol{Z}$ is a Toeplitz matrix. Note that the first column of $\boldsymbol{Z}$ is the same as $\boldsymbol{z}_1$, as $\boldsymbol{Z}$ is symmetric. This means that

$$\boldsymbol{Z} = \mathrm{toeplitz}(\boldsymbol{z}_1, \boldsymbol{z}_1^T), \tag{A10}$$

where $\mathrm{toeplitz}(\boldsymbol{z}_{\mathrm{c}}, \boldsymbol{z}_{\mathrm{r}})$ constructs a Toeplitz matrix based on the first column $\boldsymbol{z}_{\mathrm{c}}$ and first row $\boldsymbol{z}_{\mathrm{r}}^T$ of the matrix to be constructed, see also [84].

For a UCA consisting of N parallel dipoles that are oriented such that they are perpendicular to the circle connecting their centers, the impedance matrix $\boldsymbol{Z}$ can be computed efficiently by computing the first $\lceil (N+1)/2 \rceil$ entries of $\boldsymbol{z}_1$, and then exploiting that $\boldsymbol{Z}$ is circulant. The remaining entries of $\boldsymbol{z}_1$ can be obtained using symmetry, i.e., $z_{1,N-n} = z_{1,n+2}$. Due to this symmetry, $\boldsymbol{Z}$ is a symmetric Toeplitz matrix as well, and (A10) applies.

Consider a URA consisting of $N_x N_y$ parallel dipoles. Let us partition $\boldsymbol{Z}$ into $N_y N_y$ $N_x \times N_x$ matrices

$$\boldsymbol{Z} = \begin{bmatrix} \boldsymbol{Z}_{1,1} & \cdots & \boldsymbol{Z}_{1,N_y} \\ \vdots & \ddots & \vdots \\ \boldsymbol{Z}_{N_y,1} & \cdots & \boldsymbol{Z}_{N_y,N_y} \end{bmatrix}. \tag{A11}$$

Then $\boldsymbol{Z}_{m,n}$ represents the (mutual) impedance matrix between the m-th and n-th row of the URA. Due to symmetry, it is sufficient to compute the upper triangular part of $\boldsymbol{Z}$. Furthermore, due to the regular structure of the URA, it is sufficient to compute the first row of $\boldsymbol{Z}$, because it is block-Toeplitz. For the computation of $\boldsymbol{Z}_{1,1}$, which corresponds to the impedance matrix of the first row of the URA, one can exploit its symmetric Toeplitz structure, similarly to the ULA. For the computation of $\boldsymbol{Z}_{1,n}$ with $n > 1$, which corresponds to the mutual impedance matrix between the first and the n-th row, we have a Toeplitz structure again. It is symmetric as well, if the dipoles are perpendicular to the plane of the URA or if the dipoles lie in the plane and are parallel to the x- or y-direction, see Section 2.3. Then the mutual impedance between the k-th dipole in the first row and the l-th dipole in the n-th row is the same as that between the l-th dipole in the first row and the k-th dipole in the n-th row.

To extend this consideration to a URA consisting of $N_x N_y$ dual-polarized dipoles that lie in the URA's plane, see Fig. 2.12, we split each row into two virtual rows, where each virtual row consists of antenna elements with identical polarization. We then partition $\boldsymbol{Z}$ into $N_x \times N_x$ matrices $\boldsymbol{Z}_{m,n}$ that correspond to the (mutual) impedance matrices between virtual rows

$$\boldsymbol{Z} = \begin{bmatrix} \boldsymbol{Z}_{1,1} & \cdots & \boldsymbol{Z}_{1,N_y} & \boldsymbol{Z}_{1,N_y+1} & \cdots & \boldsymbol{Z}_{1,2N_y} \\ \vdots & \ddots & \vdots & \vdots & \ddots & \vdots \\ \boldsymbol{Z}_{N_y,1} & \cdots & \boldsymbol{Z}_{N_y,N_y} & \boldsymbol{Z}_{N_y,N_y+1} & \cdots & \boldsymbol{Z}_{N_y,2N_y} \\ \boldsymbol{Z}_{N_y+1,1} & \cdots & \boldsymbol{Z}_{N_y+1,N_y} & \boldsymbol{Z}_{N_y+1,N_y+1} & \cdots & \boldsymbol{Z}_{N_y+1,2N_y} \\ \vdots & \ddots & \vdots & \vdots & \ddots & \vdots \\ \boldsymbol{Z}_{2N_y,1} & \cdots & \boldsymbol{Z}_{2N_y,N_y} & \boldsymbol{Z}_{2N_y,N_y+1} & \cdots & \boldsymbol{Z}_{2N_y,2N_y} \end{bmatrix}, \tag{A12}$$

where the antenna elements 1 to N_y have the same polarization, and the antenna elements N_y to $2N_y$ polarized orthogonally. The matrices

$$\begin{bmatrix} \boldsymbol{Z}_{1,1} & \cdots & \boldsymbol{Z}_{1,N_y} \\ \vdots & \ddots & \vdots \\ \boldsymbol{Z}_{N_y,1} & \cdots & \boldsymbol{Z}_{N_y,N_y} \end{bmatrix} \quad \text{and} \quad \begin{bmatrix} \boldsymbol{Z}_{N_y+1,N_y+1} & \cdots & \boldsymbol{Z}_{N_y+1,2N_y} \\ \vdots & \ddots & \vdots \\ \boldsymbol{Z}_{2N_y,N_y+1} & \cdots & \boldsymbol{Z}_{2N_y,2N_y} \end{bmatrix} \tag{A13}$$

can be computed similarly to the URA consisting of parallel dipoles. This means that it is sufficient to compute the matrices in the first row, and then the complete matrices can be obtained based on the block-Toeplitz structure and the symmetry of $\boldsymbol{Z}$. The matrices $\boldsymbol{Z}_{1,n}$ for $n = 1, \ldots, N_y$ and $\boldsymbol{Z}_{N_y+1,n}$ for $n = N_\mathrm{y} + 1, \ldots, 2N_y$, fulfill again a Toeplitz structure, but they are only symmetric for $n \in \{1, N_\mathrm{y} + 1\}$, because the dipoles are not oriented such that they fulfill the criterion described in the previous paragraph. Therefore the first row and column of each of these matrices need to be computed separately. Similarly, the matrix

$$\begin{bmatrix} \boldsymbol{Z}_{1,N_y+1} & \cdots & \boldsymbol{Z}_{1,2N_y} \\ \vdots & \ddots & \vdots \\ \boldsymbol{Z}_{N_y,N_y+1} & \cdots & \boldsymbol{Z}_{N_y,2N_y} \end{bmatrix} \tag{A14}$$

is block-Toeplitz, and the block matrices $\boldsymbol{Z}_{1,N_y+1}$ to $\boldsymbol{Z}_{1,2N_y}$, and $\boldsymbol{Z}_{1,N_y+1}$ to $\boldsymbol{Z}_{N_y,N_y+1}$ are Toeplitz, but neither the large matrix nor the small matrices are symmetric in general.

For the further extension to a scenario where the URA is parallel to a reflector, see (2.61), $\boldsymbol{Z}_\mathrm{orig}$ can be computed as just described, and $\boldsymbol{Z}_\mathrm{mutual}$ can be computed in a similarly to $\boldsymbol{Z}_\mathrm{orig}$, where the difference is that there is an extra distance between the original and the reflector antennas.

A3 Influence of the Generators' Internal Impedance and that of the Load Impedance

Consider the influence of the generators' internal impedance Z_G and that of the load impedance Z_L on capacity. C is independent of Z_G. C depends on $\boldsymbol{H}$. $\boldsymbol{H}$ in turn depends on $\boldsymbol{D}$, $\boldsymbol{B}^{-H/2}$ and $\sqrt{R_\mathrm{G}}$, which depend on Z_G, but the product $\sqrt{R_\mathrm{G}}\boldsymbol{D}\boldsymbol{B}^{-H/2}$ is independent of Z_G, see (2.10), (2.21) and (2.23). Even if one chooses a different $\boldsymbol{B}_1^{-H/2} = \boldsymbol{B}^{-H/2}\boldsymbol{U}$, which leads to some $\boldsymbol{H}_1$ and where $\boldsymbol{U}$ is a unitary matrix, $\boldsymbol{H}_1 = \boldsymbol{H}\boldsymbol{U}$ is independent of Z_G, unless $\boldsymbol{U}$ is a function of Z_G. As the noise covariance $\boldsymbol{R}_\eta$ is independent of Z_G as well, capacity is independent of Z_G.

C is also independent of Z_{L}, because $\boldsymbol{u}_{\mathrm{L}}$ only depends on Z_{L} through $Z_{\mathrm{L}}(\boldsymbol{Z}_{22}+Z_{\mathrm{L}}\boldsymbol{I})^{-1}$, which is part of $\boldsymbol{D}$ and $\boldsymbol{R}_{\eta}$, see (2.10), (2.15) and (2.17). [1] As this is an invertible transform that is applied to both the received signal and the noise, capacity before and after the transform is the same. This was already noted in [27]. This implies that capacity is independent of Z_{L}. This result also matches that the noise figure is independent of Z_{L}. Note that this also holds for multi-user scenarios, because the matrix $Z_{\mathrm{L}}(\boldsymbol{Z}_{22}+Z_{\mathrm{L}}\boldsymbol{I})^{-1}$ is block-diagonal, so that each user can invert that part of the transform that affects its channel individually.

R_{hyp} does depend on Z_{G}. Consider

$$\hat{\boldsymbol{H}} = \sigma_{\vartheta}\frac{\sqrt{R_{\mathrm{G}}}}{\sqrt{R_{\mathrm{L}}}}\boldsymbol{R}_{\eta}^{-1/2}\boldsymbol{D}\hat{\boldsymbol{B}}^{-H/2}, \tag{A15}$$

$$\hat{\boldsymbol{H}}' = \sigma_{\vartheta}\frac{\sqrt{R_{\mathrm{G}}}}{\sqrt{R_{\mathrm{L}}}}\hat{\boldsymbol{R}}_{\eta}^{-1/2}\boldsymbol{D}\hat{\boldsymbol{B}}^{-H/2}, \tag{A16}$$

which is different from (3.22) and (3.32), because we do not assume $Z_{\mathrm{L}} = Z_{\mathrm{G}}$ here. There is a dependence on Z_{G}, because the factor $(\boldsymbol{Z}_{11}+Z_{\mathrm{G}}\boldsymbol{I})^{-1}$ inside of $\sqrt{R_{\mathrm{G}}}\boldsymbol{D}\hat{\boldsymbol{B}}^{-H/2}$ is not canceled out, see (2.10) and (3.19). $\hat{\boldsymbol{H}}$ is independent of Z_{L} similarly to $\boldsymbol{H}$, but $\hat{\boldsymbol{H}}'$ does depend on Z_{L}, because transform with $Z_{\mathrm{L}}(\boldsymbol{Z}_{22}+Z_{\mathrm{L}}\boldsymbol{I})^{-1}$ is not inverted. This means that in general, R_{hyp} also depends on Z_{L}. Note that in the SU-MISO and MU-MISO scenarios, $Z_{\mathrm{L}}(\boldsymbol{Z}_{22}+Z_{\mathrm{L}}\boldsymbol{I})^{-1}$ is a scaled identity matrix and $\boldsymbol{R}_{\eta} = \hat{\boldsymbol{R}}_{\eta}$, which makes R_{hyp} independent of Z_{L}, because a scaling both signal and noise with the same factor does not change the rate, and the noise distribution at the mobiles is what the base station expects.

Similarly to C, R_{recip} is independent of Z_{G} and Z_{L}, because $\boldsymbol{H}$ and $\boldsymbol{H}_{\mathrm{UL}}$ are independent of them. $\boldsymbol{H}$ is independent as discussed above for C, and $\boldsymbol{H}_{\mathrm{UL}}$ is independent with the same arguments.

Regarding the influence of two-port matching on capacity, see Section 2.1.

[1] Technically, $\boldsymbol{u}_{\mathrm{L}}$ also depends on $\sqrt{R_{\mathrm{L}}}$, because $\boldsymbol{\eta}$ is scaled by this factor, but it cancels with R_{L} in the denominator inside of $\boldsymbol{R}_{\eta}$.

List of Figures

Nomenclature

Abbreviations

3GPP	3rd Generation Partnership Project, page 1
5G	Fifth generation cellular wireless standard, page 1
6G	Sixth generation cellular wireless standard, page 1
ADC	Analog-to-digital converter, page 5
AWGN	Additive white Gaussian noise, page 7
BC	Broadcast channel, page 32
CSI	Channel state information, page 25
DAC	Digital-to-analog converter, page 5
DMN	Decoupling and impedance matching network, page 2
DPC	Dirty Paper Coding, page 33
EVD	Eigenvalue decomposition, page 31
FDD	Frequency division duplex, page 25
GSM	Global System for Mobile Communications, page 1
i.i.d.	independent and identically distributed, page 3
LNA	Low noise amplifier, page 7
LOS	Line-of-sight, page 55
LTE	Long Term Evolution, page 1
MAC	Multiple access channel, page 33
MIMO	Multiple-input multiple-output, page 1
MU-MIMO	Multi-User-Multiple Input Multiple Output, page 25
RF	Radio frequency, page 8
RMa	Rural macro, page 65
Rx	Receive, page 25
SNR	Signal-to-noise ratio, page 1
SVD	Singular value decomposition, page 32
TDD	Time Division Duplex, page 2
TS	Technical specification, page 3
Tx	Transmit, page 25
UCA	Uniform circular array, page 3
ULA	Uniform linear array, page 3
UMa	Urban macrocell, page 39
UMi	Urban micro, page 65
UMTS	Universal Mobile Telecommunications System, page 1
URA	Uniform rectangular array, page 3

ZF	Zero forcing, page 33	
Variables		
α	ratio between radiated and predicted radiated power, page 31	1
γR_r	dissipation resistance, page 60	Ω
λ	wavelength, page 1	m
$\boldsymbol{B}$	power-coupling matrix, page 11	1
$\boldsymbol{D}$	channel matrix, page 10	1
$\boldsymbol{H}$	information-theoretic channel, page 12	1
$\boldsymbol{Q}$	noise covariance matrix, page 11	V^2
$\boldsymbol{R}_\eta$	noise covariance matrix, page 11	W
$\boldsymbol{R}_\mathrm{A}$	covariance matrix corresponding to the extrinsic noise, page 10	V^2
$\boldsymbol{R}_x$	covariance matrix of $\boldsymbol{x}$, page 27	W
$\boldsymbol{Z}$	joint impedance matrix of the transmit and receive arrays, page 8	Ω
$\boldsymbol{Z}_{11}, \boldsymbol{Z}_\mathrm{BS}$	impedance matrix of the antenna array at the base station, page 8	Ω
$\boldsymbol{Z}_{21}$	mutual impedance between the antenna array at the base station and the antenna arrays at the mobiles, page 8	Ω
$\boldsymbol{Z}_{22}$	impedance matrix of the antenna arrays at the mobiles, page 8	Ω
σ_ϑ	standard deviation of $\boldsymbol{\vartheta}$, page 11	$\sqrt{\mathrm{W}}$
σ_i	standard deviation of the intrinsic current noise source, page 10	V
σ_u	standard deviation of the intrinsic voltage noise source, page 10	V
θ	zenith angle in the usual spherical coordinate system, page 18	rad
$\hat{\boldsymbol{B}}$	power-coupling matrix that ignores the mutual coupling, page 29	1
$\hat{\boldsymbol{H}}$	information-theoretic channel ignoring the mutual coupling, page 30	1
φ	azimuth angle in the usual spherical coordinate system, page 18	rad
$\boldsymbol{\eta}$	noise, page 8	$\sqrt{\mathrm{W}}$
$\boldsymbol{\vartheta}$	noise vector in the information-theoretic model, page 11	$\sqrt{\mathrm{W}}$
$\boldsymbol{u}_\mathrm{G}$	generator voltage, page 8	V
$\boldsymbol{u}_\mathrm{L}$	load voltage, page 8	V
$\boldsymbol{x}$	transmit vector in the information-theoretic model, page 11	$\sqrt{\mathrm{W}}$
$\boldsymbol{y}$	receive vector in the information-theoretic model, page 11	$\sqrt{\mathrm{W}}$
A_Rx	receive array gain, page 62	1
A_Tx	transmit array gain, page 62	1
C	capacity, page 27	bpcu
d	antenna separation, page 12	m
d_bm	distance between the base station and the mobile, page 64	m
G_Tx	transmit gain, page 73	1
k	angular wavenumber, page 14	m^{-1}
M	number of receive antennas, page 8	1
N	number of transmit antennas, page 8	1
$P_\mathrm{T,p}$	predicted transmit power, page 30	W
P_T	transmit power, page 11	W
R_hyp	(hypothetical) rate, page 30	bpcu
R_L	real part of Z_L, page 8	Ω
R_recip	rate with the ordinary reciprocity relation, page 32	bpcu
R_r	radiation resistance, page 45	Ω
Z_0	impedance of free space, page 14	Ω

Z_{A}	self-impedance of the antennas at the mobiles, page 27	Ω
Z_{G}	internal impedance of the generators, page 8	Ω
Z_{L}	input impedance of the receive chains, page 8	Ω
$Z_{\lambda/2}$	impedance of infinitely thin but perfectly conducting $\lambda/2$-dipoles, page 13	Ω

List of Publications

During the preparation of the thesis, several parts were published as papers in peer-reviewed international conferences and journals:

- T. Laas, J. A. Nossek, S. Bazzi, and W. Xu, "On reciprocity of physically consistent TDD systems with coupled antennas," in *Proc. 21st Int. ITG Workshop Smart Antennas (WSA)*, Berlin, Germany, Mar. 2017, pp. 377–382.
- T. Laas, J. A. Nossek, S. Bazzi, and W. Xu, "On the impact of the mutual impedance of an antenna array on power and achievable rate," in *Proc. 22nd Int. ITG Workshop Smart Antennas (WSA)*, Bochum, Germany, Mar. 2018.
- T. Laas, J. A. Nossek, S. Bazzi, and W. Xu, "On the impact of the mutual reactance on the radiated power and on the achievable rates," *IEEE Trans. Circuits Syst. II*, vol. 65, no. 9, pp. 1179–1183, Sep. 2018, doi: 10.1109/TCSII.2018.2796643.
- T. Laas, J. A. Nossek, and W. Xu, "Gain of uniform rectangular arrays," in *Proc. 24th Int. ITG Workshop Smart Antennas (WSA)*, Hamburg, Germany, Feb. 2020.
- T. Laas, J. A. Nossek, and W. Xu, "Limits of transmit and receive array gain in massive MIMO," in *Proc. IEEE Wireless Commun. Netw. Conf. (WCNC)*, Virtual Conference, South Korea, May 2020, doi: 10.1109/WCNC45663.2020.9120590, arXiv:2002.06107.
- T. Laas, J. A. Nossek, S. Bazzi, and W. Xu, "On reciprocity in physically consistent TDD systems with coupled antennas," *IEEE Trans. Wireless Commun.*, vol. 19, no. 10, pp. 6440–6453, Oct. 2020, doi: 10.1109/TWC.2020.3003414, arXiv:1907.10562.

In addition, several papers that are not directly related to the topic of the thesis were published in peer-reviewed international conferences and journals:

- T. Laas, L. G. Baltar, and J. A. Nossek, "Frequency-domain analysis of linear periodically time-varying FBMC systems," in *Proc. IEEE Sensor Array and Multichannel Signal Process. Workshop (SAM)*, Rio de Janeiro, Brazil, Jul. 2016, doi: 10.1109/SAM.2016.7569649.
- A. Kakkavas, M. Castañeda, J. Luo, T. Laas, W. Xu, and J. A. Nossek, "FBMC-OQAM with phase noise: Achievable performance and compensation," in *Proc. IEEE 18th Int. Workshop Signal Process. Advances Wireless Commun. (SPAWC)*, Sapporo, Japan, Jul. 2017, doi: 10.1109/SPAWC.2017.8227811.
- T. Laas and W. Xu, "On the Ziv-Zakai bound for time difference of arrival estimation in CP-OFDM systems," in *Proc. IEEE Wireless Commun. Netw. Conf. (WCNC)*, Nanjing, China, Mar./Apr. 2021, doi: 10.1109/WCNC49053.2021.9417566.

Bibliography

[1] 3GPP Homepage, "Release 15," accessed: 25 Nov 2020. [Online]. Available: http://www.3gpp.org/release-15

[2] 3GPP Homepage, "Release 16," accessed: 25 Nov 2020. [Online]. Available: http://www.3gpp.org/release-16

[3] M. Latva-aho and K. Leppänen, "Key drivers and research challenges for 6G ubiquitous wireless intelligence," University of Oulu, Oulu, Finland, Whitepaper, Oct. 2019.

[4] T. L. Marzetta, "Noncooperative cellular wireless with unlimited numbers of base station antennas," *IEEE Trans. Wireless Commun.*, vol. 9, no. 11, pp. 3590–3600, Nov. 2010, doi: 10.1109/TWC.2010.092810.091092.

[5] H. Asplund, D. Astely, P. von Butovitsch, T. Chapman, M. Frenne, F. Ghasemzadeh, M. Hagström, B. Hogan, G. Jöngren, J. Karlsson, F. Kronestedt, and E. Larsson, *Advanced Antenna Systems for 5G Network Deployments: Bridging the Gap Between Theory and Practice*, 1st ed. Academic Press, 2020.

[6] J. W. Wallace and M. A. Jensen, "Mutual coupling in MIMO wireless systems: A rigorous network theory analysis," *IEEE Trans. Wireless Commun.*, vol. 3, no. 4, pp. 1317–1325, Jul. 2004, doi: 10.1109/TWC.2004.830854.

[7] C. Waldschmidt, S. Schulteis, and W. Wiesbeck, "Complete RF system model for analysis of compact MIMO arrays," *IEEE Trans. Veh. Technol.*, vol. 53, no. 3, pp. 579–586, May 2004, doi: 10.1109/TVT.2004.825788.

[8] M. T. Ivrlač and J. A. Nossek, "Toward a circuit theory of communication," *IEEE Trans. Circuits Syst. I*, vol. 57, no. 7, pp. 1663–1683, Jul. 2010, doi: 10.1109/TCSI.2010.2043994.

[9] M. T. Ivrlač and J. A. Nossek, "The multiport communication theory," *IEEE Circuits Syst. Mag.*, vol. 14, no. 3, pp. 27–44, Aug. 2014, doi: 10.1109/MCAS.2014.2333618.

[10] S. Jaeckel, L. Raschkowski, K. Börner, L. Thiele, F. Burkhardt, and E. Eberlein, "QuaDRiGa – Quasi deterministic radio channel generator, user manual and documentation," Fraunhofer Heinrich Hertz Inst., Berlin, Germany, Tech. Rep. Version 2.0.0-664, Aug. 2017.

[11] S. Jaeckel, L. Raschkowski, K. Börner, and L. Thiele, "QuaDRiGa: A 3-D multi-cell channel model with time evolution for enabling virtual field trials," *IEEE Trans. Antennas Propag.*, vol. 62, no. 6, pp. 3242–3256, Jun. 2014, doi: 10.1109/TAP.2014.2310220.

[12] "Study on channel model for frequencies from 0.5 to 100 GHz," 3GPP, TS 38.901, Jun. 2017, Version 14.1.0.

[13] M. T. Ivrlač and J. A. Nossek, "On physical limits of massive MISO systems," in *Proc. 20th Int. ITG Workshop Smart Antennas (WSA)*, Munich, Germany, Mar. 2016, pp. 66–72.

[14] N. W. Bikhazi and M. A. Jensen, "The relationship between antenna loss and superdirectivity in MIMO systems," *IEEE Trans. Wireless Commun.*, vol. 6, no. 5, pp. 1796–1802, May 2007, doi: 10.1109/TWC.2007.360381.

[15] J. Brown, "Microwave optics," in *Advances in Electronics and Electron Physics*, L. Marton and C. Marton, Eds. New York, N.Y.: Academic Press, 1958, vol. X, pp. 107–152.

[16] T. L. Marzetta, "Super-directive antenna arrays: Fundamentals and new perspectives," in *Proc. 53rd Asilomar Conf. Signals, Syst., Comput.*, Pacific Grove, CA, USA, Nov. 2019, pp. 1–4, doi: 10.1109/IEEECONF44664.2019.9048753.

[17] E. Biglieri, R. Calderbank, A. Constantinides, A. Goldsmith, A. Paulraj, and H. V. Poor, *MIMO Wireless Communications*, 1st ed. Cambridge Univ. Press, 2007.

[18] H. M. Payntner, *Analysis and Design of Engineering Systems*. Cambridge, MA: M.I.T. Press, 1961. [Online]. Available: http://hdl.handle.net/2027/mdp.39015064874921

[19] M. L. Morris and M. A. Jensen, "Network model for MIMO systems with coupled antennas and noisy amplifiers," *IEEE Trans. Antennas Propag.*, vol. 53, no. 1, pp. 545–552, Jan. 2005, doi: 10.1109/TAP.2004.838774.

[20] C. P. Domizioli, B. L. Hughes, K. G. Gard, and G. Lazzi, "Noise correlation in compact diversity receivers," *IEEE Trans. Commun.*, vol. 58, no. 5, pp. 1426–1436, May 2010, doi: 10.1109/TCOMM.2010.05.080601.

[21] T. Laas, J. A. Nossek, S. Bazzi, and W. Xu, "On reciprocity in physically consistent TDD systems with coupled antennas," *IEEE Trans. Wireless Commun.*, vol. 19, no. 10, pp. 6440–6453, Oct. 2020, doi: 10.1109/TWC.2020.3003414, arXiv:1907.10562.

[22] T. Laas, J. A. Nossek, S. Bazzi, and W. Xu, "On reciprocity of physically consistent TDD systems with coupled antennas," in *Proc. 21st Int. ITG Workshop Smart Antennas (WSA)*, Berlin, Germany, Mar. 2017, pp. 377–382.

[23] T. Laas, J. A. Nossek, and W. Xu, "Gain of uniform rectangular arrays," in *Proc. 24th Int. ITG Workshop Smart Antennas (WSA)*, Hamburg, Germany, Feb. 2020.

[24] D. Nie, B. M. Hochwald, and E. Stauffer, "Systematic design of large-scale multiport decoupling networks," *IEEE Trans. Circuits Syst. I*, vol. 61, no. 7, pp. 2172–2181, Jul. 2014, doi: 10.1109/TCSI.2014.2304666.

[25] H. Rothe and W. Dahlke, "Theory of noisy fourpoles," *Proc. IRE*, vol. 44, no. 6, pp. 811–818, Jun. 1956, doi: 10.1109/JRPROC.1956.274998.

[26] K. F. Warnick and M. A. Jensen, "Optimal noise matching for mutually coupled arrays," *IEEE Trans. Antennas Propag.*, vol. 55, no. 6, pp. 1726–1731, Jun. 2007, doi: 10.1109/TAP.2007.898596.

[27] C. P. Domizioli and B. L. Hughes, "Front-end design for compact MIMO receivers: A communication theory perspective," *IEEE Trans. Commun.*, vol. 60, no. 10, pp. 2938–2949, Oct. 2012, doi: 10.1109/TCOMM.2012.072612.110541.

[28] K. F. Warnick, B. Woestenburg, L. Belostotski, and P. Russer, "Minimizing the noise penalty due to mutual coupling for a receiving array," *IEEE Trans. Antennas Propag.*, vol. 57, no. 6, pp. 1634–1644, Jun. 2009, doi: 10.1109/TAP.2009.2019898.

[29] Y. Hassan and A. Wittneben, "Rate maximization in coupled MIMO systems: A generic algorithm for designing single-port matching networks," in *Proc. IEEE Wireless Commun. Netw. Conf. (WCNC)*, Istanbul, Turkey, Apr. 2014, pp. 1287–1292, doi: 10.1109/WCNC.2014.6952355.

[30] Y. Hassan, "Compact multi-antenna systems: Bridging circuits to communications theory," Dr. sc. dissertation, Swiss Federal Institute of Technology (ETH), Zurich, Switzerland, Mar. 2018.

[31] T. A. de Vasconcelos, A. L. F. de Almeida, and J. A. Nossek, "Matching strategies for multi-antenna arrays," in *Proc. 24th Int. ITG Workshop Smart Antennas (WSA)*, Hamburg, Germany, Feb. 2020.

[32] T. Azevedo de Vasconcelos, "Matching strategies for multi-antenna arrays in single and multiuser scenarios," M. thesis, Federal University of Ceará (UFC), Fortaleza, Brazil, Nov. 2020.

[33] B. Lehmeyer, "Receiver and transmitter topologies," Dr.-Ing. dissertation, Technical University of Munich (TUM), Munich, Germany, Aug. 2018.

[34] J. Kornprobst, T. J. Mittermaier, R. A. M. Mauermayer, G. F. Hamberger, M. G. Ehrnsperger, B. Lehmeyer, M. T. Ivrlač, U. Imberg, T. F. Eibert, and J. A. Nossek, "Compact uniform circular quarter-wavelength monopole antenna arrays with wideband decoupling and matching networks," *IEEE Trans. Antennas Propag.*, vol. 69, no. 2, pp. 769–783, Feb. 2021, doi: 10.1109/TAP.2020.3016422.

[35] M. T. Ivrlač and J. A. Nossek, "A multiport theory of communications," in *Proc. 8th Int. ITG Conf. Source Channel Coding (SCC)*, Siegen, Germany, Jan. 2010.

[36] S. A. Schelkunoff and H. T. Friis, *Antennas, Theory and Practice*. Wiley: New York, Chapman & Hall: London, 1952.

[37] W. K. Kahn and H. Kurss, "Minimum-scattering antennas," *IEEE Trans. Antennas Propag.*, vol. 13, no. 5, pp. 671–675, Sep. 1965, doi: 10.1109/TAP.1965.1138529.

[38] W. Wasylkiwskyj and W. K. Kahn, "Theory of mutual coupling among minimum-scattering antennas," *IEEE Trans. Antennas Propag.*, vol. 18, no. 2, pp. 204–216, Mar. 1970, doi: 10.1109/TAP.1970.1139649.

[39] F. W. J. Olver, D. W. Lozier, R. F. Boisvert, and C. W. Clark, Eds., *NIST Handbook of Mathematical Functions*. Cambridge Univ. Press, 2010.

[40] M. T. Ivrlač, "Physical principles of antenna systems," Associate Professorship for Methods of Signal Processing, Technical University of Munich, Munich, Germany, Lecture Notes, 2016, version 1.0.

[41] Wikipedia. Rotation matrix. Accessed: Nov. 6, 2019. [Online]. Available: https://en.wikipedia.org/w/index.php?title=Rotation_matrix&oldid=924871518

[42] C. J. Taylor and D. J. Kriegman, "Minimization on the Lie group SO(3) and related manifolds," Yale Univ., Tech. Rep. 9405, Apr. 1994.

[43] M. T. Ivrlač, K. Wang, J. A. Nossek, T. Eibert, and U. Imberg, "HWSE-TUM DMN-Cooperation, Stage 1," Report, 2015.

[44] L.-H. Lim, R. Sepulchre, and K. Ye, "Geometric distance between positive definite matrices of different dimensions," *IEEE Trans. Inf. Theory*, vol. 65, no. 9, pp. 5401–5405, Sep. 2019, doi: 10.1109/TIT.2019.2913874.

[45] E. G. Larsson, O. Edfors, F. Tufvesson, and T. L. Marzetta, "Massive MIMO for next generation wireless systems," *IEEE Commun. Mag.*, vol. 52, no. 2, pp. 186–195, Feb. 2014, doi: 10.1109/MCOM.2014.6736761.

[46] M. Petermann, M. Stefer, F. Ludwig, D. Wübben, M. Schneider, S. Paul, and K.-D. Kammeyer, "Multi-user pre-processing in multi-antenna OFDM TDD systems with non-reciprocal transceivers," *IEEE Trans. Commun.*, vol. 61, no. 9, pp. 3781–3793, Sep. 2013, doi: 10.1109/TCOMM.2013.072813.120984.

[47] F. Kaltenberger, H. Jiang, M. Guillaud, and R. Knopp, "Relative channel reciprocity calibration in MIMO/TDD systems," in *Proc. Future Netw. Mobile Summit*, Florence, Italy, Jun. 2010.

[48] S. Bazzi and W. Xu, "A simple over-the-air hardware calibration procedure in TDD systems," in *Proc. IEEE 27th Annu. Int. Symp. Pers., Indoor, Mobile Radio Commun. (PIMRC)*, Valencia, Spain, Sep. 2016, pp. 583–588, doi: 10.1109/PIMRC.2016.7794651.

[49] J. Vieira, F. Rusek, and F. Tufvesson, "Reciprocity calibration methods for massive MIMO based on antenna coupling," in *Proc. IEEE Global Commun. Conf. (GLOBECOM)*, Austin, TX, USA, Dec. 2014, pp. 3708–3712, doi: 10.1109/GLOCOM.2014.7037384.

[50] J. Vieira, F. Rusek, O. Edfors, S. Malkowsky, L. Liu, and F. Tufvesson, "Reciprocity calibration for massive MIMO: Proposal, modeling, and validation," *IEEE Trans. Wireless Commun.*, vol. 16, no. 5, pp. 3042–3056, May 2017, doi: 10.1109/TWC.2017.2674659.

[51] H. Wei, D. Wang, H. Zhu, J. Wang, S. Sun, and X. You, "Mutual coupling calibration for multiuser massive MIMO systems," *IEEE Trans. Wireless Commun.*, vol. 15, no. 1, pp. 606–619, Jan. 2016, doi: 10.1109/TWC.2015.2476467.

[52] T. Laas, J. A. Nossek, S. Bazzi, and W. Xu, "On the impact of the mutual impedance of an antenna array on power and achievable rate," in *Proc. 22nd Int. ITG Workshop Smart Antennas (WSA)*, Bochum, Germany, Mar. 2018, arXiv:2002.06107.

[53] Z. Botev. (2015, Dec.) Kernel Density Estimator. Version 1.5.0.0. [Online]. Available: https://www.mathworks.com/matlabcentral/fileexchange/14034-kernel-density-estimator

[54] Z. I. Botev, J. F. Grotowski, and D. P. Kroese, "Kernel density estimation via diffusion," *Ann. Statist.*, vol. 38, no. 5, pp. 2916–2957, Oct. 2010, doi: 10.1214/10-AOS799.

[55] E. Telatar, "Capacity of multi-antenna Gaussian channels," *Eur. Trans. Telecommun.*, vol. 10, no. 6, pp. 585–595, Nov. 1999, doi: 10.1002/ett.4460100604.

[56] P. Viswanath and D. N. C. Tse, "Sum capacity of the vector Gaussian broadcast channel and uplink–downlink duality," *IEEE Trans. Inf. Theory*, vol. 49, no. 8, pp. 1912–1921, Aug. 2003, doi: 10.1109/TIT.2003.814483.

[57] S. Vishwanath, N. Jindal, and A. Goldsmith, "Duality, achievable rates, and sum-rate capacity of Gaussian MIMO broadcast channels," *IEEE Trans. Inf. Theory*, vol. 49, no. 10, pp. 2658–2668, Oct. 2003, doi: 10.1109/TIT.2003.817421.

[58] R. Hunger and M. Joham, "A general rate duality of the MIMO multiple access channel and the MIMO broadcast channel," in *Proc. IEEE Global Telecommun. Conf. (GLOBECOM)*, New Orleans, LO, USA, Nov./Dec. 2008, doi: 10.1109/GLOCOM.2008.ECP.178.

[59] R. Hunger, *Analysis and Transceiver Design for the MIMO Broadcast Channel*, ser. Foundations in Signal Processing, Communications and Networking. Springer: Berlin, Heidelberg, 2013, no. 8.

[60] D. P. Bertsekas, "On the Goldstein-Levitin-Polyak gradient projection method," *IEEE Trans. Autom. Control*, vol. AC-21, no. 2, pp. 174–184, Apr. 1976, doi: 10.1109/TAC.1976.1101194.

[61] S. Yang and J.-C. Belfiore, "The impact of channel estimation error on the DPC region of the two-user Gaussian broadcast channel," in *Proc. 43rd Annu. Allerton Conf. Commun. Control Comput.*, Monticello, IL, USA, Sep. 2005, pp. 1366–1372.

[62] K. Eriksson, S. Shi, N. Vucic, M. Schubert, and E. G. Larsson, "Globally optimal resource allocation for achieving maximum weighted sum rate," in *Proc. IEEE Global Telecommun. Conf. (GLOBECOM)*, Miami, FL, USA, Dec. 2010, doi: 10.1109/GLOCOM.2010.5683826.

[63] H. Al-Shatri and T. Weber, "Achieving the maximum sum rate using D.C. programming in cellular networks," *IEEE Trans. Signal Process.*, vol. 60, no. 3, pp. 1331–1341, Mar. 2012, doi: 10.1109/TSP.2011.2177824.

[64] C. Guthy, W. Utschick, R. Hunger, and M. Joham, "Efficient weighted sum rate maximization with linear precoding," *IEEE Trans. Signal Process.*, vol. 58, no. 4, pp. 2284–2297, Apr. 2010, doi: 10.1109/TSP.2009.2040016.

[65] S. S. Christensen, R. Agarwal, E. de Carvalho, and J. M. Cioffi, "Weighted sum-rate maximization using weighted MMSE for MIMO-BC beamforming design," *IEEE Trans. Wireless Commun.*, vol. 7, no. 12, pp. 4792–4799, Dec. 2008, doi: 10.1109/T-WC.2008.070851.

[66] B. Lehmeyer, M. T. Ivrlač, and J. A. Nossek, "LNA characterization methodologies," *Int. J. Circuit Theory Appl.*, vol. 45, no. 9, pp. 1185–1202, Sep. 2017, doi: 10.1002/cta.2276.

[67] S. Gault, W. Hachem, and P. Ciblat, "Joint sampling clock offset and channel estimation for OFDM signals: Cramér–Rao bound and algorithms," *IEEE Trans. Signal Process.*, vol. 54, no. 5, pp. 1875–1885, May 2006, doi: 10.1109/TSP.2006.871975.

[68] T. Laas, J. A. Nossek, S. Bazzi, and W. Xu, "On the impact of the mutual reactance on the radiated power and on the achievable rates," *IEEE Trans. Circuits Syst. II*, vol. 65, no. 9, pp. 1179–1183, Sep. 2018, doi: 10.1109/TCSII.2018.2796643.

[69] H. Yordanov, M. T. Ivrlač, P. Russer, and J. A. Nossek, "Arrays of isotropic radiators – A field-theoretic justification," in *Proc. Int. ITG Workshop Smart Antennas (WSA)*, Berlin, Germany, Feb. 2009, pp. 32–35.

[70] E. A. Guillemin, *Synthesis of Passive Networks*. New York: John Wiley & Sons, London: Chapman & Hall, 1957.

[71] P. P. Toulios and E. W. Weber, "Determination of antenna reactance from the far-field expressions," *Proc. IEEE*, vol. 61, no. 2, p. 245, Feb. 1973, doi: 10.1109/PROC.1973.9014.

[72] L. D. Landau, E. M. Lifshits, and L. P. Pitaevskii, "The generalized susceptibility," in *Statistical Physics*, 3rd ed., ser. Course of Theoretical Physics. Oxford, U.K.: Pergamon Press, 1980, vol. 5, sec. 123, pp. 377–384.

[73] O. G. Vendik and D. S. Kozlov, "A novel method for the mutual coupling calculation between antenna array radiators: Analysis of the radiation pattern of a single radiator in the antenna array," *IEEE Antennas Propag. Mag.*, vol. 57, no. 6, pp. 16–21, Dec. 2015, doi: 10.1109/MAP.2015.2481818.

[74] L. Råde and B. Westergren, *Springers Mathematische Formeln, Taschenbuch für Ingenieure, Naturwissenschaftler, Informatiker, Wirtschaftswissenschaftler*, 3rd ed., P. Vachenauer, Ed. Springer Berlin Heidelberg, 2000.

[75] A. I. Uzkov, "An approach to the problem of optimum directive antennae design," *Compt. Rend. Acad. Sci. URSS*, vol. 53, no. 1, pp. 35–38, 1946.

[76] A. D. Yaghjian, T. H. O'Donnell, E. E. Altshuler, and S. R. Best, "Electrically small supergain end-fire arrays," *Radio Sci.*, vol. 43, no. 3, doi: 10.1029/2007RS003747.

[77] S. Schilliger Kildal, N. Pfuhl, R. Flamini, and B. Biscontini, "Molded interconnect device (MID) design for base station antenna elements," in *Proc. 2016 IEEE Int. Symp. Antennas Propag. (APSURSI)*, Fajardo, Puerto Rico, Jun. 2016, pp. 1845–1846, doi: 10.1109/APS.2016.7696629.

[78] T. Laas, J. A. Nossek, and W. Xu, "Limits of transmit and receive array gain in massive MIMO," in *Proc. IEEE Wireless Commun. Netw. Conf. (WCNC)*, Virtual Conference, South Korea, May 2020, doi: 10.1109/WCNC45663.2020.9120590.

[79] S. Verdú, "Spectral efficiency in the wideband regime," *IEEE Trans. Inf. Theory*, vol. 48, no. 6, pp. 1319–1343, Jun. 2002, doi: 10.1109/TIT.2002.1003824.

[80] B. Friedlander, "Localization of signals in the near-field of an antenna array," *IEEE Trans. Signal Process.*, vol. 67, no. 15, pp. 3885–3893, Aug. 2019, doi: 10.1109/TSP.2019.2923164.

[81] "Evolved universal terrestrial radio access (E-UTRA); user equipment (UE) radio transmission and reception," 3GPP, TS 36.101, Dec. 2018, Version 15.5.0.

[82] "NR; user equipment (UE) radio transmission and reception; part 1: Range 1 standalone," 3GPP, TS 38.101-1, Dec. 2018, Version 15.4.0.

[83] "NR; user equipment (UE) radio transmission and reception; part 2: Range 2 standalone," 3GPP, TS 38.101-2, Dec. 2018, Version 15.4.0.

[84] *Toeplitz matrix – MATLAB toeplitz*, The Mathworks, Inc., accessed: 07 Jun 2021. [Online]. Available: https://www.mathworks.com/help/matlab/ref/toeplitz.html